ABSTRACT

Title of dissertation: DIRECTED CELL MIGRATION: FROM SINGLE CELLS TO COLLECTIVELY MOVING CELL GROUPS

Can Guven, Doctor of Philosophy, 2014

Dissertation directed by: Professor Wolfgang Losert
Department of Physics

Unlike molecules, which are driven thermally by Brownian motion, eukaryotic cells move in a particular direction to accomplish designated tasks that are involved in diverse biological processes such as organ development and tumor progression. In this dissertation, I present experiments, analysis, and modeling of directed individual and collective cell migration. At subcellular scale, the migration of cells can be guided via the interaction of the cell cytoskeleton with the surrounding nanotopographic elements. I show that mechanical waves of actin polymerization are involved in this guidance–known as contact guidance–as dynamic sensors of surface nanotopography. The dynamics of guided actin waves were measured to build and test predictive models of contact guidance. The distributions of actin-wave propagation speed and direction were obtained from experimental observations of cell migration on nanotopographic surfaces as a function of the spacing between adjacent features (varying between 0.8 and 5 microns). I show that actin polymerization is preferentially localized to nanoscale features for a range of spacings. Addition-

ally, the velocity of actin polymerization waves moving parallel to the direction of nanoridges depends on the nanoridge spacing. A model of actin polymerization dynamics in which nanoridges modify the distribution of the nucleation promoting factors captures these key observations. For individual cells, the question is how the intracellular processes result in directed migration of cells. I introduce a coarse-grained model for cell migration to connect contact guidance to intrinsic cellular oscillations.

The guidance of collective cell migration can be dictated via intercellular communication, which is facilitated by biochemical signals. I present a coarse-grained stochastic model for the influence of signal relay on the collective behavior of migrating *Dictyostelium discoideum* cells. In the experiment cells display a range of collective migration patterns including uncorrelated motion, formation of partially localized streams, and clumping, depending on the type of cell and the strength of the external concentration gradient of the signaling molecule cyclic adenosine monophosphate (cAMP). The collective migration model shows that the pattern of migration can be quantitatively described by considering the competition of two processes, the secretion of cAMP by the cells and the degradation of cAMP in the gradient chamber. With degradation, the model secreting cells form streams and efficiently traverse the gradient, but without degradation the model secreting cells form clumps without streaming. This observation indicates that streaming requires not only signal relay but also degradation of the signal. In addition, I show how this model can be extended to other eukaryotic systems that exhibit more complex cell-cell communication, in which the impact on collective migration is more subtle.

DIRECTED CELL MIGRATION: FROM SINGLE CELLS TO COLLECTIVELY MOVING CELL GROUPS

by

Can Guven

Dissertation submitted to the Faculty of the Graduate School of the
University of Maryland, College Park in partial fulfillment
of the requirements for the degree of
Doctor of Philosophy
2014

Advisory Committee:
Professor Wolfgang Losert, Chair
Professor Edward Ott, Co-advisor
Professor John Fourkas, Dean's Representative
Professor Arpita Upadhyaya
Professor Michelle Girvan

© Copyright by
Can Guven
2014

To Serap and Derin

Acknowledgments

I would like to thank my advisors Wolfgang Losert and Ed Ott for their immense support and helping me balance experiment and theory throughout the graduate school. I thank John Fourkas for his assistance and providing ideas that fueled my research. I am grateful to Michelle Girvan, who introduced me the field of non-linear dynamics.

I want to thank all members of Losert Lab especially to: Satarupa Das, Meghan Driscoll, Colin McCann, Joshua Parker, Xiaoyu Sun, and Chenlu Wang. The synergy in the lab provided me a seamless working environment, which I enjoyed the most.

I appreciate the help I got from researchers at NIH: Carole Parent, Paul Kriebel and Ritankar Majumdar and thank them for their patience in teaching biology to a physicist. I thank to Oliver Nagel and Carsten Beta from Potsdam University for their collaboration and perseverance for working together over six time zones for over a year.

Also, I would like to thank my friends: Meghan Driscoll, Shane Squires, Anita Roychowdhury, Joshua Parker, Luke Johnson, Jessica Rajkowski, Jeff Grover, Mark Kegel, Mark Herrera, Rachel Lee, Vijay Kaul, Will Stem, and Aram Vartanyan for all the help they provided and for their companionship.

I appreciate all the help and kindness from the members of IREAP. I thank Nancy Boone, Don Martin, Nolan Ballew, and Ed Condon for all their support.

I am deeply grateful to my parents Hatice Guven and Ahmet Guven for sup-

porting me for my entire life. Even though I have spent the last five years of my life mostly away from them, I have always felt their presence with me. I also want to thank my parents in law Necdet Suvari and Yucel Suvari for their support and trust.

Most importantly, I would like to thank my wonderful wife Serap Suvari, for being there for me all the time. I cannot imagine finishing the grad school without her support, mentoring, and love. I thank Derin Ates Guven, who has been accompanying my academic journey in the last two and a half years. You have been my inspiration ever since I held you in my arms for the first time.

Finally, I thank my dissertation committee: Wolfgang Losert, Ed Ott, John Fourkas, Arpita Upadhyaya, and Michelle Girvan.

Table of Contents

List of Tables

List of Figures

List of Abbreviations

ACA	Adenaline Cyclase A
Arp	Actin related protein
ATP	Adenosine triphosphate
Ax	Axenically growing strain
BSA	Bovine serum albumin
cAMP	Cyclic adenosine monophosphate
CRAC	Cytosolic regulator of adenosine cyclase
FCC	Tridecafluoro-1,1,2,2-tetra hydrooctyl dimethyl chlorosilane
IREAP	Institute for Research in Electronics and Applied Physics
LEGI	Local excitation global inhibition
NPF	Nucleation promotion factor
PDE1	Phosphodiesterase 1
PI3K	Phosphatidylinositol-4,5-bisphosphate 3-kinase
PIP	Phosphoinositide lipid
PLL	Poly-L-Lysine
PTEN	Phosphatase and tensin homolog
tal	Talin
WT	Wild-type

Chapter 1: Introduction

1.1 Cell migration

Our overall aim is characterization of directed cell migration. Cell migration is a ubiquitous phenomenon observed in a wide range of processes including embryonic development [1], wound healing [2], and tumor progression [3,4]. The social amoeba, *Dictyostelium discoideum*, serves both as a biological and a mathematical model system for the study the individual components of the multicellular processes listed above. These components include signaling pathways that are involved in the sensing of chemical gradients and the cell cytoskeleton, which plays a crucial role in cell motion [5].

The dynamics of the migration of the slime mold *D. discoideum* has been studied as a model for chemotaxis [6–8], individual amoeboid motion [9–11], and group migration [12, 13]. Studying these phenomena provides insights into human inflammatory response to wounds and infections as well as into cancer cell migration [14].

1.2 A model organism: *D. discoideum*

D. discoideum cells both sense and secrete the same chemoattractant, cyclic adenosine monophosphate (cAMP), providing a bias towards coordinated motion in neighboring cells. For low densities or strong external chemoattractant gradients, uniformly distributed *D. discoideum* cells move independently. However, other conditions allow for chemical signaling between cells, resulting in the formation of chains of migrating cells called "streams" [8, 15, 16].

When food is plentiful, *D. discoideum* cells exist as single cells and chemotax towards the bacterial metabolic product folic acid. When food is removed, *D. discoideum* transitions from single cell to collective behavior - through the spontaneous secretion and detection of cAMP (Fig. 1.1 shows stages of this transition from unicellular phase to the multicellular phase). The cooperative behavior of this spontaneous transition was found to follow Winfree synchronization [17] and the emergence of pulsatile, signaling centers is beautifully described in [18]. These pulses travel through a population of *D. discoideum* in spiral waves [19, 20]. Secretion of the extracellular phosphodiesterase (PDE1) is essential for the spontaneous transition [21]. Each pulse of external cAMP detected by cells results in an increase in gene expression promoting collective behavior [22], and after 4-6 hours of cAMP mediated development, cells begin to aggregate. In order to determine the essentials for chemotaxis and streaming separate from those needed for development, researchers often provide exogenous pulses of cAMP [22, 23].

From the previous studies, it has been found that cAMP secretion is essential

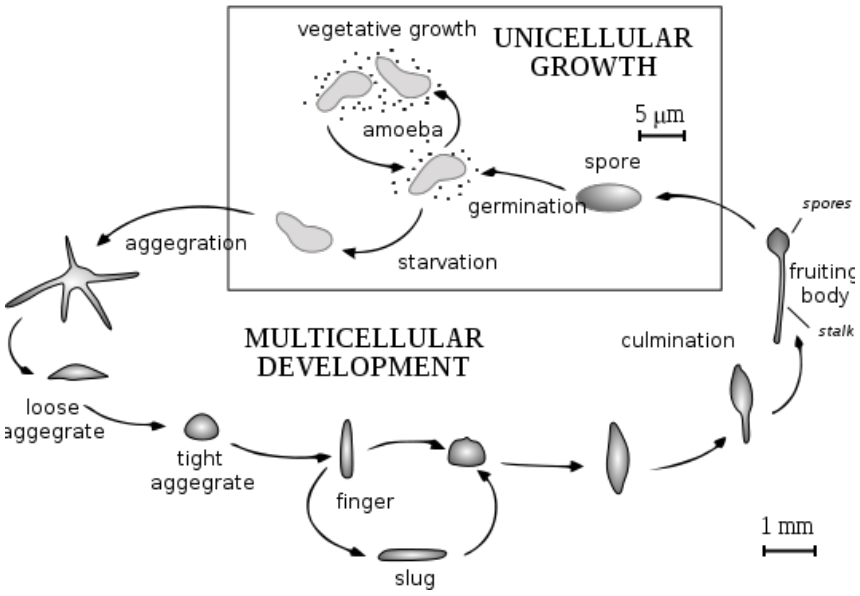

Figure 1.1: *D. discoideum* can exist in either in unicellular or in multicellular phases. (Figure reused under GFDL and CC BY-SA licenses.)

for streaming, but not for chemotaxis. Cells lacking adenyl cyclase A, the enzyme primarily responsible for internal cAMP production during aggregation, will chemotax to cAMP without forming streams [24]. Development and chemotaxis to cAMP in cells lacking the gene for PDE1 can be rescued through periodic addition of partially purified PDE1. Cells lacking PDE1 secretion will chemotax to cAMP and form transient streams to a central source of cAMP, although in linear gradients, the streams appear thicker than wild type [25]. Spontaneous aggregation by developed PDE1 null cells can be recovered with the addition of a uniform bolus of exogenous PDE1, although the addition of exogenous PDE1 is insufficient to recover the spatial extent of the streams.

Aside from the collective aspects of their migration, individual *D. discoideum*

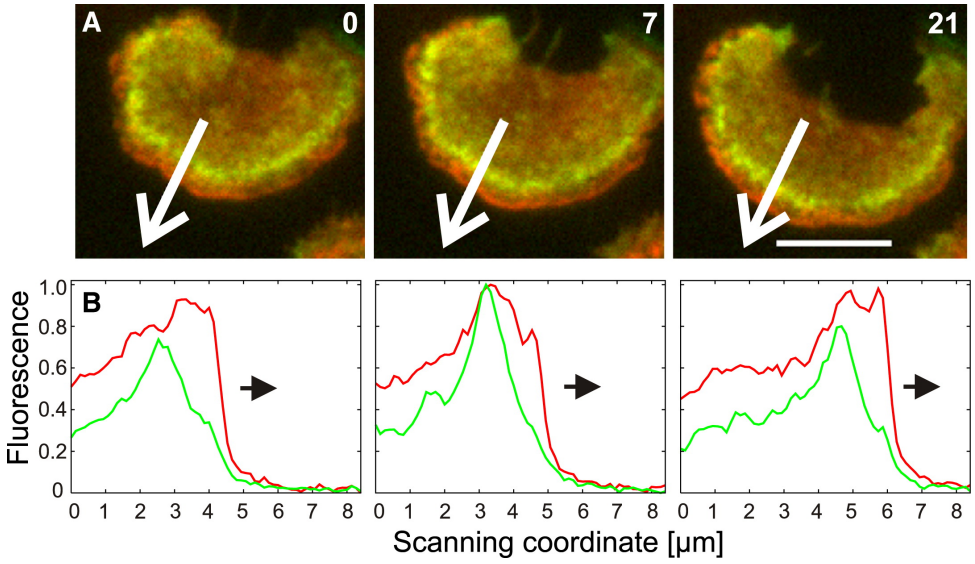

Figure 1.2: (a) Overlayed image of actin binding protein limE-Δcoil tagged with red fluorescent protein and coronin (another actin binding protein) tagged with green fluorescent protein for three time points. (b) Fluorescence intensity of the tagged proteins along the direction of protrusion. Propagation of the polymerization wave front is evident. Time is indicated in seconds. Scale bar is 5 μm. (Figure reproduced from Ref. [26] under Elsevier user license.)

cells move by generating protrusions that are primarily concentrated at their front. These protrusions are large deformations on the plasma membrane and emerge due to the reorganization of the cell's cytoskeleton.

1.3 Migration at subcellular scale

Actin is an essential component of the cellular cytoskeleton. Its dynamic polymerization and depolymerization cycle not only maintains the integrity of the cell's cytoskeleton but also results in generation of the sufficient forces that push against the cell membrane and facilitate movement. Many co-factors assist actin polymeriza-

tion and modify the spatial organization of the polymerized actin filaments [27–29]. *In vivo*, the polymerization of actin exhibits reaction-diffusion waves [30, 31]. These waves of polymerizing actin and their interactions with the cellular environment guide the motion of neutrophils [31, 32] and *D. discoideum* [26, 30]. Fig. 1.2 shows a traveling actin polymerization wave in a *D. discoideum* cell. Here, two actin-binding proteins (limE and coronin) are shown for three snapshots. LimE binds to the polymerizing actin and is tagged with a red fluorescent marker. The expression of this protein is at a maximum close to the plasma membrane (Fig. 1.2a). The profile of the intensity of limE along the direction of cell motion (depicted with white arrows) is shown in Fig. 1.2b, which illustrates the propagation of the wave front. In this dissertation, we investigate how these subcellular waves contribute to directed migration.

1.4 Directed migration

Cells orchestrate complex processes such as identifying external guidance cues and modifying their cytoskeleton to arrive at a target destination, which is dictated presumably by an external chemical or mechanical cue (i.e., a signal) [33, 34]. The preferential migration of cells is known as directed migration and is essential in single cell motion and multicellular processes. A characteristic behavior of the cells that perform directed migration is persistence of their motion [8]. Even in the absence of external cues that provide a preferential direction, cells undergo persistent motion, which becomes random motion over long timescales [9,35]. Of the external cues that

guide cell motion two are prominent: *(i)* guidance by chemoattractant gradients [36, 37] (chemotaxis) and *(ii)* guidance of motion via the interaction between the cell cytoskeleton and the surrounding mechanical restrictions [38] (contact guidance).

1.5 Chemotaxis and collective motion

Eukaryotic cells frequently transduce external chemical gradients into directed cell migration [6], a phenomenon known as chemotaxis. Work in the last few decades has identified components of the intracellular biochemical networks that mediate cellular response to external chemical gradients. It has been found that responsive components such as the phosphoinositide lipids (PIPs), PI3K, and PTEN are highly conserved across cell types. In these efforts, the model organism *D. discoideum* has been a useful source for the discovery of biochemical network components and the development of quantitative models exploring plausible mechanisms for mediating directional sensing.

D. discoideum cells transduce the chemoattractant gradient through G-protein coupled receptors [36,37]. These receptors are uniformly distributed on the cell membrane (Fig. 1.3a). Other intracellular biochemicals are distributed anisotropically in response to the external chemoattractant gradient. For example, in the presence of an external chemoattractant gradient the cytosolic regulator of adenosine cyclase (CRAC) is localized at the cell front (Figs. 1.3a-b). The local excitation global inhibition model (LEGI) recapitulates this localization of biochemicals associated with the gradient sensing [39]. In this model the binding of a ligand to

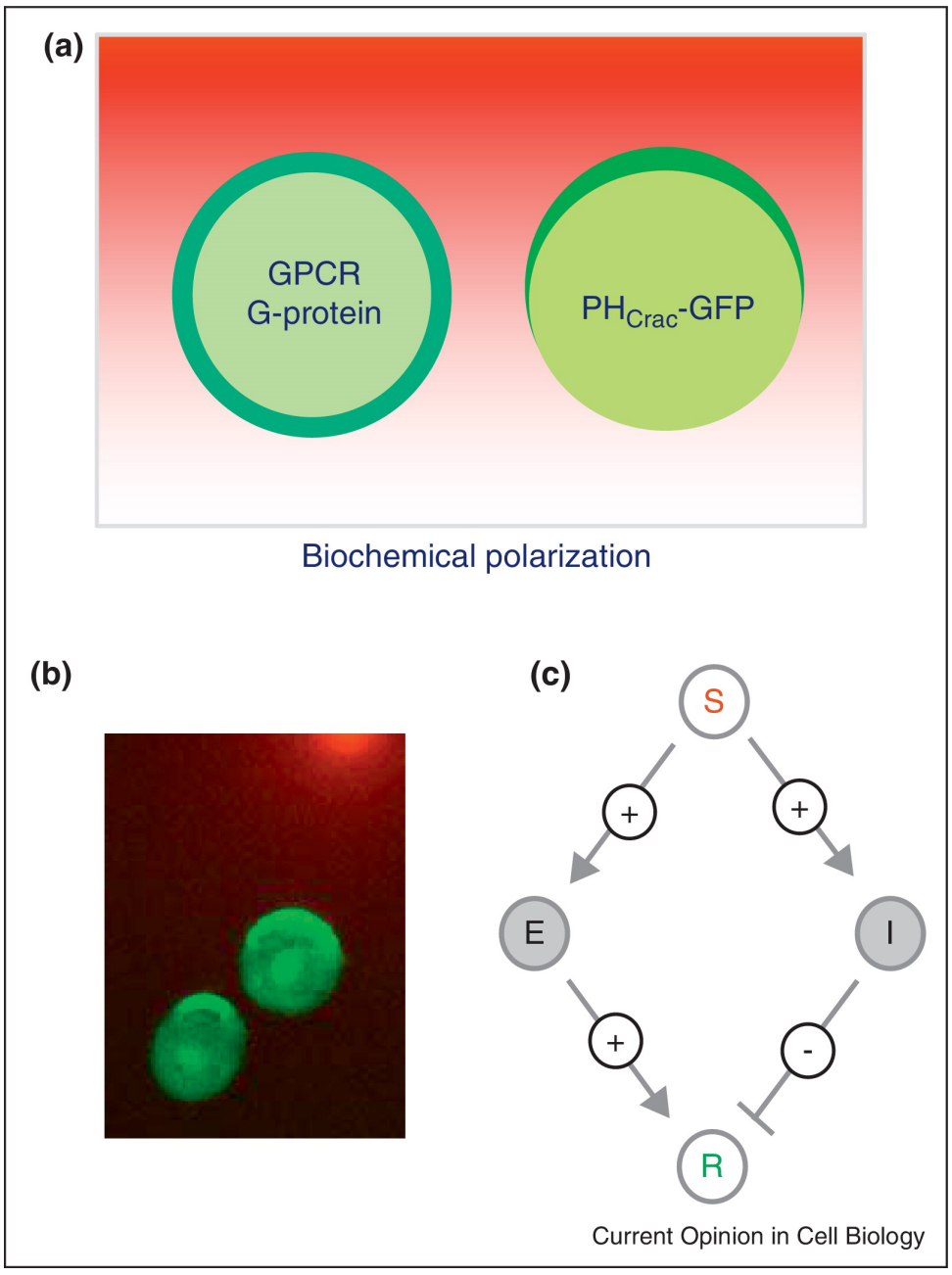

Figure 1.3: (a) In a chemoattractant gradient, G-proteins are uniformly distributed, whereas PH-Crac proteins exhibit spatial asymmetry. (b) Intracellular distribution of GFP-labeled PH-Crac in an externally imposed chemoattractant gradient. (c) Local excitation global inhibition model. (Figure reproduced from Ref. [37] under the CC BY license.)

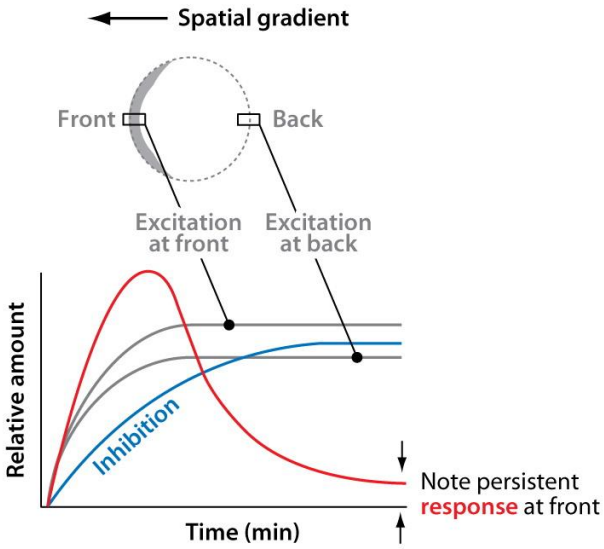

Figure 1.4: In response to an external chemoattractant gradient the membrane-bound excitation and the cytosolic inhibition of the response biochemical results in a spatial anisotropy in its concentration. (Figure reproduced from Ref. [36].)

a receptor triggers simultaneous expression of the excitation and inhibition of the response biochemical (e.g., CRAC). The excitation is local meaning that it only diffuses on the plasma membrane. The inhibitor, on the other hand, diffuses in the cytosol, and is therefore global. This difference in the diffusion of the excitation and inhibition biochemicals establishes a delay between the positive and negative feedforwards (Fig. 1.3c). Additionally, the excitation timescale is faster than the inhibition timescale. The combined difference in the timescales of excitation and inhibition provides an excitable system for the dynamics of the response chemical (Fig. 1.4).

Despite the considerable similarities in gradient detection among *D. discoideum* and mammalian cells including neutrophils and neurons, *D. discoideum* chemotaxis

displays striking collective behavior not often found in other cell types; *D. discoideum* cells responding to the extracellular chemical signal cyclic-AMP (cAMP) tend to migrate in a head-to-tail fashion in what are termed streams [24]. In response to an external cAMP cue, *D. discoideum* cells synthesize and secrete cAMP, thereby relaying the initial signal to nearby cells. Many cell types, including neutrophils, macrophages, and epithelial cells, have potential signal relay loops, but they do not tend to migrate in streams in a standard chemotaxis assay. In this dissertation, I introduce a simple model to analyze how the sensing and signal relay mechanisms affect the collective dynamics of cells.

1.6 Modeling amoeboid migration

Modeling the individual and group migration of *D. discoideum* can provide an understanding of the significance of physical processes that are involved in its motion. Considering that the cells are performing directed migration in response to extremely noisy cues, the dynamics of cell migration is also an interesting problem from a physics perspective. The dynamics of the pre-aggregation stage of *D. discoideum* development was analyzed by Potel and Mackay [13], who observed the motion of cells and calculated various dynamic quantities, such as the mean speed and the mean square displacement of cells and used Furth's persistent motion model [35, 40] to explain their observations. Futrelle et al. [41] investigated chemotactic response to an external signal for early, middle and late developed cells for different durations and frequencies of cAMP pulses. In particular, the chemotactic

index and the speed of the cells during development were analyzed, and significant timescales that define the dynamics were extracted, including the response time to a change in cAMP gradient (which they estimated to be on the order of 20 seconds). Gingle [42] measured the smallest cell density, above which collective motion occurs ($\approx$ 2500 cells/mm^2). Gingle and Robertson [43] showed that this limiting density depends on the development time of the cells. McCann *et al.* quantified the dependence of cell-cell coordination (in particular formation of "cell-streams") with respect to the average distance between cells [8].

The spontaneous emergence of traveling waves in a population of *D. discoideum* cells has attracted the interest of the mathematics and physics communities and has led to the development of several computational models to test hypotheses for mechanisms involving signal transduction, signal relay, and gradient sensing. Pioneering work by Martiel and Goldbeter used a differential equation approach based on the receptor activation and desensitization dynamics [44] to explain the pulses of cyclic AMP. Subsequent models studied mechanisms in *D. discoideum* chemotaxis including wave propagation of cAMP signals in an inhomogeneous excitable medium [19, 45–48], directional sensing via receptor activation followed by further intracellular signaling [39, 49, 50], and physical forces that regulate cell-cell or cell-surface interactions [51–54]. In most of these studies, the physical forces of interest arose from cell-cell contact or tension due to membrane deformation. In this dissertation, I present a coarse-grained model for mechanically-guided cell migration that identifies forces due to the interaction between internal cellular oscillations and periodic nanotopographic features in cell's environment.

1.7 Contact guidance

Mammalian cells conduct many tasks that require motion, such as development, immune response or wound healing while embedded in an extracellular matrix (ECM) [55–57]. The interaction between cells and the ECM is in part biochemical, and involves modulation of specific and non-specific adhesion [58] and modification of the actin scaffolding [59]. However, the ECM also presents a prominent nanotopographic structure through collagen fibrils, which have a characteristic diameter of approximately 300 nm and can elongate for tens of micrometers [60]. Cells can detect and respond to such topography of their environment by altering key biological functions, such as polarization or migration, in a phenomenon that is known as contact guidance [38]. In this dissertation, we show how cells can detect features comparable in size to collagen fibrils even when the cells lack the focal adhesions that typically bind them directly to the collagen fibrils. We further show that the contact guidance efficiency, i.e., the degree to which a cell responds to nanotopography, depends on the spacing between nanotopographic features and appears to involve the intrinsic actin dynamics of amoeboid cells [61].

1.8 Outline

Being able to following directional cues and adjusting their motion accordingly is crucial for cells to accomplish specific tasks. Detecting chemoattractant gradients facilitates directed cell migration and the key components of chemotaxis have been

identified through experiments and modeling. Recently, it has been observed that different mechanical cues can also result in directed migration [62–64]. Although mechanical cues act differently than chemical stimuli (e.g., effect of contact forces are immediate, in contrast with the finite timescales in receptor-ligand binding and subsequent signal transduction) the underlying physical and chemical mechanisms of the cellular behavior in response to these different stimuli exhibit an intricate interplay [65].

In this dissertation, we will first show in Chapter 2 how actin polymerization waves are guided by the externally imposed periodic nanotopography. Detailed analysis and microscopic modeling of actin waves implicates preferential polymerization of actin as a potential mechanism for the mechanical guidance of cells. Based on an actin-polymerization model, we propose microscopic mechanisms for the actin-substrate coupling that recapitulate the observed characteristics of actin waves in the presence of external mechanical stimuli. To investigate the significance of depolymerization of actin in this coupling, we changed the model parameters to mimic the effect of a drug that alters depolymerization. These results are compared to experimental observations of cells under similar conditions. In Appendices A and B the details of the automated analysis of actin polymerization waves are provided. Also, a guide to the analysis software is included with detailed figures that explain the logic of tracking the actin waves and extracting the position of nanoscale features when they are periodic.

In Chapter 3, we present experiments, analysis and modeling of the modification of intrinsic cellular oscillations, when cells are migrating in the presence

of nanotopography. There are two main sections in this chapter. In Section 3.2, we introduce a cellular oscillations model that investigates how intrinsic cellular oscillations are modified in the presence of nanotopography. In contrast with the actin polymerization model introduced in Chapter 2, this model investigates cellular dynamics at a larger scale. We show experimental data that agrees well with the predictions of the cellular oscillation model. The cellular oscillations are also compared to the oscillatory levels of internal actin polymerization observed in other recent experiments introduced in Ref. [67]. We show that the optimal contact guidance can be achieved when the interaction timescale is matched to the characteristic timescale of actin polymerization dynamics. Interestingly, these timescales overlap substantially with the timescales of membrane protrusions (i.e., average duration of each protrusion and period between protrusions on different ends of the leading edge of the cell). In Section3.5, through analysis of cells that are confined in one-dimensional microchannels, we demonstrate that these protrusions can be organized in a way that greatly increases the persistence of the cell motion.

The other aspect of directed cell migration is the chemical guidance via chemoattractant gradients that are either abundant in nature (e.g., as a source of nutrition) or established by secreted chemoattractant molecules (e.g., byproducts of bacterial synthesis). In Chapter 4, we present a collective migration model that is minimal and recapitulates experimentally observed patterns of group migration of *D. discoideum* in the presence of an externally imposed chemoattractant gradient. The model is utilized to understand the competition between neighboring streams of cells and the strength of cell-cell communication through comparison of controlled external

chemoattractant gradients. We use this model to discuss the competition between the different processes that contribute to cell-cell communication and compare the results of the model to existing results from the literature.

As discussed in Refs. [65,68], cells can integrate chemical and mechanical cues by utilizing the associated mechanochemical transduction mechanisms. In Chapter 5, we present an extension of the minimal model that was introduced in Chapter 4 to enable the study of the competition between chemical and mechanical inputs to the direction of guidance of the cell. Finally, we discuss ongoing work about integrating multiple chemical and mechanical inputs, as are present in the natural environment of almost all eukaryotic cells.

Chapter 2: Actin wave guidance via periodic nanotopography

2.1 Overview

The natural environment of eukaryotic cells is composed of complex nanotopographic elements that facilitate directed migration. Guidance of cell motion is required in diverse biological processes such as wound healing, embryonic development, immune response, and tumor growth. An essential component of directed cell migration is actin-based motility. Here, we elucidate how contact guidance is achieved through the dynamic sensing of nanotopography by mechanical waves of actin polymerization. We quantify the dynamics of actin waves traveling on nanoridges and use these data to build and test predictive models of contact guidance, and more generally of the dynamic actin cortex. The actin polymerization model identifies the enhanced nucleation probability of filaments as a potential key factor in contact guidance.

Contact guidance of amoeboid cells involves not chemoattractant gradients, but rather sensing of the local nanotopography. Nevertheless, some or all of the same feedback loops that drive actin polymerization and migration in chemotaxis may be involved in sensing and responding to surface topography [69]. Recent work on the feedback loops that drive actin polymerization has shown that cytoskeletal

regulatory elements (including SCAR/WAVE, Arp 2/3 and additional actin-binding proteins) can generate a range of features including waves and undulations of the cell boundary, or oscillatory, spatially stationary actin foci [70]. Ref. [70] concluded that the oscillatory components are organized by the upstream chemotactic pathways to yield a large membrane deformation, which regulates the motion of the cell.

In this chapter we show that control of actin waves is also involved in the contact guidance of amoeboid cells. Through a combination of quantitative observations and simulations we demonstrate that surface topography guides cell migration by preferential nucleation and guidance of actin polymerization waves. Some of the experimental data presented in this chapter were acquired by Xiaoyu Sun, who also fabricated all of the nanotopographic structures used in the experiments. Additionally, I acknowledge the assistance from Joshua Parker regarding the initial adaptation of the actin polymerization model for simulating actin polymerization on nanotopography.

2.2 Experimental observations

2.2.1 Preferential actin polymerization on nanoridges

To investigate the interaction between actin polymerization and surface topography, we placed starved *D. discoideum* cells on surfaces with spatially periodic nanoridges. The dark regions in the bright-field images shown in Fig. 2.1A are crests that have a constant width of 200-300 nm and a height between 0.4 μm and 1 μm, depending on the sample. The bright regions are the grooves, which separate the

nanoridges by a distance, d. We investigated values of d ranging from 0.8 to 5.0 μm. This range is centered around the characteristic length scale of actin polymerization waves found in prior studies (1 to 2 μm) [71]. After adhesion to the surface, cells were exposed to a spatially uniform cyclic adenosine monophosphate (cAMP) signal to initiate migration. In this work, we used limE-Δcoil-GFP cells, which overexpress limE. The concentration of limE, which is fluorescently labeled, is increased at sites of polymerization of cortical actin [30, 72], enabling the direct visualization and analysis of actin polymerization waves. Although limE labels actin indirectly by binding to polymerizing actin, it has been shown that there is no substantial difference between the dynamics of limE versus those of directly labeled actin [72] within the 100- to 200-nm-thick membrane-bound actin filament network [73].

To focus on the actin activity near the surface in contact with the nanoridges, we imaged cell motion using confocal microscopy with an approximate voxel height of 1 μm (i.e., ranging roughly from the bottoms to the tops of the nanoridges). We observed a visual bias in actin polymerization along the nanoridges, resulting in streaks of limE activity running parallel to the nanoridges (see Fig. 2.1A). As the spacing between nanoridges increases, the number of streaks is reduced. For large spacings (5 μm), actin polymerization mediated by the leading edge is more apparent than actin polymerization along the ridges. We imaged multiple confocal slices separated by 1 μm to analyze the three-dimensional structure of these actin polymerization waves (Fig. 2.1B). We found that polymerizing actin filaments surround the tops of the nanoridges.

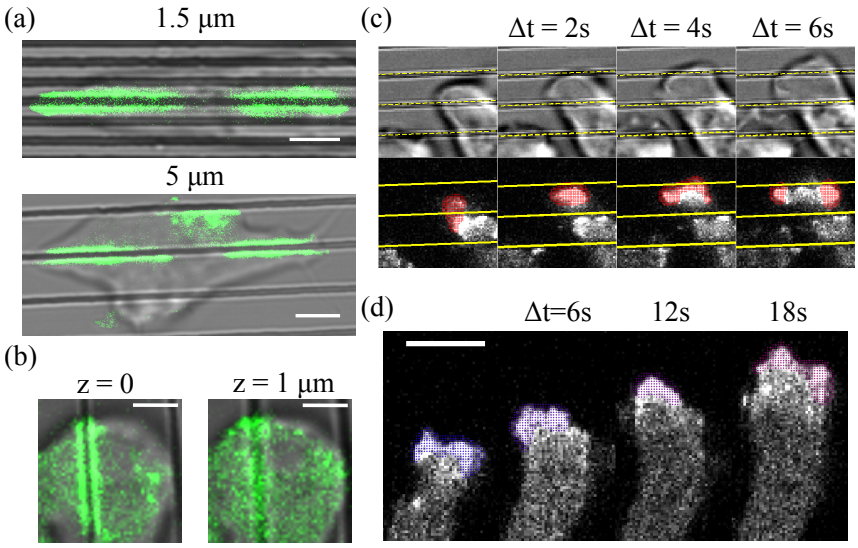

Figure 2.1: (a) Overlayed image of actin binding protein limE-Δcoil tagged with green fluorescent protein and bright field. Actin polymerization on crests of the periodic nanotopography (nanoridges) is enhanced. (b) Confocal slices separated by 1 μm indicate engulfing of nanoridges with polymerizing actin. (c) Snapshots from a cell moving perpendicularly to nanoridges (depicted with yellow dashed lines) for every two seconds (top panel). The corresponding actin dynamics (bottom panel) exhibit an incoming polymerization wave being split by a ridge (depicted with yellow full line). The scale bar represents 3 μm. (d) Propagation of an actin polymerization wave on the substrate for four instances separated in time (6 seconds between instances). The apparent flow of actin polymerization is tracked through clustering of flow vectors obtained via optical flow. All scale bars represent 3 μm.

2.2.2 Quantification of actin polymerization waves

In addition to the preferential actin polymerization parallel to the nanoridges that is steered by the topography, actin waves that nucleate independently of the nanoridges are guided when they encounter nanoridges. A representative example of such an interaction is shown in Fig 2.1C. Here, an actin wave that propagated approximately perpendicularly to a ridge split into two waves with opposite orientations that were aligned parallel to the ridge. More complex wave/ridge interactions, such as waves fracturing into more waves or merging after being split, are shown in Figs. A.1-A.4.

In contrast to a physical flow, actin waves involve reaction-diffusion processes and propagate with a velocity that is determined by growth via treadmilling [26]. Because actin waves and the dynamic phenomena related to them are often highly disordered, it is difficult to analyze the wave dynamics via deterministic properties such as wave speed, frequency, and shape. Furthermore, such properties do not provide an extensive database for comparing theory and experiment. For this reason, we developed an algorithm for the quantitative evaluation of the statistics of guided actin waves directly from experimental videos. The algorithm is applied directly to entire videos, and thus avoids the danger of "cherry-picking" features from the data. This feature is crucial for obtaining an unbiased comparison of simulation and experiment. The algorithm is based on optical flow, and compares individual pixels in successive time-lapse images of actin polymerization to measure the distribution of wave speed and direction. Actin flux vectors are clustered using Tarjan's

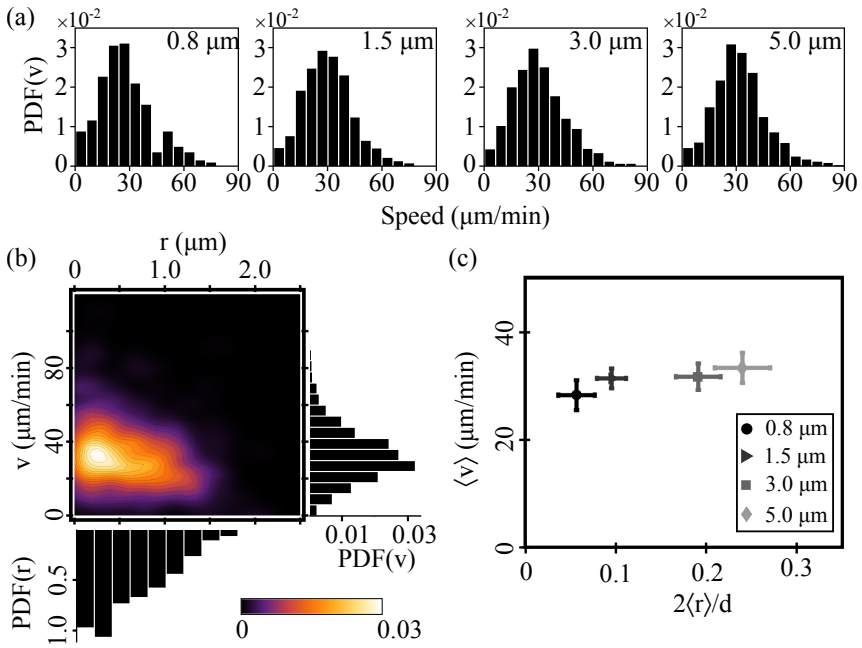

Figure 2.2: (a) Total speed distribution of actin waves on the nanoridges. (b) Joint probability density of the actin waves with respect to their speed, v, and centroid distance from the closest ridge, r, shown for cells moving on 5 μm-spaced nanoridges. The marginal probability densities are shown in the corresponding axes. (c) Mean actin wave speed, $\langle v \rangle$, versus mean relative distance of the actin wave centroid from the closest ridge, $2\langle r \rangle / d$, plotted for four different ridge spacings. Error bars correspond to standard error. All results are obtained from experimentally observed actin waves.

connected-components algorithm [74]. Connections are defined based on the parallel component of a flux vector with respect to its nearest neighbors in space-time (see Appendix A.1). Thus, a cluster of actin flux vectors yields a tracked actin wave. A representative example of a tracked wave is shown in Fig. 2.1D. Tracked clusters in each snapshot are shown with colored dots, which represent the pixels that are in the cluster. Here, snapshots separated by 6 seconds were taken from an actin polymerization wave that propagated parallel to the nanoridges.

Using this technique, we can extract wave velocity distributions from the displacement of the mean cluster position over two consecutive frames and measure both speed and alignment distributions (filtering out contributions from split and fractured waves). We define the alignment of a wave as the average alignment of the flux vectors within a cluster with respect to the nanoridge direction. Histograms of total actin wave speeds for different ridge spacings, shown in Fig. 2.2A, indicate a difference of the speed for waves that are propagating on 0.8-μm- and 5-μm-spaced nanoridges ($p < 0.05$ using Mann-Whitney-U test).

2.2.3 Localization of actin wave activity

To determine the position of actin waves relative to the ridges, we calculated the distance of the initiation point of actin waves from the nearest ridge, r (see Appendix A.3). We measured the joint probability density of actin waves as a function of actin wave speed and distance from the ridge, $P(v, r)$ as shown in Fig. 2.2B (for other spacings see Fig. A.6). For this large nanoridge spacing the wave activity is close to the nanoridges with an average total wave speed of approximately 35 μm/min, which is similar to the speed of membrane curvature waves [11]. The average propagation speed of the actin waves appears to decrease slightly with increasing distance from the ridge. Actin waves on uniform substrates have been reported to propagate with a lower speed of 10 μm/min for cells recovering from depolymerization via latrunculin A [30].

To compare the location and speed of actin polymerization for different ridge

spacings, we plot the average total speed $\langle v \rangle$ versus the average scaled distance of the wave center (normalized by the maximum possible distance from a ridge, $d/2$, see Fig.2.2C). Although there seems to be a small increase in the average wave speed with increasing nanoridge spacing, this trend is not statistically significant. The average actin-wave location shifts away from the ridge with increasing ridge spacing. This behavior is consistent with our observation that, at large ridge spacings, actin waves appear in the flat regions between the ridges.

2.2.4 Effects of cell-nanoridge interaction

Actin wave propagation speed varies as a function of the location and direction of the wave, as already noted qualitatively in Fig. 2.2B. We analyzed the wave propagation speed for the subset of waves that were within 200 nm of a nanoridge. We further distinguished waves based on their alignment, specifically $\theta \in (0, \pi/2)$, which determines how parallel a wave is with respect to the ridge direction (0 and $\pi/2$ correspond to perfect parallel and perpendicular alignment respectively). We divided the near-ridge actin waves into two groups: parallel waves (i.e., $\pi/3 < \theta \leq \pi/2$) and perpendicular waves (i.e., $0 \leq \theta < \pi/6$). We plot the average speed of these groups in Fig. 2.3A. Waves that are aligned parallel to the nanoridges propagate more rapidly as the ridge spacing increases, whereas the speed of perpendicularly aligned waves depends less strongly on the nanoridge spacing (inset of Fig. 2.3A). A potential mechanism for the slower propagation observed along more closely spaced ridges is the increased depletion of actin or nucleation promotion factors (e.g., Arp2/3) by

other polymerization events in the adjacent nanoridges.

We calculated the probability density of the wave orientation, θ, in the vicinity of the nanoridges (i.e., $r \leq 200$ nm) and in the grooves (i.e., 200 nm $< r \leq d/2$, see Fig. 2.3B). Compared to the waves that are in the grooves (inset of Fig. 2.3B), waves closer to the nanoridges tend to align with the ridges. This observation suggests that waves travel preferentially along the nanoridges. The wave alignment distributions for waves on different nanoridge spacings are shown in Fig. A.7.

When actin waves are coupled to the nanoridges, the waves can be considered to be quasi-one-dimensional. However, in the grooves, the waves can propagate in all directions. In Fig. 2.3C we show the joint probability density of wave alignment and wave speed for different nanoridge spacings. On closely spaced nanoridges ($d = 800$ nm), both the average wave speed and its variance are small. The variance of wave propagation speed and the variance in wave alignment increases with increasing ridge spacing as shown in Fig. 2.3C. The increase in the variation of the wave propagation speed and the wave alignment suggest that nanoridges constrain actin waves and influence their characteristics.

2.3 Stochastic modeling of actin polymerization

Actin waves are generally believed to result from reaction-diffusion mechanisms involving autocatalytic positive feedback. Recent reviews of modeling work are given in Refs. [75, 76]. More recent models include those of Refs. [67, 70, 77–80], which in general discuss the feedbacks involved in the generation of the actin polymerization

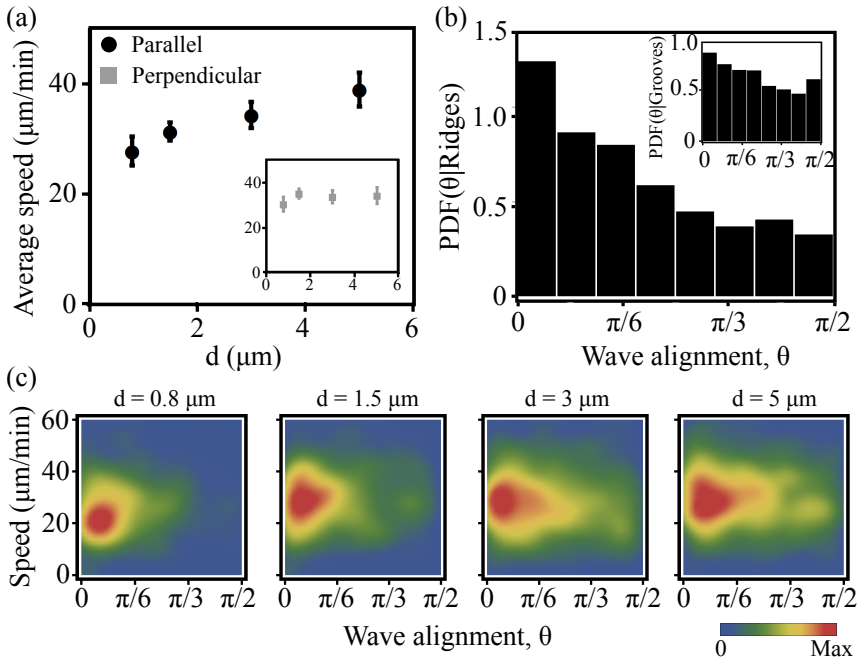

Figure 2.3: (a) Average total wave speed for waves that are in the vicinity of the nanoridges and propagate parallel (black circles) to the nanoridges. The inset shows the same quantity for waves that propagate perpendicular to the ridges (gray squares). (b) Conditional probability distribution of the actin wave alignment with respect to the nanoridges for waves that have a centroid distance to the nearest ridge less than 0.2 μm ($\theta = (0, \pi/2)$ is the angle between the wave vector and the ridge axis). The inset shows the conditional probability density of θ for waves that have a centroid distance greater or equal to 0.2 μm. Both of the distributions are from the 5 μm-spaced nanoridges. (c) Joint probability distribution of total wave speed and wave alignment for all waves on different spacings. All results are obtained from experimentally observed actin waves. Red is associated with the maximum of the probability density. The maximum probabilities for the plots from left to right are 0.042, 0.034, 0.028, and 0.025.

waves. We simulate the polymerization dynamics of actin using realistic biochemical rates, nucleation promoting factors (NPFs) and actin filament severing dynamics as described previously [66]. For details of the actin polymerization model and implementation for a finite domain, see Appendix A.4.

To capture the observed variation in actin filament nucleation due to surface nanotopography shown in Figure 2.1A in our simulations, we modulated the activity of NPFs in a periodic manner, with increased activity of NPFs on stripes mimicking nanoridges. This approach simulates a potential effect of nanoridges on actin polymerization dynamics without the explicit inclusion of the topography in the simulation. Simulations were performed in a rectangular domain of size 8 μm $\times$ 5 μm.

We define k_{nuc} as the NPF-mediated actin nucleation rate, which has units of $\mu\text{M}^{-1}\text{s}^{-1}$. In our actin polymerization model, we fixed k_r and k_g, the actin nucleation activity on the ridges and in the grooves, respectively. The existence of two local rates causes the overall actin nucleation rate to depend on ridge spacing. In the limit of large ridge spacings, the actin nucleation rate approaches k_g. In the small-ridge-spacing limit, the average nucleation rate approaches k_r. We found that we could not capture key experimental observations if we assumed that the average actin nucleation rate is independent of ridge spacing (see Fig. A.9). This observation indicates that enhancement of actin nucleation along nanoridges, rather than a simple redistribution of the location of polymerization activity, is key to the observed contact guidance (the results of an alternative actin polymerization model, where the total NPF activity is kept constant are discussed in Appendix A.4).

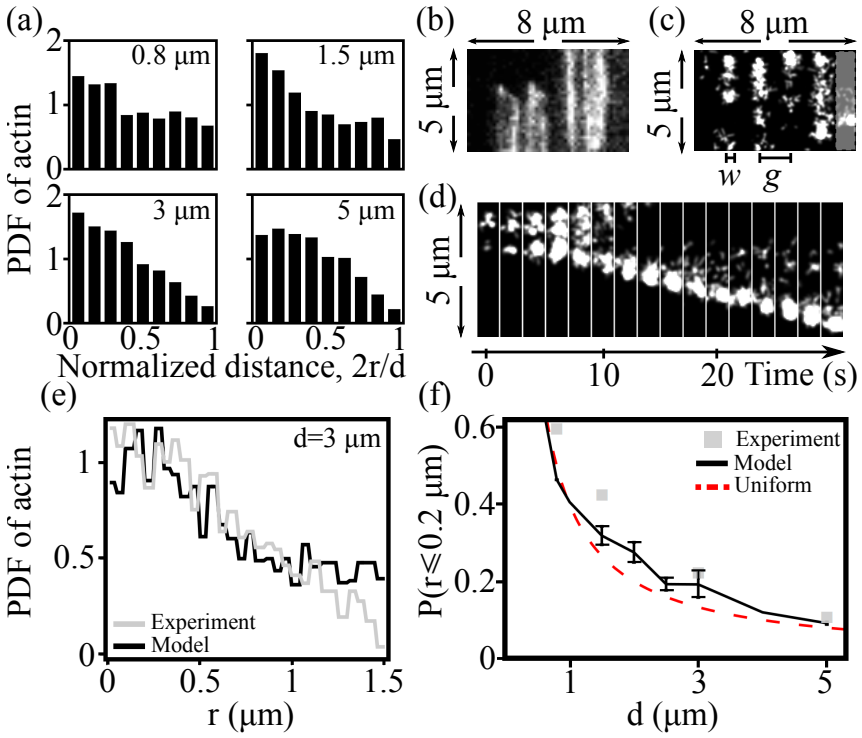

Figure 2.4: (a) Probability density function of polymerizing actin (limE-Δcoil-GFP intensity) with respect to the normalized distance from the ridge for different ridge spacings. (b) limE-Δcoil-GFP intensity from a cell moving on $1.5-\mu$m-spaced nanoridges. (c) A snapshot from actin simulations on modeled nanoridges ($d = 1.5$ μm). Simulations are performed in a two-dimensional domain, where nucleation promotion factor intensity is enhanced on nanoridges with an effective width, w, and unperturbed in the grooves of length, g. (d) Kymograph of the shaded region shown in (c). A wave is initiated on the nanoridges followed by motion parallel to the nanoridges. (e) Probability density of actin polymerization obtained from experiments (gray line) and numerical simulations (black line). (f) Probability of actin in the vicinity of the nanoridges as a function of the ridge spacing for experiment and model results. The dashed red line shows the same quantity for uniformly distributed polymerized actin.

In Fig. 2.4A the calculated rescaled probability density function, $P(2r/d)$, is plotted against the normalized distance from the ridge center, $2r/d$. Compared to $d = 800$ nm and $d = 5$ μm, the number of actin waves with $2r/d < 0.1$ increases in the vicinity of the nanoridges for $1.5-\mu$m and $3-\mu$m spacings. We compare the simulation results with recorded images of limE-Δcoil-GFP (Fig. 2.4B) by transforming the simulated F-actin density with a Gaussian kernel matching the resolution of our confocal microscope images. In Fig. 2.4C, a snapshot from our simulations is shown. The simulated actin polymerization dynamics bear a qualitative resemblance to the experimental results (cf. Fig. 2.4B). In Fig. 2.4D, we illustrate the dynamics of simulated actin waves using a kymograph of actin polymerization on a ridge (marked with dashed red lines in Fig. 2.4C). Initially, a wave nucleates on the ridge. After 8 seconds the wave reaches a length of roughly 2 μm. The wave then splits into two antiparallel waves, one of which leaves the simulation domain and the other of which propagates on the ridge.

2.3.1 Comparison between experiment and theory

By construction, the simulated actin waves are non-stationary due to the selection of the actin-polymerization-model parameters. Also, the tracking algorithm can only extract propagating actin waves. Therefore, we compared the actin-wave profile and total actin activity near the nanoridges for our experimental and numerical results (Figs. 2.4E-F). With increasing ridge spacing the average actin activity in the vicinity of the nanoridges is in fair agreement with our actin polymeriza-

tion model, although the simulation results deviate from the experimental results for narrowly and widely separated nanoridges. Additionally, both the experimental and numerical results converge to a uniform distribution of polymerized actin for both narrow and wide nanoridge spacings.

The behavior of the guided actin waves depends on the concentration of the free actin monomers. Our numerical results show that a reduction of 22% in the monomer concentration does not affect the preferential polymerization along the nanoridges (Figs. 2.5A-B). When the free monomer concentration is reduced, the wave propagation becomes slower (Fig. 2.5C, $p < 0.001$). We validated these simulation predictions experimentally by observing actin polymerization on nanoridges for cells that were treated with latrunculin A, which sequesters actin monomers [81]. At 1.25-μM concentration of latrunculin A, cells became more stationary and the actin activity decreased (Figs. 2.5D-E). Nevertheless, actin still polymerized preferentially parallel to the nanoridges. Results from this perturbation conclude that neither the localization of actin polymerization nor the preferential polymerization of actin is qualitatively affected by the impaired polymerization-depolymerization cycle.

2.4 Discussion

The ability of cells to navigate and migrate in their natural environment is crucial for functions such as wound healing and organ development. Although chemical cell-cell signaling plays an important role in these processes [16], recent research has

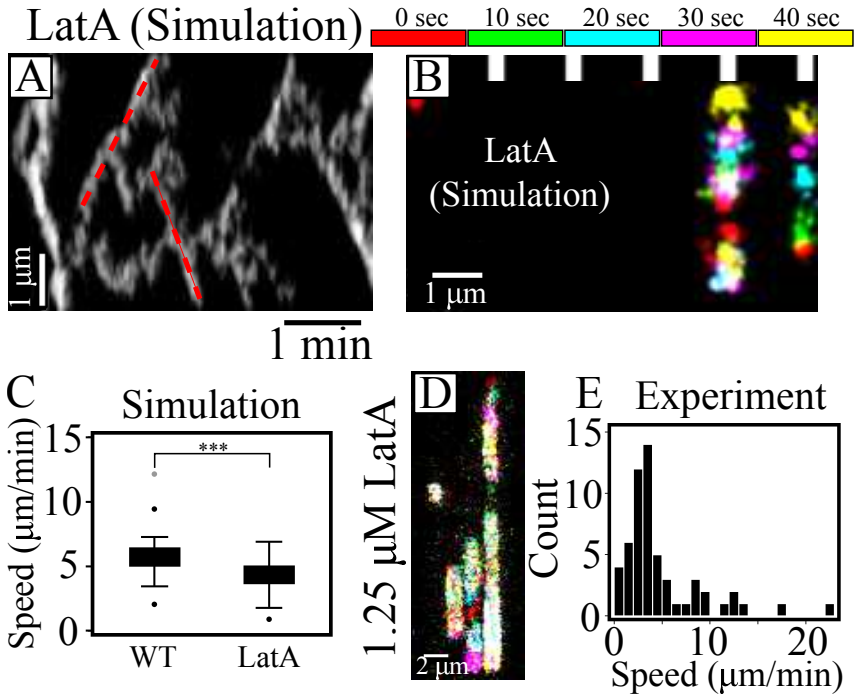

Figure 2.5: (A) Kymograph of polymerizing actin on a nanoridge obtained from a simulation, in which the number of free monomers are reduced. Dashed red lines were used to estimate the average propagation speed of waves. (B) Superposition of snapshots of actin polymerization color-coded with respect to time. White stripes at the top show the location of the nanoridges. (C) Actin wave propagation speed for simulated waves for unperturbed (WT) and perturbed actin polymerization (LatA). The perturbation simulates the effect of latrunculin A treatment (*** corresponds to $p < 0.001$ using Mann-Whitney-U test). (D) Color-coded snapshots for experimentally observed actin waves obtained from 1.25-μM latrunculin A treated cells. White regions indicate that there is stationary polymerization activity. (E) Propagation speed distribution of actin waves for latrunculin-treated cells.

indicated that the topography of the environment can also facilitate directed cell migration [61, 82, 83].

Our detailed analysis of actin dynamics on controlled topographies with bioinspired dimensions indicates that contact guidance involves the nucleation and guidance of actin polymerization waves. The waves are steered by nanotopography with ≈300-nm sized features, which is comparable to the dimension of collagen fibrils. We observe that actin polymerization is enhanced in the vicinity of nanoridges, suggesting that this nanotopography induces nucleation of actin filaments. We showed that in the vicinity of nanoridges actin polymerization waves are preferentially aligned along the nanoridges. The speed of these waves increases with increasing distance between nanoridges. Waves of actin polymerization that do not travel along the nanoridges are dissipated more quickly than waves traveling along ridges as a result of multiple splitting events, in which traveling regions of actin polymerization break up into two regions that travel in opposite directions.

Prior work suggested several mechanisms through which actin dynamics might be affected by surface topography. A number of studies found that actin waves are affected by steric hindrance, or "impact" on a surface. Specifically, the extensions and retraction dynamics of filopodia were found to be guided by obstacles in the surface topography [84], and actin polymerization waves were found to be inhibited upon contact with a local barrier [31]. However, in our experiments the actin polymerization waves travel along the top of a ridge. Although there are no apparent obstacles to wave propagation down the ridge and away from the ridge, such dynamics are not observed.

Our observation that the nucleation of actin filaments is enhanced along the ridge tops suggests models of guidance of actin polymerization that are based on a key characteristic of the ridge top—a highly convex surface curvature. Contact guidance may involve the preferential polymerization of actin on surfaces of high local curvature. This proposal is consistent with other models of preferential branching of actin filaments (biased Arp2/3 binding activity) based on the curvature of the mother filament [85]. The confinement of the plasma membrane on the nanoridges provides such curvature in the actin cortex, which in turn increases the nucleation of actin filaments.

To elucidate the nature of the actin waves, we adapted an actin polymerization model that gives a fully 3D actin filament structure on the basis of realistic biochemical rates and molecular components. *In silico*, we are able to recreate contact guidance via actin waves by simulating stripes with enhanced activity of nucleation promoting factor. From additional simulations, we found that reducing the concentration of actin monomers reduces the overall actin activity.

The success of the modeling in explaining these facets of the experimental data suggests that the ingredients of the actin polymerization model, including stochastic actin nucleation, assembly, and disassembly, are key factors involved in determining the spatial distribution of actin waves. Further work should incorporate a more detailed treatment of upstream signaling pathways.

2.5 Materials and Methods

2.5.1 Cell culture and imaging

The limE-Δ-coil overexpressing *Dictyostelium discoideum* cells (in an AX3 background) were cultured in HL-5 medium at 1–4 $\times$ 10^6 cells/mL with 50 mg/mL hygromyocin B (Sigma-Aldrich H3274). We imaged cells in the pre-aggregate state. Cells were harvested at 4 $\times$ 10^6 cells/mL and shaken at 150 rpm in a beaker with a density of 2 $\times$ 10^7 cells/mL. Cells were then developed for 4 hours in development buffer (5 mM Na_2HPO_4, 5 mM NaH_2PO_4, pH 6.2, 2 mM $MgSO_4$ and 0.2 mM $CaCl_2$). During development, cells were stimulated every 6 minutes with pulses of 50 nM cAMP. The cells were then washed twice in phosphate buffer (5 mM Na_2HPO_4, 5 mM NaH_2PO_4, pH 6.2). To inhibit cell-cell communication, cells were treated with 2 μM caffeine (Sigma-Aldrich C1778) for 30 minutes, while shaken at 150 rpm. For imaging, 300 μL of cell solution with density 5 $\times$ 10^5 cells/mL was added to a multi-well plate. After waiting 5 minutes for the cells to adhere to the surface, 50 μM of cAMP (Sigma A3262) is added to cells to initiate chemokinesis. Latrunculin A (Sigma L5163) perturbations were performed by addition of the drug to a final concentration of 1.25 μM (and a final concentration of 0.05% DMSO by volume) after cells adhered to the substrate. Fluorescence and bright-field images were obtained on a Leica TCS SP5 confocal microscope (Leica TCS SP2 for latrunculin A experiments) with a 100$\times$ objective, and a frame rate of 0.5 frames/second.

2.5.2 Nanoridge fabrication

Structures were fabricated by Xiaoyu Sun according to the protocols explained in Refs. [86,87]. We used a Ti:sapphire laser (Coherent Mira 900 F) to perform multiphoton absorption polymerization. A region of total size 300 μm $\times$ 300 μm was patterned with 200- to 300-nm-wide nanoridges that had a uniform separation of 0.8, 1.5, 3, or 5 μm. The ridges were fabricated using an acrylic resin containing tris–(2-hydroxyethyl) isocyanurate triacrylate (SR368, Sartomer), ethoxylated trimethylolpropane triacrylate (SR499, Sartomer), and Lucirin TPO-L (Ciba). This process yielded a master structure, which was then developed in dimethylformamide and ethanol. In experiments, we made replicas of the master structure using a composite PDMS mold.

2.5.3 Image analysis

Images were processed with custom written MATLAB software. To reduce noise, images and difference images were smoothed with Gaussian filters of different spread. Smoothed difference images were further thresholded. The apparent actin polymerization flux was measured using a modified optical flow algorithm, and parallel flux vectors were clustered. Nanoridges were detected using either a Hough or a Radon transform. Details of the actin wave tracking and nanoridge detection algorithms are explained in Appenix A.1 and Appendix A.3.

2.5.4 Actin simulations

Simulations were performed using a custom C++ program provided by Anders Carlsson modified in collaboration with Joshua Parker from the one published in Ref. [66]. From the simulation results, we measured the actin filament density within 200 nm from the cell membrane with a planar resolution of 10 nm $\times$ 10 nm and a temporal resolution of 0.5 seconds. We then generated pseudoimages from the density data. The images were filtered with a Gaussian kernel and spatially downsampled to mimic the images obtained with the confocal microscope.

Chapter 3: Dynamic sensing of nanotopography

3.1 Overview

In Chapter 2 we showed how actin dynamics can be guided by the nanotopography and suggested preferential actin polymerization as a potential mechanism for the contact guidance of cells. In this chapter, we will discuss the effect of guided actin polymerization on the cell membrane and how the biasing of actin-related cellular oscillations by the surrounding nanotopography can result in guidance of cell migration. Facilitated by the dynamic organization of cortical actin (polymerizing actin on the plasma membrane) cells can recognize features in their environment, which results in an increase in the persistence of their motion. This increased persistence is achieved via a coupling between natural cellular oscillations and the associated periodic encounter of nanotopographic elements in their environment.

Figure 3.1 shows such oscillations, when cells are stimulated with the cell-cell signaling molecule cAMP. Fig. 3.1A presents results of experiments performed by Westendorf et al. [67], which shows that upon stimulation by a cAMP signal (red line) the amount of polymerizing actin in the cytosol decreases (black line), whereas the polymerization of actin on the plasma membrane increases (blue line). The recruitment of actin to the plasma membrane exhibits different dynamic modes.

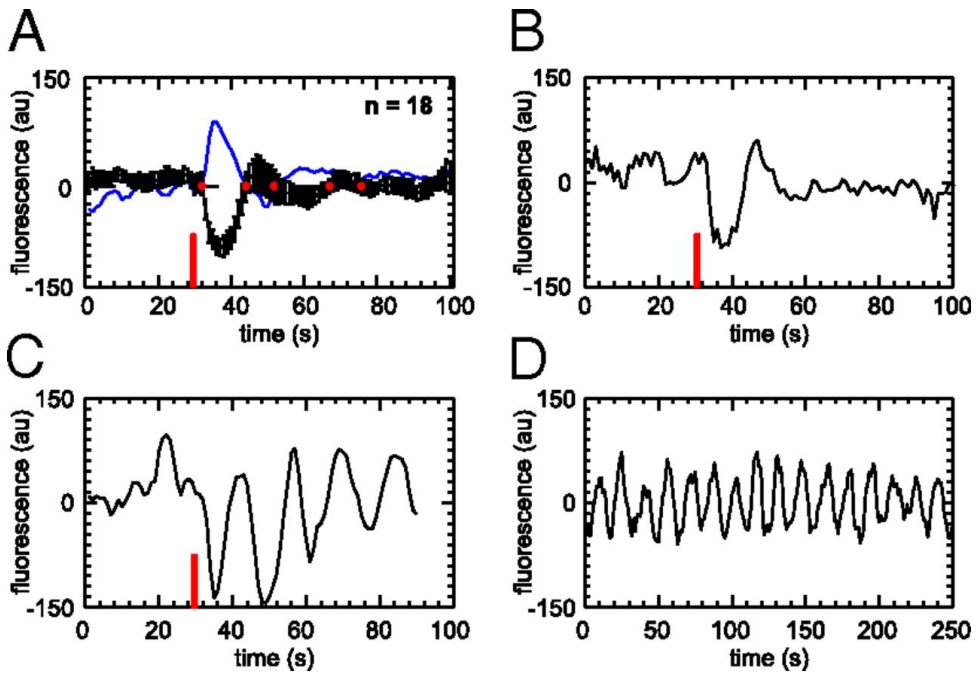

Figure 3.1: (A) Average cortical (blue) and cytosolic (black) LimE-GFP fluorescence signal in response to a short pulse (red) of cAMP. The response time scales were defined by the crossings of the cytosolic signal with the averaged lower confidence interval (dashed line, crossings highlighted by red dots). The averaged confidence interval was calculated from the individual confidence intervals of each data point before the pulse was applied (black error bars). (B-D) Time traces of the cytosolic signal from three different single cells. (B) Example of a strongly damped response to a short pulse of cAMP. (C) Example of a weakly damped response to a short pulse of cAMP. (D) Example of a cell that displays self-sustained oscillations in absence of an external stimulus. (Figure and caption reused from [67]. "Copyright (2013) National Academy of Sciences, USA.")

Figures 3.1B-D show a wide range of dynamic behavior of actin polymerization shuttling from the cytosol to the plasma membrane back and forth. In Fig. 3.1B the excitation of a cell through a cAMP signal at t=30 s is followed by damped oscillations, which quickly dissipate. A similar cAMP pulse excites a cell and actuates self-sustained oscillations of actin polymerization (Fig. 3.1C). Some cells exhibit self-sustained oscillations even in the absence of external stimulation (Fig. 3.1D).

The outline of this chapter is as follows: In the first section, we show how the intrinsic oscillations of polymerizing actin can be mechanically coupled to the nanotopography. In the following two sections we compare the cellular oscillation model results with experimental results and extract biophysical quantities that differentiate mechanically-induced oscillations from chemically-induced oscillations. The experiments that are shown in this section are performed by Meghan Driscoll. In the last section, we show additional experimental data to demonstrate mechanically-guided cell migration. These experiments are performed by Oliver Nagel. In this example– when confined in one-dimensional microchannels–cells undergo highly-persistent migration. Analysis shows that the confinement imposes an ordered formation of left and right pseudopods. Consequently cells "walk" through the microchannel, due to the formation of spatially-stationary patches of actin polymerization in the vicinity of microchannel walls. Interestingly, the lifetime of these stationary patches is similar to the optimal switch time between biasing events, which is different than the resonant timescale of chemically-driven oscillations.

3.2 Nanotopography-driven cellular oscillations

The shape and surface-adhesion dynamics of migrating cells are oscillatory [11]. In this section we show that a coarse-grained cellular oscillation model of a resonant interaction between internal force-generating oscillations and the nanoridge grating can account for our observations of contact guidance.

We model the forces generated by internal oscillations as being biased in the direction parallel to the nanoridges. The interaction of the internal oscillations with the surface nanotopography is described as an overdamped harmonic oscillator, whose dynamics were characterized by a natural frequency ω_0 and a damping coefficient β. We will assume that the interaction between the nanoridges and the membrane oscillations is in the form of a force that drives the membrane oscillations. Any oscillation on the membrane has a parallel and a perpendicular component with respect to the nanoridge orientation. As the cell moves on the nanoridges with an average speed v_0, the perpendicular component of a membrane oscillation encounters a nanoridge with a frequency $\tau^{-1} = v_0|\sin\theta|/L$, where θ is the smallest angle between the centroid position of the membrane undulation from the cell centroid and the nanoridge alignment. L is the distance between two adjacent nanoridges.

The perpendicular and parallel components of the oscillations are coupled through the underlying actin polymerization machinery. We assume that the parallel component of the oscillations was equally affected by the driven perpendicular oscillation. However, due to the symmetry along the direction of the nanoridges, the driving force exerted by the nanoridges can bias the parallel oscillations in either

direction. Therefore, we model this biasing force from the nanoridge grating, $F(t)$, as a stochastic cue that mimics a random square-wave signal. $F(t)$ has amplitude a and correlation time τ, the latter of which is described above.

When the nanoridge spacing approaches zero, the correlation time becomes zero. In this case, because forcing events are not correlated with one another, the net force is not biased. For large nanoridge spacings, correlations become large as well, suggesting the presence of a long-lasting forcing term. However, in this case the correlation time becomes independent of the angle. Therefore, the average force again does not result in bias in any direction. For simplicity, in the rest of the section we will focus only on the perpendicular component of the oscillations (i.e., $\theta = \pi/2$).

The position of these stochastically driven oscillations, x, is described by the damped harmonic oscillator equation:

$$\frac{d^2x}{dt^2} + \beta\frac{dx}{dt} + \omega_0^2 x = F(t) \tag{3.1}$$

where the average force is zero and consecutive driving events are correlated with a timescale τ,

$$\langle F \rangle = 0\,, \quad \langle F(t)F(t') \rangle = a^2 e^{-|t-t'|/\tau}\,. \tag{3.2}$$

3.2.1 Homogenous solution

The homogenous solution of Eq. (3.1) is in the form of $x_h \sim e^{i\Omega t}$. Evaluating this solution in Eq. (3.1) we obtain:

$$-\Omega^2 + i\beta\Omega + \omega_0^2 = 0\,. \tag{3.3}$$

The two roots for Eq. (3.3) are $\Omega_\pm = (i\beta/2) \pm \sqrt{-\beta^2/4 + \omega_0^2}$. In the over-damped case $\beta > 2\omega_0$. We define $\omega := \sqrt{\beta^2/4 - \omega_0^2}$, which is real and positive. Using this definition, $\Omega_\pm = i(\beta/2 \pm \omega)$.

The homogenous solution is the superposition of the two frequencies, Ω_+ and Ω_-:

$$\begin{aligned} x_h(t) &= C_+ e^{i\Omega_+ t} + C_- e^{i\Omega_- t} \\ &= e^{-\beta t/2}\left(C_+ e^{-\omega t} + C_- e^{\omega t}\right) \end{aligned} \tag{3.4}$$

Using the initial conditions $x(0) = A$ and $\dot{x}(0) = B$, we obtain

$$C_\pm = \frac{A}{2}\left(1 \mp \frac{\beta}{2\omega}\right) \mp \frac{B}{2\omega} \tag{3.5}$$

Finally, the homogenous solution shown in Eq. (3.4) becomes:

$$x_h(t) = e^{-\beta t/2}\left(A\cosh(\omega t) + \left(B + \frac{A\beta}{2}\right)\frac{\sinh(\omega t)}{\omega}\right)\,. \tag{3.6}$$

3.2.2 Non-homogenous solution

The non-homogenous solution of Eq. (3.1) can be obtained with the Green's function of the overdamped harmonic oscillator [88],

$$x_p(t) = \int_0^t G(t-s)F(s)ds\,, \tag{3.7}$$

where

$$G(t) = e^{-\beta t/2}\frac{\sinh \omega t}{\omega}\,. \tag{3.8}$$

In the rest of this section we will be focusing on the resonant characteristics of the oscillations, and especially on the power generated by the driven oscillations. For that purpose we only require the solution to Eq. (3.1) in the form of $x(t) = x_h(t) + x_p(t)$.

3.2.3 Power generated by oscillations

The average power generated by the oscillations is defined as $\langle P(t)\rangle := \langle \dot{x}(t)F(t)\rangle$. To obtain this expression, we first calculate the speed of the membrane oscillations, $\dot{x} = \dot{x}_h + \dot{x}_p$. The derivative of the homogenous part is

$$\dot{x}_h(t) = -\frac{\beta}{2}x_h(t) + e^{-\beta t/2}\left(A\omega \sinh \omega t + \left(B + \frac{A\beta}{2}\right)\cosh \omega t\right)\,. \tag{3.9}$$

The second term in the speed is the derivative of the non-homogenous solution, which is calculated using the Leibniz rule

$$\begin{aligned}\dot{x}_p(t) &= \frac{d}{dt}\int_0^t G(t-s)F(s)ds \\ &= \int_0^t \left(\frac{\partial G(t-s)}{\partial t}F(s) + G(t-s)\frac{\partial F(s)}{\partial t}\right)ds + G(0)F(t)\,. \end{aligned} \tag{3.10}$$

Since $\partial F(s)/\partial t = 0$ and $G(0) = 0$, Eq. (3.10) reduces to

$$\begin{aligned}\dot{x}_p(t) &= \int_0^t \frac{\partial G(t-s)}{\partial t}F(s)ds \\ &= \int_0^t e^{-\beta(t-s)/2}\left(-\frac{\beta}{2\omega}\sinh\omega(t-s) + \cosh\omega(t-s)\right)F(s)ds \\ &= \int_0^t \left(-\frac{\beta}{2}G(t-s) + e^{-\beta(t-s)/2}\cosh\omega(t-s)\right)F(s)ds \\ &= -\frac{\beta}{2}x_p(t) + \int_0^t e^{-\beta(t-s)/2}\cosh\omega(t-s)F(s)ds\,. \end{aligned} \tag{3.11}$$

Combining Equations (3.9) and (3.11) we obtain

$$\dot{x}(t) = \kappa(t) - \frac{\beta}{2}x(t) + \int_0^t e^{-\beta(t-s)/2}\cosh\omega(t-s)F(s)ds\,, \tag{3.12}$$

where $\kappa(t) := e^{-\beta t/2}(A\omega\sinh\omega t + (B + A\beta/2)\cosh\omega t)$. This is the only term that depends on the initial conditions A and B. Since we will be interested in the steady state oscillations the initial conditions are not important and can be chosen zero without loss of generality [89]. Therefore κ becomes zero as well. Next, we calculate the power generated by steady state oscillations:

$$\langle P\rangle = -\frac{\beta}{2}\langle x(t)F(t)\rangle + \int_0^t e^{-\beta(t-s)/2}\cosh\omega(t-s)\langle F(s)F(t)\rangle ds\,. \tag{3.13}$$

The first term in the equation above consists of two terms: $-(\beta/2)\langle x_h(t)F(t)\rangle = -(\beta/2)x_h(t)\langle F(t)\rangle = 0$ and

$$
\begin{aligned}
-\frac{\beta}{2}\langle x_p(t)F(t)\rangle &= \int_0^t G(t-s)\langle F(s)F(t)\rangle ds \\
&= -\frac{a^2\beta}{2}\int_0^t G(t-s)e^{-|t-s|/\tau}ds\,. \qquad (3.14)
\end{aligned}
$$

Using Eq. (3.8) and performing the integral for $t \to \infty$ (for steady state) Eq. (3.14) yields

$$
-\frac{a^2\beta/2}{\left(\frac{\beta}{2}+\frac{1}{\tau}\right)^2-\omega^2}\,. \qquad (3.15)
$$

Similarly the second term in Eq. (3.13) at steady state yields

$$
\frac{a^2\left(\frac{\beta}{2}+\frac{1}{\tau}\right)}{\left(\frac{\beta}{2}+\frac{1}{\tau}\right)^2-\omega^2}\,. \qquad (3.16)
$$

In calculating both terms we used the condition for the overdamped case, $\beta/2 > \omega$, which provided the convergence of the results. Next, we add Equations (3.15) and (3.16) and obtain a simplified expression for Eq. (3.13)

$$
\begin{aligned}
\langle P\rangle &= \frac{a^2/\tau}{\left(\frac{\beta}{2}+\frac{1}{\tau}\right)^2-\omega^2} \\
&= \frac{a^2\tau}{1+\beta\tau+(\omega_0\tau)^2}\,, \qquad (3.17)
\end{aligned}
$$

where we used the relation $\omega^2 = \beta^2/4 - \omega_0^2$.

3.2.4 Normalization

We normalize the average power with the amplitude of the stochastic force and the average speed of the cell $\langle P'\rangle = \langle P\rangle/(av_0)$. We substitute the correlation

time τ with the spacing between nanoridges using $\tau = L/v_0$:

$$\begin{aligned} \langle P' \rangle &= \frac{aL}{v_0^2 \left(1 + \frac{\beta}{v_0} L + \left(\frac{\omega_0}{v_0} L\right)^2\right)} \\ &= \frac{a'L}{1 + \beta' L + (\omega_0' L)^2}\,, \end{aligned} \tag{3.18}$$

where we define $\beta' := \beta/v_0$, $\omega_0' := \omega/v_0$, and $a' := a/v_0^2$. With this choice of normalization factors, all of the cellular-oscillation-model parameters has units of inverse distance.

3.2.5 Resonance

The normalized power exhibits a resonance for $L = 1/\omega_0'$. This resonance implies that the power generated by the internal oscillations is maximized, when the correlation time between subsequent biasing events matches to the characteristic time of the internal oscillations. In Fig. 3.2 the normalized average power given in Eq. (3.18) is plotted against the nanoridge spacing.

To obtain this plot we make the following assumptions to estimate the cellular-oscillation-model parameters. $2/\beta$ is defined as the decay time of oscillations, which we relate to the average duration of the protrusions. This timescale is measured around 10 seconds [90, 91]. ω_0 is the resonant frequency of the chemically-driven oscillations of polymerizing actin, which is approximately 20 seconds [67]. The inverse of the normalized amplitude of the force $(1/a')$ has also units of length. Ref. [92] reported that the contact guidance of melanocytes depends on the height

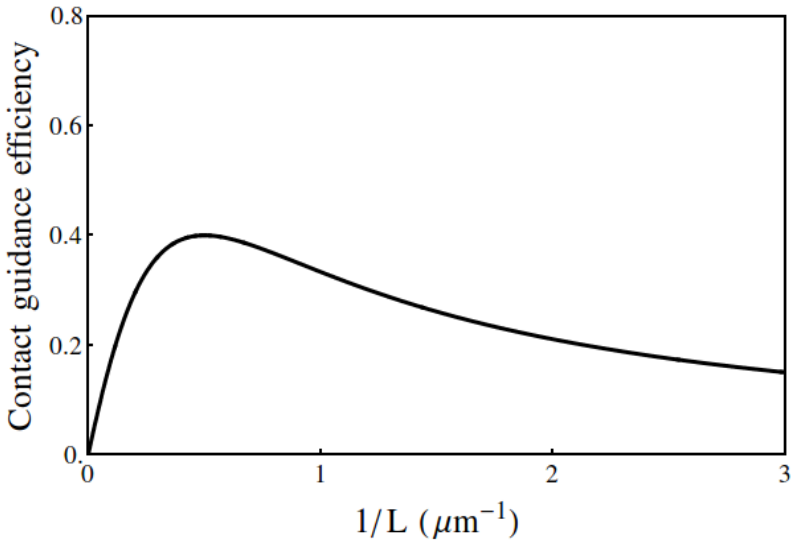

Figure 3.2: Predicted normalized average power generated by oscillations (Eq. (3.18)). In this plot we used biophysical quantities for the cellular-oscillation-model parameters (see text). The cellular oscillation model predicts a resonance for the contact guidance between 1-2 μm.

of the micron scale ridges. Therefore, we associated $1/a'$ with the height of the nanoridges (≈ 0.5 μm).

3.3 Measuring contact guidance

To observe whether the resonance of the internal oscillations leads to a guidance in the overall cell motion, we assayed cell migration on nanoridges with a variety of spacings. We used gratings with spacings of 0.4, 0.6, 0.8, 1.0, 1.2, 1.5, 2, 3, 5, and 10 μm. Fig. 3.3A shows the distributions of the alignment of the cell long axis with respect to the ridge direction (weighted by eccentricity) for several of the nanoridges. We found that the nanoridges with the larger spacings induce little contact guidance. On average, cells are 10 to 20 μm long and 5 μm wide.

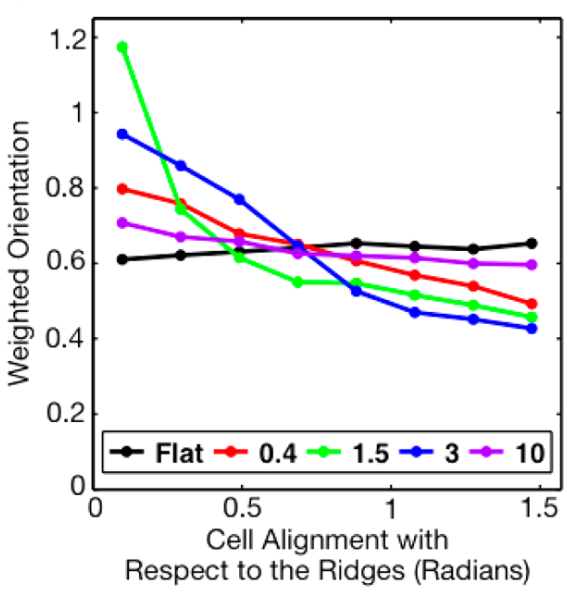

Figure 3.3: Alignment, weighted by eccentricity, of cells migrating on nanoridge gratings with ridge spacings of 0.4, 1.5, 3, and 10 μm. (Figure reproduced with permission from [61]. Copyright (2014) American Chemical Society.)

A reduction in contact guidance is expected when the nanoridge spacing is greater than cell width. We also found that gratings with nanoridge spacings smaller than 1 μm exhibit reduced contact guidance. The distributions of cell alignments (weighted by eccentricity) fit well to a Gaussian with periodic boundary conditions. Unlike a regular Gaussian distribution, a circular Gaussian has only one fitting parameter, which is proportional to the inverse variance of the distribution. This single fitting parameter, which we term the contact guidance efficiency, can be used to characterize the cell alignment distributions. Analyzing *D. discoideum* migration, we find that the contact guidance efficiency is greatest for nanoridge spacings between 1.0 and 2.0 μm (see Fig. 3.3C).

To fit the weighted orientations of cell orientation with respect to eccentricity (see Fig. 3.3), we used a stochastic cellular oscillation model for the dynamics of cell orientation that is developed by Kemkemer *et al.* [92]. In this coarse-grained orientatio-sensing model it is assumed that cells identify the orientation of the nanoridges with respect to their orientation and turn towards the ridge alignment. This situation is described by the following differential equation

$$\frac{\partial \phi}{\partial t} + p \sin 2\phi = \xi(t)\,, \tag{3.19}$$

where ϕ is the average cell orientation with respect to the ridge alignment. As shown in Eq. (3.19), this coarse-grained orientation-sensing model has a feedback mechanism that turns the cell towards the ridge alignment. The amount of turning depends on the orientation of the cell non-linearly. Also, due to the symmetry of the ridges, cells can turn towards the ridges independent of their direction of the motion (the turning amount is independent under the transformation $\phi \to \phi + \pi$). The cell turning rate is described by p, which is a function of the topographical signal. The stochastic term, $\xi(t)$, models fluctuations in the cells determination of the surface topography. The introduced noise, $\xi(t)$, is white, and so has zero average (i.e., $\langle \xi(t) \rangle = 0$). Its amplitude q, is given by the relation

$$\langle \xi(t)\xi(t') = q\delta(t - t') \rangle\,, \tag{3.20}$$

where the brackets are an average over all cells, and δ is the Dirac-delta function. In our experiments we measure the probability density of the orientation angle, $P(\phi)$,

which is less noisy than the dynamics of the orientation angle. Therefore, instead of using Eq. (3.19) directly, we consider the corresponding Fokker-Planck equation, which determines the time evolution of the probability density of the orientation angle, $P(\phi, t)$ [93]

$$\frac{\partial P}{\partial t}(\phi, t) = \frac{\partial}{\partial \phi}\left(p \sin 2\phi + \frac{q}{2}\frac{\partial}{\partial \phi}\right) P(\phi, t)\,. \tag{3.21}$$

The steady-state solution of this equation yields the observed probability density of the orientation angle

$$P(\phi) = \frac{e^{(p/q)\cos 2\phi}}{2\pi I_0(p/q)}\,, \tag{3.22}$$

where I_0 is the modified Bessel function of the first kind of order zero. We used the probability densities of the weighted orientations to find the fit parameter $\sigma = p/q$. Fig. 3.4 shows representative fits to orientation distribution of cells weighted by their eccentricity moving on nanoridges with different spacing. This fit parameter resembles a signal-to-noise term and can be used as a measure to determine the ability of the cells to detect the nanotopography. We define this quantity as the contact guidance efficiency.

3.4 Comparing experiments and cellular oscillation model

We suggest that the normalized power is a useful quantity for comparing the efficiency of contact guidance to the efficiency of internal oscillations. Fitting the normalized averaged power, Eq. (3.18), to the contact guidance efficiencies mea-

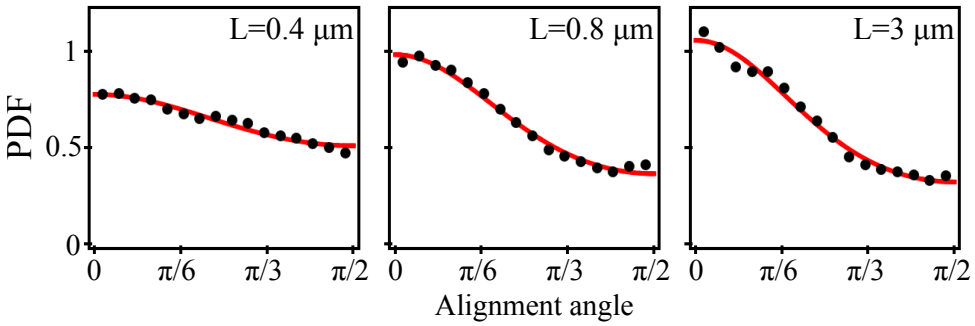

Figure 3.4: To measure the surface contact guidance efficiency, weighted alignments from individual experiments (black dots) were fit to a stochastic orientation-sensing model of cell guidance (red lines) for cells moving on nanoridges with different spacing. The orientation-sensing model predicts the cell alignment in the form of Eq. (3.22). (Data courtesy Meghan Driscoll).

sured for a broad range of nanoridge spacings, we find length and time scales that characterize the cell's interaction with the nanoridges.

The contact guidance efficiencies and the fit are shown in Fig. 3.4. The three scales correspond roughly to the spatial resonance length scale (the peak position in Fig. 3.5), a damping length scale (the width of the peak), and the signal strength (the height of the peak). We find a resonance in the interaction of the cellular oscillations with the nanoridge grating at $1/\omega_0 = 1.7$ μm, which is comparable to the size of protrusions and actin waves in *D. discoideum* cells [30]. To interpret the remaining parameters extracted via the cellular oscillation model, we set $v_0 = 10$ μm/min, which is the average speed of the cells [8], the speed of protrusions relative to the cell, and the speed of actin waves [30].

From the fit, we find a damping coefficient of $1/\beta' \approx 1.17\mu$m, which leads to an oscillation decay time of $2v_0/\beta'$=14 s. This timescale is roughly the duration of

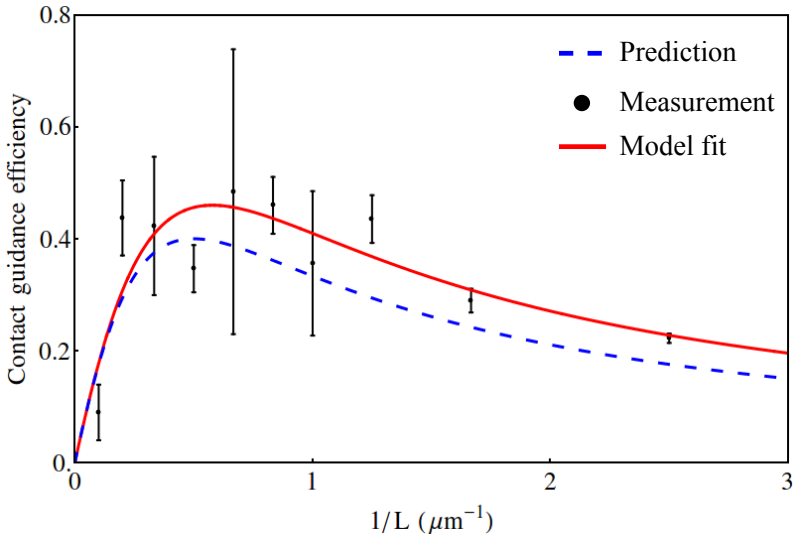

Figure 3.5: Surface contact guidance efficiencies of various nanoridge gratings shown in black dots as a function of the inverse ridge spacing, with the fit to the stochastic harmonic oscillator model shown in red. The predicted curve was shown with blue dashed lines. (Data courtesy Meghan Driscoll).

protrusions [90,91]. The amplitude of the signal received by the cell is $1/a' \cong 0.5$ μm. The fit yields a natural frequency coefficient of $1/\omega_0' \approx 0.57$ μm. Using v_0, we can also interpret this spatial resonance scale as a time scale. The mean sensing time is the frequency at which the intrinsic cellular oscillations sense the up-down symmetry of the ridges via the stochastic signal. The probability density of the biasing force to switch from one direction to the opposite direction is given by $\lambda e^{-\lambda t}$, where λ^{-1} is defined as the switching time [89]. This time is calculated as $\lambda^{-1} = 2/(\omega_0' v_0) \approx$7 s. This is the optimal duration between biasing events for a protrusion to be guided best by the nanoridges during its lifetime.

In the next chapter, we will show that the duration of stationary actin patches, which form in response to an interaction with a microchannel wall peaks around 10 seconds. The resonance timescale of localization of actin to the plasma membrane is in response to chemical inputs and is around 20 seconds [67]. There are no chemical signals involved in the contact guidance of the cells used in our experiments. Therefore, we can conclude that the mechanically-induced resonance timescale is roughly a factor of two faster than the chemically-induced resonance of actin localization.

"This section is adapted with permission from [61]. Copyright (2014) American Chemical Society."

3.5 Geometry-driven persistent motion

In this section, we show that persistent motion can also emerge from the confinement of cells in lower-dimensional geometries. The natural environment of

eukaryotic cells consists of narrow interstitial spacings. Cells developed different strategies to move in different environments. For example when confined in stiff environments such as tissue, neutrophils (a type of immune cell) generate focal adhesion sites. In these regions actin is rich and mediated via receptors that can identify extracellular molecules on the sites of contact. On the other hand, their migration in blood stream resembles amoeboid-type motion, which they utilize to swim [10]. Interestingly, *D. discoideum* cells can also undergo persistent migration in confined geometries even though they lack focal adhesions. In one-dimensional microchannels, these cells maintain contact with the two sides of the microchannel walls and exhibit increased persistence (five times more than their measured persistent motion in planar surfaces) by organizing their protrusion in a controlled manner. Additionally, detailed analysis of the actin cytoskeleton revealed that during their enhanced persistent migration, stationary patches of actin emerge at the sites of contact with microchannel walls. The average lifetime of these patches are 15 seconds.

3.5.1 Experimental observations

Figure 3.6 shows the persistent motion of a *D. discoideum* cell in when it is moving in a microchannel. The persistence time for this example is greater than 15 minutes, which is more than two times the characteristic persistence time of *D. discoideum* motion on planar surfaces. A large portion of the cell body maintains a quasi-rectangular shape throughout the migration. However, the leading edge of

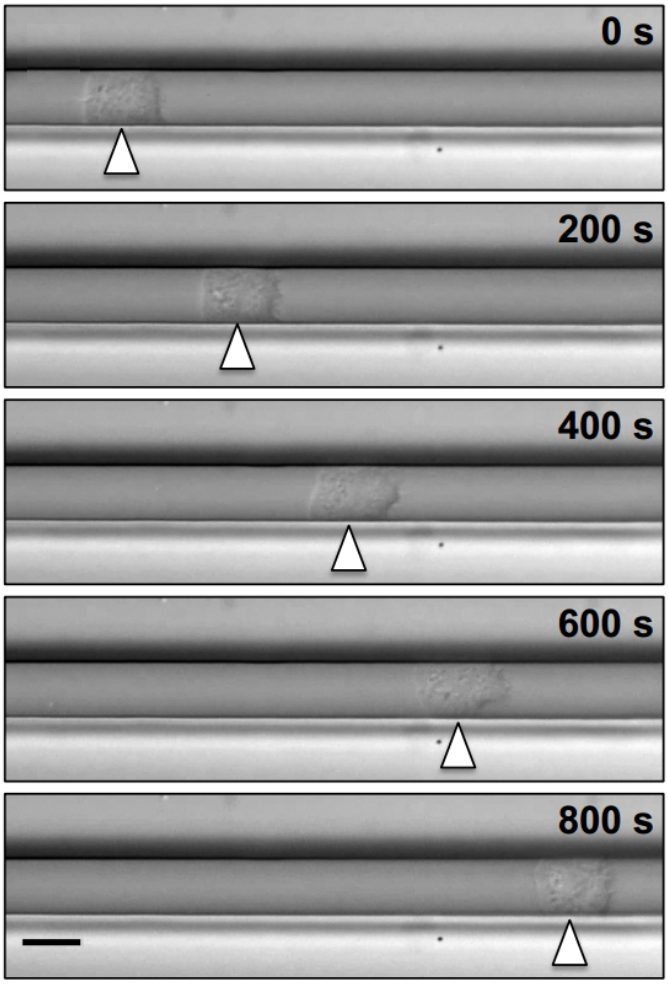

Figure 3.6: When confined in microchannels, cells move more persistently in a direction. Scale bar 10 μm. (Experimental data and figure courtesy Oliver Nagel and Carsten Beta)

cells exhibits large membrane fluctuations. Specifically, the both edges that are in contact with the side walls of the microchannel elongate in the direction parallel to the cell motion.

We quantify these dynamic regions at the leading edge by a tailored edge-detection algorithm (details of this algorithm is explained in Section 3.6.1). Using this algorithm we track the position of the four corners of a cell that is in contact with the microchannel walls. For one cell, the position of the front and back corners in corresponding comoving frames were shown in Fig. 3.7 as a function of time. We observe that the front corners oscillate with respect to the average position of the front of the cell. Additionally, these oscillations are out of phase (i.e., with respect to the direction of motion of the cell when one corner is maximally stretched from the average location of the cell front in the positive direction, the opposite front corner stretches maximally in the negative direction vice versa). The autocovariance function of the oscillation of each front corner shows exponential decay, whereas the cross-covariance between front corners exhibits definite periodic behavior. These observations indicate that the pseudopod activity depends on the activity of the opposite pseudopod. Confinement of cells in these 1D microchannels may result similar sloshing of polymerizing actin between the side walls. In the previous chapter, we showed similar dynamics of actin polymerization in response to interaction with nanoridges (see Fig. 2.1d).

In contrast with the dynamic behavior of the front corners, the back corner of the cell move uniformly with respect to the average location of the back of the cell (Fig. 3.7). This monotonic motion at the back is sustained throughout the

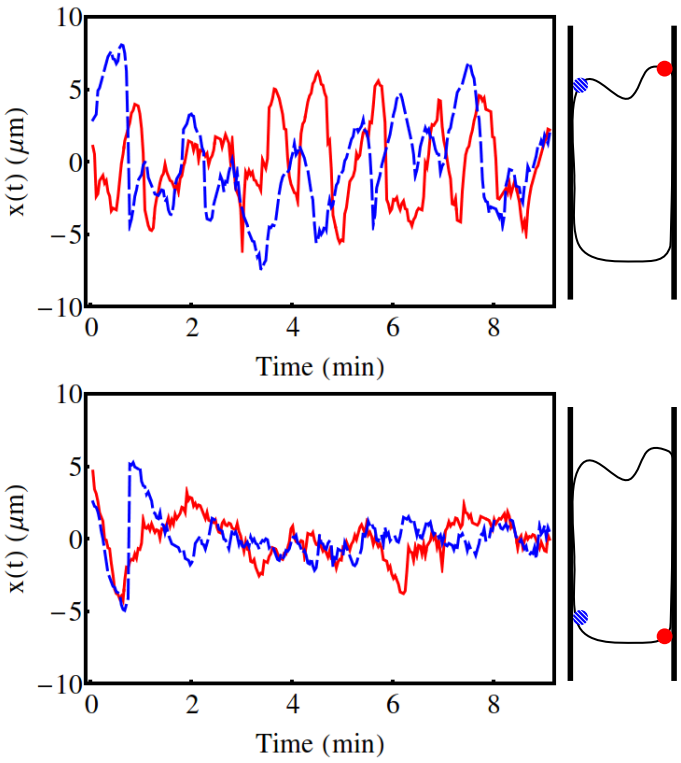

Figure 3.7: Positions of the front and back corners of the cell in contact with the side walls of the microchannel (see cartoon for the spatial definition of a corner). The positions are measured in the cell reference frame. Front corners exhibit oscillations, whereas back corners exhibit steady retraction. (Experimental data courtesy Oliver Nagel)

migration of the cell in the microchannel. The behavior of front and back corners suggest that cells maintain their mechanical polarity (i.e., the asymmetry in the cytoskeletal dynamics that yields highly dynamic protrusions at the cell's front and uniform retraction at the cell's back) due to the persistent interaction with the side walls of the microchannel. Since there are no chemical gradients inside the microchannel, we defined the asymmetric distribution of actin polymerization as mechanically-induced polarity (cf. chemically-induced polarity during chemotaxis). Next, we analyze how the dynamics of actin polymerization associated with the mechanically-induced polarity are different from those of the chemically-induced polarity.

In Section 3.4 we saw evidence of discrepancy between the characteristic timescales of mechanically- and chemically-driven actin polymerization. We now quantify the actin polymerization dynamics of cells undergoing motion with mechanically-induced polarity. We analyze polymerizing actin in a small cellular region close to the microchannel wall (Fig. 3.8A). We average the intensity in the direction perpendicular to the direction of cell motion. This averaging results in a characteristic profile of actin polymerization shown in Fig. 3.8B. Fig. 3.8C shows this averaged profile as a function of time for one cell. We observe that the cell is undergoing uniform motion. However, we also observe multiple high-intensity regions of polymerizing actin that remain stationary with respect to the lab reference frame. In fact, almost all of the high-intensity regions exhibit stationary behavior to a certain extent.

We have developed an algorithm to measure the duration of these spatially-

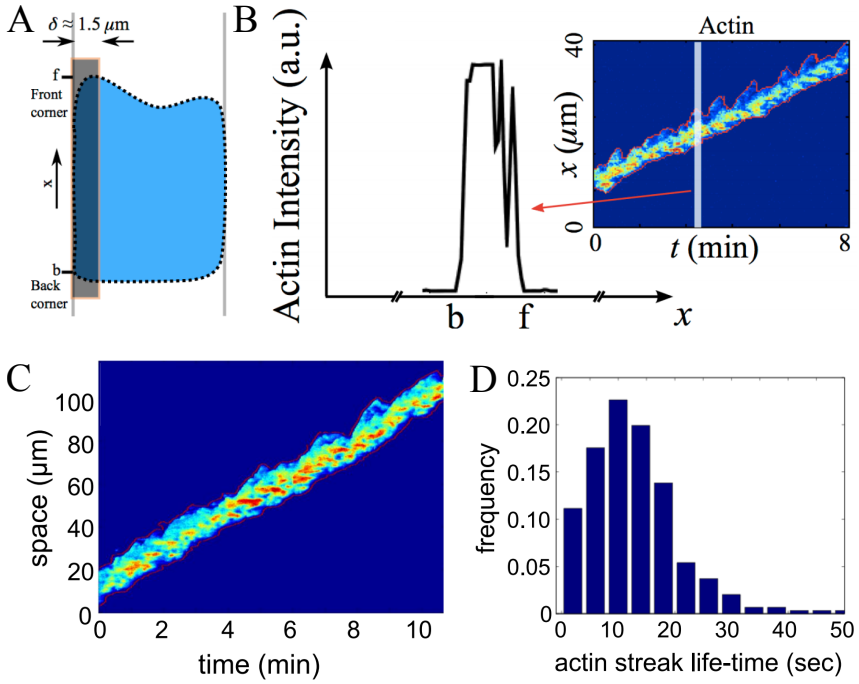

Figure 3.8: (A) Cartoon of a cell showing the definitions used in the analysis of actin polymerization. (B) A representative actin polymerization profile as a function of the position on the cell membrane in contact with the microchannel wall (averaged over δ shown in (A)). Inset shows a kymograph of these profiles. (C) Kymograph of actin polymerization profile in detail. Spatially-stationary patches of high actin polymerization are evident. (D) Duration of the spatially-stationary polymerizing actin patches. The distribution was obtained from 10 cells. (Experimental data courtesy Oliver Nagel)

stationary actin polymerization patches (defined as actin streaks). Details of the algorithm are provided in Section 3.6.2. We have measured the distribution of the lifetime of these actin streaks for n=10 cells (Fig. 3.8D). The average lifetime of the actin streaks is approximately 10 seconds. This timescale is faster than the resonance timescale of chemically-driven actin polymerization oscillations.

Our observations suggest that there are multiple mechanisms that can drive actin polymerization. Chemotaxis pathways are well studied and the connection between chemoattractant-gradient sensing biochemicals and actin polymerization has been suggested by several research groups (PIPs, PTEN, PI3K etc.) [36, 69, 78]. These studies suggest that actin polymerization is ultimately guided by the spatial asymmetry of these biochemicals. We show that compared to the chemically-guided actin polymerization, modulation of actin with physical forces is faster. Our analysis shows that physical forces that feedforward to actin polymerization have a much more direct impact on the preferential polymerization of actin, which is observed either as guided waves or spatially-stationary patches. It is likely that cells integrate chemical and mechanical signals that provide a directional cue. We will explore the interplay between these signals in the following chapters.

3.6 Methods

3.6.1 Detection and analysis of the cell boundary regions

To find the cell boundary regions that are in contact with the microchannel walls, we use a gradient-based edge detection algorithm. We first find the position

of the microchannel walls from the summed fluorescence intensities of the actin and myosin II markers. We average the summed intensity with respect to time and position x (the direction parallel to the motion of the cell). The time average gives the average contact region of the cell with the microchannel wall, and the x-average minimizes the noise. This averaging yields a typical intensity profile that is narrow and rapidly decreasing close to the microchannel wall. We find pixels that are close to the microchannel wall by selecting those which have an intensity below 1% of the total intensity. Next, we calculate the derivative of the intensity for these points. Then we look for a sudden change in the derivative by performing a unidirectional search that starts from outside the microchannel all and scans towards the cell cytoplasm. The sudden change in the derivative ranges from 0.0005 to 0.005. We choose a different value for each cell, because the fluorescence intensity of the labeled proteins depends on the expression level and varies from cell to cell.

Next, we find the front-most and back-most boundary points, where the cell is in contact with the microchannel wall, see Fig. 3.8A). At each x-position, we sum the total intensity starting from the microchannel wall over a distance of 6 pixels ($\approx$ 1.44 μm) into the cytoplasm. An example of the resulting intensity profile along the channel wall is shown in Fig. 3.8B. We next employ a similar unidirectional search as above for the locations of the anterior and posterior contact. We search for 5 consecutive points that each have an intensity above a threshold value. For each cell, we individually choose a threshold intensity in the range of [0.002, 0.005]. The time evolution of the front-most and back-most locations of the cell contact with the microchannel are shown as red outlines in the inset in Fig. 3.8B and in Fig. 3.8C

for another cell.

3.6.2 Measuring the lifetime of actin foci

To obtain the lifetime of the actin foci on the cell membrane in contact with the microchannel wall (at a given boundary position), we consider actin intensities that are greater than $\epsilon = 78\%$ of the maximum intensity (thresholding). Next, we calculate the average and the standard deviation of the intensity in the thresholded region over time. We then smooth the actin intensity using "locally weighted scatter plot smooth" method in Matlab's smooth function. We monitor the deviation of this smoothed intensity at each time point in the region from the time-averaged intensity and count the number of frames during which the deviation is within $\Delta = 2\%$ of the average intensity. The values of ϵ and Δ are picked such that the distribution obtained from one kymograph has maximum similarity with the one that is manually obtained ($p \approx 0.85$ using Kolmogorov-Smirnov test). For the remaining kymographs, we utilized the algorithm to obtain the distribution of actin foci lifetime shown in Fig. 3.8D ($n = 10$ cells).

Chapter 4: Signal relay in noisy directed migration of cell groups

4.1 Overview

Collective cell migration is observed in various biological processes including angiogenesis, gastrulation, fruiting body formation, and wound healing. *D. discoideum*, for example, exhibits highly dynamic patterns, such as streams and clumps during its early phases of collective motion, and has served as a model organism for the study of collective migration. In this chapter, facilitated by experiments, we develop a conceptual, minimalistic, computational collective migration model to analyze the dynamical processes leading to the emergence of collective patterns and the associated dependence on the external injection of a cAMP signal, the intercellular cAMP secretion rate, and the cAMP degradation rate. We demonstrate that degradation is necessary to reproduce the experimentally observed collective migration patterns, and show how our collective migration model can be utilized to uncover the basic dependence of migration modes on cell characteristics. Our numerical observations elucidate the different possible types of motion and quantify the onset of collective motion. Thus, the collective migration model allows us to distinguish noisy motion guided by the external signal from weakly correlated motion. The experiments presented in this chapter were performed by Erin Rericha.

Modeling of the experimental data was done in collaboration with my co-advisors Edward Ott and Wolfgang Losert.

The focus of this chapter is on modeling, simulating, and analyzing collective motion arising from chemotaxis and signal relay. Although collective motion, chemotaxis, and signal relay have all been investigated before, this section focuses on collective behavior in the presence of a linear gradient without fluid flow. The linear, no-flow gradient geometry has been used in conjunction with Zigmond chambers and under-agar assays but was cumbersome and often replaced with point sources, such as a micropipette, which leads to convergent cell trajectories even in the absence of signal relay. A linear gradient has been recently incorporated into a microfluidic system that can simultaneously monitor multiple gradient conditions and cell lines (using EZ-TAXIScan system (ECI, Japan) [94]). By monitoring many parallel conditions we are able to analyze signal relay and differentiate different types of collective motion. It also allows us to validate metrics for detection of collective behavior that should be useful for the analysis of a number of other investigations of cell signaling that are starting to be carried out in this signal geometry. Linear gradients have been introduced for quantitative studies of gradient sensing, but recent work in microfluidic devices has been carried out in chambers with fluid flow that flushes out signal relay (e.g., in Refs. [95, 96]).

The controlled linear gradient allows us develop a quantitative phenotype for the onset of signal relay between cells. We are able to tune the relative strength of signal relay continuously, by varying the linear gradient strength. This capability allows us to measure collective behavior based on correlations between cell

trajectories. We anticipate that our systematic studies will be valuable for a broad range of investigations of collective cell behavior. Indeed, cell trajectories in such linear gradient chambers are starting to be collected to investigate signaling pathways that regulate chemotaxis in various types of cells (e.g., *D. discoideum* [97], neutrophils [98, 99], eosinophils [100], and osteoclasts [101]).

Building on previous work [18, 102–104], we develop a minimalistic collective migration model for *D. discoideum* migration and signal relay in a linear gradient. Our collective migration model incorporates recent experimental measurements on cell migration persistence [8], independence of signal strength [18], and the migration mechanism and lag in reorientation in response to signals [11]. We use the collective migration model to study which aspects of the signal relay loop promote streaming. We find that a balance between fast secretion and degradation is needed to match experimental observations. To constrain the migration parameters, we measure the time autocorrelations and the fluctuations of the cell motion from our experimental systems. We propose the use of these metrics to find evidence of signal relay in cells that do not display streams. Our efforts are motivated by recent experiments on *D. discoideum*, that show a notable visual distinction between cells that relay signals, and cells that both relay and degrade the signal. Wild-type cells, which both emit and degrade cAMP, can form streams in which cells are aligned head to tail, whereas mutant PDE1- cells that are unable to degrade cAMP form transient, aberrant streams that lead to clusters [25].

Other models of chemotaxis focus on stochastic aspects of the cellular processes. These models discuss mechanisms that include stochastic dynamics of direc-

tional sensing and speed control [9, 102, 105–107], "memory" associated with membrane deformations [108–110], and extension of new pseudopods conditional on the locations of existing ones [91, 111]. Recent models of chemotaxis study the effects of noise due to fluctuations in receptor binding as well as the noise arising from subsequent internal responses [95, 96, 104, 112–114]. In the simplest models directional sensing is represented as stochastic dynamics of a single angular variable (which represents the density asymmetry of both the occupied receptors and further downstream processes such as PIP_3 regulation). Schienbein et al. [105] showed that the dynamics of the stochastic angle agrees well with the directional sensing dynamics of granulocytes during galvanotaxis. The stochastic angle model was also implemented for *D. discoideum* chemotaxis by including receptor kinetics and chemical gradient steepness [104]. In this work we choose to capture the stochastic effects by associating the stochasticity of the previously described angular variable with the measured fluctuations in the direction of motion.

4.2 Experimental observations

Experiments in linear chemical gradient classify the collective response of relay systems to externally imposed signals. The EZ-TAXIScan system uses an etched silicon chip to form 6 separate channels for chemotaxis experiments in a linear geometry [94]. Each channel contains two buffer wells on opposite sides of a thin, terraced gap (260 microns long, 1.2 mm wide and 5 microns deep). Cells are gently pipetted into one well and allowed to settle to the glass surface. The opposite channel is

filled with cAMP and diffusion sets a linear gradient in the channel within 5 minutes. Cells, responding to the external signal, enter the terraced region and travel 260 microns towards the other side. Parallel to the edges of the terrace are small columns (20 microns long, 8 microns apart) that set the vertical spacing, but provide little impedance to cell motion. If not modulated by cAMP or by PDE1 secreted by the cells, the imposed gradient stays constant at least for 60 minutes [94, 100]. This type of setup provides a good signaling geometry for separating the effect of intercellular communication and an imposed gradient. Fig. 4.1A and Fig. 4.1B show time lapse images of wild-type cells and mutant cells under the influence of a linear (downward in the figures) cAMP gradient. At $t = 0$ cells placed in a reservoir without cAMP begin to move into the chamber (at the top boundary in the figures). Although the cells are initially introduced uniformly in the horizontal direction (5 min panel of Fig. 4.1A and Fig. 4.1B), wild-type cells are attracted to each other and form streams (32 min panel of Fig. 4.1A), which in this example evolve to swirling groups (60 min. panel of Fig. 4.1A). The mutual attraction of the cells is due to the enzyme adenyl cyclase A (ACA) localized at the back of the cells [24]. ACA synthesizes intracellular cAMP, which diffuses into the extracellular medium. As shown in Fig. 4.1B, mutant cells (aca-), lacking ACA, do not exhibit collective motion and, throughout the time-course of the experiment, move without streaming or clumping in the direction of the external cAMP gradient.

To analyze these observed migratory behaviors, we use a cell-tracking algorithm to determine, over a short time interval Δt, displacement vectors of the position of the center of the imaged intensity of each cell. We define a motion angle

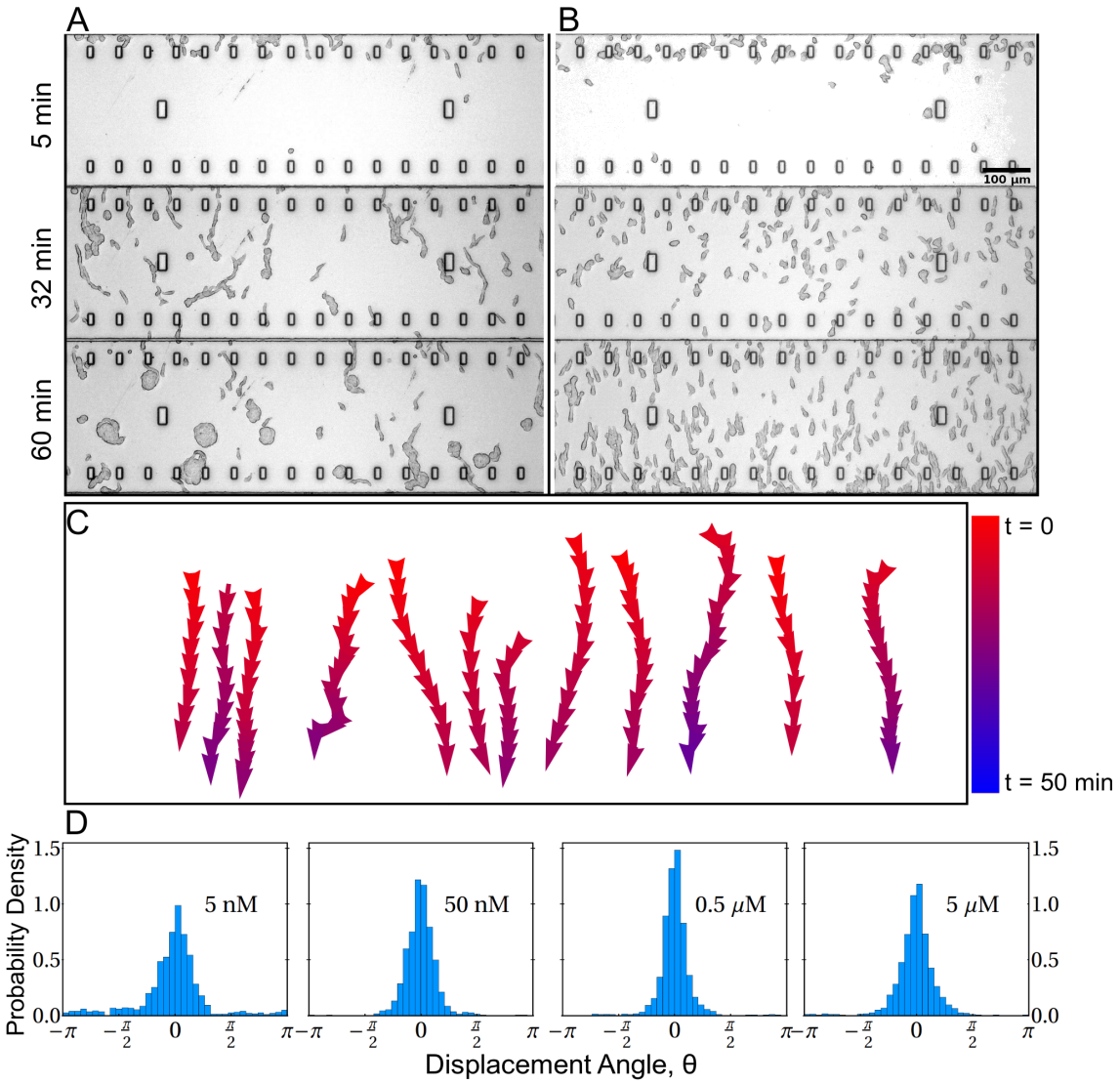

Figure 4.1: (A) Wild-type cells can relay the signal by secreting cAMP from their tails. They form streams that are unstable towards swirling clumps. (B) The mutant cells (aca-) lacking the ACA enzyme cannot secrete cAMP and thus undergo uniform motion in the direction of the external cAMP gradient. (C) Some representative tracks of aca- cells obtained with the tracking algorithm. Vector displacements along the tracks are color coded according to real time. (D) Distributions of the angle representing the displacement of cells exposed to different constant gradient amplitudes with respect to the vertical axis. The panel labels (5 nM to 5 μM) denote the cAMP concentration in the reservoir.

θ as the angle of a cell's displacement vector with respect to the imposed cAMP gradient. Fig. 4.1C shows representative tracks of cells during chemotaxis (color coded according to real time). Fig. 4.1D shows the distributions of the angle θ for aca- cells, subject to four different external cAMP gradient strengths, increasing by a factor of 10 from panel to panel. The spread of θ reflects the competition between noise and the ability of cells to sense and react to the gradient. Note that the width of the distributions first decreases with increasing gradient strength then decreases, indicating the existence of an optimum. This finding agrees with observations of Fuller *et al.* [95], which show that the chemotactic response is limited by external noise (noise due to receptor-ligand binding) for a small local cAMP concentration and by internal noise (noise due to subsequent internal signaling) for a higher local cAMP concentration.

The distributions in Fig. 4.1D show that the cells do not always orient in the direction of the extracellular gradient ($\theta = 0$). As discussed in Ref. [115], the gradient-sensing mechanism is stochastic, with many sources of noise that can cause random deviation from the direction of the external gradient. Our data for the angular distributions suggest that above a threshold gradient the cell orientation is independent of the gradient strength. Below this threshold (e.g., see the 5 nM panel of Fig. 4.1D), the width of the θ distribution increases with decrease of the gradient [95]. In the following we focus on the regime in which the cell migration is less sensitive to the gradient strength.

For several representative cells, Figs. 4.2A-C show the time autocorrelation of $C(\tau) = \langle \cos[\theta(t) - \theta(t+\tau)] \rangle - \langle \cos^2 \theta(t) \rangle$, where the angle brackets denote an

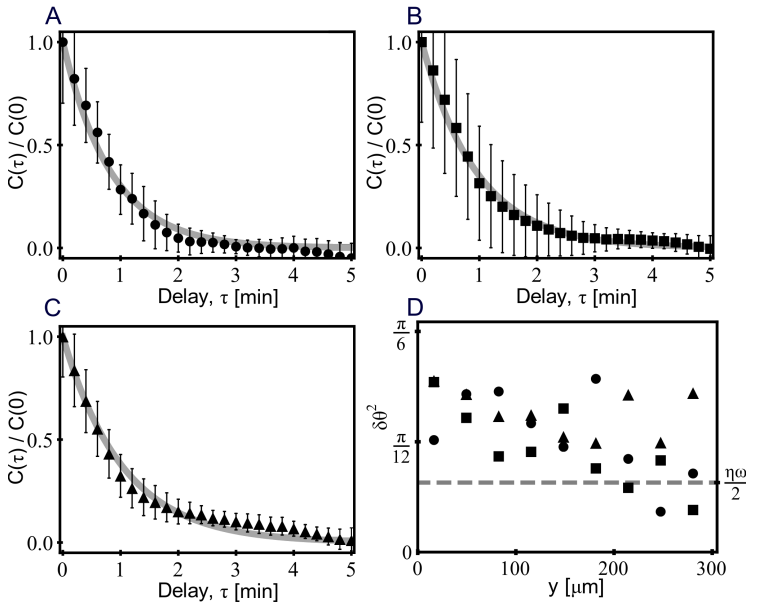

Figure 4.2: (A-C) $\langle C(\tau)\rangle$ versus τ for three different imposed cAMP gradient strengths corresponding to cAMP concentrations of 50 nM (black bullet), 0.5 μM (black square) and 5 μM (black triangle) in the reservoir on the cell exit side of the gradient chamber. The solid lines are best fits to $\langle C(\tau)\rangle = e^{-\tau/\tau_0}$ yielding values for τ_0 of 0.84 min, 0.94 min and 1 min. Autocorrelations are obtained from $n = 33$, $n = 47$, and $n = 79$ cells, respectively. Error bars represent the standard deviation. (D) The variance $\langle C(0)\rangle \cong \delta\theta^2$, versus the distance y from the cell input side of the gradient chamber for the three gradient strengths in Figs. 4.2A-C is plotted using the same symbols black bullet, black square and black triangle.

average over time for cells that are located in the region between the cell exit plane and the mid plane of the gradient chamber (lower half of the panels in Figs. 4.1A and B, (the number of cells are $n = 33$, $n = 47$, and $n = 79$, respectively)). The reason for restricting the averaging to the half of the chamber on the cell exit side is to eliminate any bias of the cell orientation angle distribution due to influence of the process of entry into the chamber. For small angles ($\cos\theta \approx 1 - \theta^2/2$) the autocorrelation is $C(\tau) \approx \langle\theta(t)\theta(t+\tau)\rangle$. The variance of θ, $\delta\theta^2 \approx C(0)$, is plotted as a function of the distance from the starting point of the cells in Fig. 4.2D for the three different gradient strengths. In the next section we develop a collective migration model that estimates the level of the fluctuations in the displacement (dashed line in Fig. 4.2D). Previous studies on eukaryotic *HaCaT* cells highlight the dependence of velocity autocorrelations on two time scales [108]. Nevertheless, we see from Figs. 4.2A-C that $\langle C(\tau)\rangle$ can be well fitted to a dependence of the form $e^{-|\tau|/\tau_0}$ parametrized by the single characteristic time τ_0. The fits for the average correlations $\langle C(\tau)\rangle$ for the individual gradient strengths are displayed in Figs. 4.2A-C. The single time scale, τ_0, is approximately constant over the two orders of magnitude in the external cAMP gradient strengths ($\tau_0 = 0.84$ min, 0.94 min and 1 min for Fig. 4.2A, Fig. 4.2B, and Fig. 4.2C). This time scale is roughly consistent with the dynamics of contractions of cells [53].

4.3 Modeling signal relay

Modeling collective migration of *D. discoideum* in a linear gradient chamber enables quantitative description of collective responses to externally imposed signals. The characteristic size of eukaryotic cells is an order of magnitude larger than that of bacterial cells. In contrast to bacterial cells, eukaryotic cells can sense the difference in chemoattractant concentration between the front and the back of a cell, thus detecting spatial gradients without moving. For *D. discoideum*, gradient sensing is accomplished via a G-protein coupled receptor and downstream signaling pathways [36]. Models of chemotaxis treating the cAMP signal transduction mechanism, including the biochemical details such as receptor desensitization [44] and adaptation [116], demonstrate the emergence of the experimentally observed cAMP waves. In this dissertation our modeling approach will differ somewhat from past works (e.g., Refs. [19, 45, 47, 117]) in that we seek a collective migration model that is simple enough that its relatively few parameters can be inferred from experiments, yet is still capable of capturing the distinctions between streams and clumps seen in our experiments on *D. discoideum*.

We model cells as self-propelled soft disks of radius $r_0 = 7.5\mu$m. For each cell i we specify the location of its center and its orientation by the two-dimensional vectors $\mathbf{r}_i(t)$ and $\mathbf{n}_i(t)$ (by definition $|\mathbf{n}_i| = 1$). We specify locations of the cells using a Cartesian coordinate system, where the chamber in which the cells move is located in $0 \leq y \leq L_y$. In the experiment, the chamber boundaries, $y = 0$ and $y = L_y$, have perforations and are thus permeable to transport of cells and

cAMP. The speed of each cell, v_0, is assumed to be well-approximated as constant in time ($12\mu m/\text{min}$), independent of signal strength, in agreement with controlled chemotaxis experiments [8]. The cAMP concentration field is denoted $C(x, y, t)$. In the experiment the cells are deposited in a large reservoir (corresponding to $y < 0$ in the collective migration model) in which there is no externally injected cAMP. This experimental condition is modeled by a Dirichlet boundary condition on the cAMP concentration, $C(x, 0, t) = 0$ at $y = 0$, and by introducing individual discrete cells at $y = 0$ with a uniform flux J_D cells per unit time per unit length in x (each newly introduced cell's orientation is initially in the $y-$ direction). In addition, the experiment has an aqueous solution of cAMP in a large reservoir on the other side of the chamber (corresponding to $y > L_y$ in the collective migration model), and the cAMP concentration in this reservoir stays constant during the course of the experiment. This is modeled by a Dirichlet boundary condition at $y = L_y$, $C(x, L_y, t) = C_0$, along with the removal of cells when they reach $y = L_y$. We applied periodic boundary conditions in x, such that $C(x, y, t) = C(x + L_x, y, t)$ and each cell that leaves the chamber at a lateral boundary, $x = 0$ or at $x = L_x$, reenters the chamber at the other end. Using these definitions, we propose the following minimal, agent-based collective migration model for cell motion in our experimental setup,

$$\frac{d\mathbf{r}_i}{dt} = v_0\mathbf{n}_i \tag{4.1}$$

$$\frac{d\mathbf{n}_i}{dt} = \omega\mathbf{n}_i \times \left[\left(\frac{\nabla C}{|\nabla C|} + \boldsymbol{\xi}_i + \mathbf{f}_i\right) \times \mathbf{n}_i\right] \tag{4.2}$$

$$\frac{\partial C}{\partial t} \;=\; D\nabla^2 C - \nu C + s\sum_i \delta(\mathbf{r}-\mathbf{r}_i)\,. \tag{4.3}$$

The equation (4.1) corresponds to the constant speed assumption. The equation (4.2) dictates that the unit vector specifying the cell's orientation $\mathbf{n}_i(t)$ is attracted toward the direction of the vector,

$$\mathbf{g}_i(t) = \frac{\nabla C}{|\nabla C|} + \boldsymbol{\xi}_i + \mathbf{f}_i\,, \tag{4.4}$$

with relaxation time ω^{-1}. This relaxation time may be thought of as including both the chemically determined time for a cell to 'perceive' the gradient, as well as the time it takes the cell to mechanically turn its orientation. The first term in $\mathbf{g}_i$ is a unit vector in the direction of the cAMP gradient. Note that, in accord with the observed similarity of the second, third, and fourth panels of Fig. 4.1D, this term is independent of the level of cAMP (i.e., invariant to the transformation $C(x,y) \to (\text{const.}) \times C(x,y)$). The second term $\boldsymbol{\xi}_i = (\xi_i^x, \xi_i^y)$ in $\mathbf{g}_i$ is white noise,

$$\langle \xi_i^l(t)\rangle = 0\,, \quad \langle \xi_i^l(t)\xi_{i'}^{l'}(t')\rangle = \eta\delta_{ii'}\delta_{ll'}\delta(t-t') \quad ; \quad l \in \{x,y\}\,. \tag{4.5}$$

The third term $\mathbf{f}_i$ in $\mathbf{g}_i$ is a repulsive 'force' modeling a soft two-body contact interaction between neighboring cells,

$$\mathbf{f}_i = f_0 \frac{\hat{\mathbf{f}}_i}{|\hat{\mathbf{f}}_i|}\,, \quad \hat{\mathbf{f}}_i = \sum_{\mathbf{r}_j \in \mathcal{S}_i} \frac{\mathbf{r}_i - \mathbf{r}_j}{|\mathbf{r}_i - \mathbf{r}_j|}\left(1 - \frac{|\mathbf{r}_i - \mathbf{r}_j|}{2r_0}\right)\,, \tag{4.6}$$

where $\mathcal{S}_i$ is the region $|\mathbf{r} - \mathbf{r}_i| \le 2r_0$. In Eq. (4.6) we have taken the form of the repulsive force to decrease linearly with distance from the center of the cell. We have

also tried other forms for the $|\mathbf{r}_i - \mathbf{r}_j|$ dependence of the repulsive force and found that no qualitative differences occurred. Szabo *et al.* [118] and Chate *et al.*, [119] discussed the effect of adding cohesive (i.e., attractive) forces in modeling tissue cells. The parameter f_0 determines the strength of the repulsion force.

Eq.(4.3) is the diffusion equation governing the evolution of the distribution of the cAMP density, with constant diffusivity $D = 400\mu\text{m}^2/\text{sec}$ [120]. The parameter s is the cAMP secretion rate of a cell. The cAMP decays at a rate ν, which can be spatially nonuniform and is approximately proportional to the concentration of the degradation enzyme phosphodiesterase PDE1 [48]. We introduce a degradation inhomogeneity suitable for our experimental setup in the following section.

4.3.1 Role of degradation in signal relay

cAMP degradation has a non-linear profile due to the experimental conditions. The cAMP degradation rate ν in Eq. (4.3) is meant to account for the presence of the cAMP-degrading enzyme PDE1, with ν assumed to be proportional to the enzyme density C_{PDE1}. Since PDE1 is secreted by the cells themselves and then diffuses, we can expect that C_{PDE1}, and hence ν, are time- and space-dependent quantities obeying an equation similar to Eq. (4.3) for the cAMP density $C(x, y, t)$, but with the term analogous to the degradation in Eq. (4.3) omitted. In the interest of simplicity, for our minimalist collective migration model, we wish to circumvent a full time-dependent diffusion equation model for C_{PDE1}. Instead, we assume that a time-independent steady state that is homogeneous in x is established for the C_{PDE1}

(we show in Appendix C.1 that this assumption is justified for the conditions of our experimental setup). This situation corresponds to ν depending on y but not x and t, $\nu = \nu(y)$. Furthermore, in steady state, the x-averaged cell flux in the y-direction must, by conservation of cell number, be independent of y in the linear gradient chamber, and its value everywhere in the chamber must be the same as the cell injection flux J_D at $y = 0$. In the simplest case, without clumps, the $x - t$ averaged density of cells in the external linear gradient region will thus be roughly uniform in y and of the order of J_D/v_0. Thus the $x - t$ averaged PDE1 density $\bar{C}_{\mathrm{PDE1}}(y)$, satisfies a one-dimensional, time-independent diffusion equation of the form

$$D_{\mathrm{PDE1}} \frac{d^2}{dy^2} \bar{C}_{\mathrm{PDE1}} + S_{\mathrm{PDE1}} = 0 \,. \tag{4.7}$$

Here we approximate S_{PDE1} as constant in y and given by $s_{\mathrm{PDE1}} J_D/v_0$ where s_{PDE1} is the production rate of the PDE1 per cell per unit time; D_{PDE1} is the diffusivity of the PDE1 and is approximately 100 $\mu\mathrm{m}^2/\mathrm{sec}$ [121]. In addition, we will argue that the appropriate boundary conditions on the PDE1 density are $\bar{C}_{\mathrm{PDE1}}(y) = 0$ at $y = 0$ and $y = L_y$. Solution of Eq.(4.7) with these boundary conditions leads to the model,

$$\nu(y) = 4\nu_0 \frac{y}{L_y} \left(1 - \frac{y}{L_y}\right) . \tag{4.8}$$

That is, $\nu(y)$ varies parabolically in y; $\nu(0) = \nu(L_y) = 0$, and has its maximum value ν_0 in the center of the chamber, $y = L_y/2$. In our numerical explorations we mostly use the model for cAMP degradation given in Eq. (4.8). We also note that

in other experiments, depending on the experimental setup, $\nu(y)$ may have different dependence on y. For comparison, we repeated our numerical runs with the spatially constant form $\nu(y) = \frac{2}{3}\nu_0$, where the numerical prefactor (2/3) is chosen so that the total amount of PDE1 in $0 \leq y \leq L_y$ is the same as for Eq. (4.8) (i.e., $\int_0^{L_y} \nu dy$ is the same). The spatially constant form for ν was used in other models of *D. Discoideum* chemotaxis [19, 44, 45, 47]. The results (shown in Appendix C.3) are qualitatively similar to the results presented here.

We now outline how we motivate the use of the boundary conditions

$$C_{\mathrm{PDE1}}(0) = C_{\mathrm{PDE1}}(L_y) = 0 \tag{4.9}$$

(more detailed quantitative justification is given in Appendix C.1). In our experiments, cells are placed in the reservoir located at $y < 0$. The cells then rapidly sink to the bottom of the reservoir ($z = 0$). The reservoir has a vertical thickness that is more than 2×10^3 times larger than the vertical thickness of the linear gradient chamber. The same dimensions apply for the reservoir in $y > L_y$. The bottom glass surface ($z = 0$) of the reservoir at $y < 0$ extends into $y > 0$, where it forms the bottom plane of the linear gradient chamber and of the reservoir in $y > L_y$. Cells that are on the bottom of the $y < 0$ reservoir supply a source of cells for entry at $y = 0$ into the linear gradient chamber. The cAMP-degrading-enzyme PDE1, secreted by cells in the $y < 0$ reservoir are assumed to be transported vertically upward by small convection flows in the reservoir fluid into the vertically large region $z > 0$ of the reservoir. In contrast, the distribution of the PDE1 emitted by the

cells in $0 \leq y \leq L_y$ is constrained to the much thinner vertical region defined by the chamber dimensions. Thus, in the linear gradient chamber the PDE1 density cannot be attenuated to low levels by spreading vertically. As shown quantitatively in Appendix C.1, based on this consideration, the enzyme density in $y < 0$ and $y > L_y$ is much less than in the interior of the chamber. This situation leads to our previously stated approximate boundary conditions, $C_{\mathrm{PDE1}}(0) = C_{\mathrm{PDE1}}(L_y) = 0$, used in obtaining Eq. (4.8).

4.3.2 Normalization of parameters

In order to systematically determine the essential dependence of the behavior of the collective migration model on its parameters, we introduce appropriate nondimensional variables. We define the dimensionless spatial coordinates (x', y') by $x' := x/L_y$ and $y' := y/L_y$. The dimensionless time scale t' is defined as $t' := \omega t$, and the dimensionless cAMP density C' is defined as $C' := C/C_0$. With the rescaled variables, the cAMP boundary conditions become, $C'(1, t') = 1$ and $C'(0, t') = 0$. Additionally, the white noise is transformed to $\langle \xi_i(t'_1)\xi_i(t'_2)\rangle = \eta'\delta(t'_1 - t'_2)$, where $\eta' := \omega\eta$. The collective migration model equations with the rescaled variables and Eq. (4.8) for $\nu(y)$ can now be written as

$$\frac{d\mathbf{r}'_i}{dt'} = v'_0\mathbf{n}_i \tag{4.10}$$

$$\frac{d\mathbf{n}_i}{dt'} = \mathbf{n}_i \times (\mathbf{g}_i \times \mathbf{n}_i) \tag{4.11}$$

$$\frac{\partial C'}{\partial t'} = D'\nabla'^2 C' - 4\nu'_0 y'(1 - y')C' + \tfrac{s'}{N}\textstyle\sum_i \delta(\mathbf{r}' - \mathbf{r}'_i)\,, \tag{4.12}$$

where $v_0' := v_0/(\omega L_y)$, $D' := D/(\omega L_y^2)$, $\nu_0' := \nu_0/\omega$, $\bar{N} := J_D L_y^2/v_0$, and $s' := sJ_D/(\omega C_0 v_0)$. The integral of the summation $\sum_i \delta(\mathbf{r}'-\mathbf{r}_i')$ over the square $0 \leq x' \leq 1$, $0 \leq y' \leq 1$ is the number of cells in the unnormalized square $0 \leq x \leq L_y$, $0 \leq y \leq L_y$ and is roughly equal to $\bar{N}$. In the situations we investigate $\bar{N}$ is always large compared to unity. Thus the term $\bar{N}^{-1}\sum_i \delta(\mathbf{r}' - \mathbf{r}_i')$ roughly plays the role of a normalized density whose nominal value is one. With these normalizations, the parameters in our collective migration model are $D', \nu_0', s', v_0', \eta'$, and $\bar{N}$. We wish to explore the variation of the system behavior as a function of parameters. This task is clearly an impossible task to carry out for the full set of 6 dimensionless parameters. Thus, we now seek to restrict our detailed considerations to the parameters whose influence is, we think, the most interesting. If we regard ω for the cells as fixed, then the parameter D' is dictated by the experimental setup. Experimentally, the typical cell speed v_0, and hence v_0', is observed to be roughly the same for wild-type, and mutant cells [8], and we therefore take v_0' as fixed. The noise term η' will be fixed by the experimental observations (e.g., Fig. 4.1D), which imply that it does not vary significantly across the different experimental conditions investigated (see Appendix C.2). Thus, we will keep D', v_0' and η' fixed at the appropriate estimated values. Furthermore, we expect that the qualitative behavior of the system will be insensitive to the precise value of $\bar{N}$ so long as $\bar{N} \gg 1$ (the situation in which we are interested). Thus our main numerical collective migration model explorations will focus on how the collective migration model behavior depends on ν_0' and s'.

We now further discuss our reason for interest in varying ν_0' and s'. First, with respect to ν_0', in reference [25] a genetic perturbation to the cells resulted in mutants

lacking the ability to produce the degradation enzyme PDE1 (but still emitting cAMP). In our collective migration model this situation corresponds to setting $\nu_0' = 0$. In our numerical experiments we will explore a continuous dependence on ν_0', partly because ν_0 is not well determined, but also to understand the difference between mutant cells that do not emit PDE1 (i.e., pdsA-/PEC cells) and wild-type cells. We also suggest that it may be useful for future experiments to explore continuous dependence on PDE1 secretion rate (i.e., ν_0') which might be realized by introducing a mixture of wild-type and mutant PDE1- cells. Regarding variations of s', we note that the secretion of cAMP from cells s, is biologically inhibited for another type of mutant, the aca- cells. Also, in our experiments, we change the external concentration of cAMP, C_0. The biological and chemical changing of the parameters, s and C_0, both yield change of $s' = sJ_D/(\omega C_0 v_0)$. (Also, s' could be tuned by changing the $y < 0$ reservoir cell density and hence J_D, but we have kept J_D constant in our experiments.)

4.3.3 Parameters

Aside from s and ν_0 the parameters we used in our simulations are summarized in Table 4.1. We assume that the cell parameters in this table (i.e., r_0, v_0, D, ω, η, f_0) are the same for wild-type cells ($s \neq 0$) and mutant cells ($s = 0$). In the absence of mutual attractions through cellular secretion of cAMP, a Fokker-Planck version of Eqs.(4.1)-(4.6) can be solved analytically (see Appendix C.2), and $\eta\omega$ in Eq. (4.5) can be determined by matching the analytical result to experimental

observations of mutant cells. Also, we estimate ω as being of the order of τ_0^{-1} as determined from our experimentally observed time-autocorrelation of the orientation vector (Fig. 4.2A), where τ_0 is defined at the end of the previous section. This time scale is comparable to the contraction rate of *D. discoideum* cells, which in the work of Satulovsky *et al.* [53] is considered as the bulk relaxation time. We note that the real cells' secretion rates of cAMP and of PDE1 are not well quantified and can be varied by drug treatment or by the use of mutant cells. Thus, we will regard s and the PDE1-level-dependent parameter ν_0 as variable parameters and investigate how the dependence of the collective cell dynamics depends on them.

Table 4.1: Parameters used in the numerical simulations

Symbol	Description	Value
r_0	Cell radius	7.5 μm
v_0	Self-propulsion speed	12 μm/min
D	Diffusion constant of cAMP	0.024 mm^2/min
ω^{-1}	Response time	1 min
η	Amplitude of Gaussian white noise	0.33 min
f_0	Repulsive force constant (dimensionless)	$\sqrt{10}$
L_x	Width of the simulation box	1 mm
L_y	Length of the simulation box	0.33 mm

Except for the force constant f_0, all the cell parameters in this table (i.e., r_0, v_0, D, ω and η) are obtained from experiment. The response time is obtained from the autocorrelations of the displacement vector. The noise amplitude η was calculated from the variance of the θ distribution, where the angle θ represents the orientation of the associated displacement vector.

4.3.4 Comparison between experiment and collective migration model results

Results of numerical simulations capture experimentally observed migration patterns. The collective migration model equations, Eqs. (4.1)-(4.6) are simulated numerically. Figs. 4.3A-4.3C show representative cell tracks for three different values of the normalized cAMP secretion rate s'. For all three of these cases ν_0' is fixed at $\nu_0' = 2.25$, which we estimate to be consistent with previous experimental measurements [44]. The color at a given point on a cell track in Figs. 4.3A-4.3C indicates the time that the cell making the track was at that point; red corresponds to the beginning of the simulation and blue corresponds to the end of the simulation. Figs. 4.3D-4.3F show representative snapshots, where the position and the orientation $\mathbf{n}$ of the cell is indicated by an ellipse (at normalized time $t' = 71$ for D, E, and F). In the top panels of Fig. 4.3 (Figs. 4.3A and 4.3D), the relative cAMP secretion rate is small (i.e., $s' \ll 1$). This regime mimics the aca- mutant cells, and our numerical results agree qualitatively with the experimental observations of aca- cells (cf., 32 min panel of Fig. 4.1B). For larger values of s', and depending on t', our numerical results can be classified under two main categories, streams (Fig. 4.3E) and clumps (Fig. 4.3F). At moderate s' (Fig. 4.3E) streams are evident. At higher s', Fig.4.3F shows that multiple clumps of cells form. From the corresponding tracks of cells shown in Fig. 4.3C, it is seen that the cells stay within the clumps and the clumps have almost no motion in the y' direction.

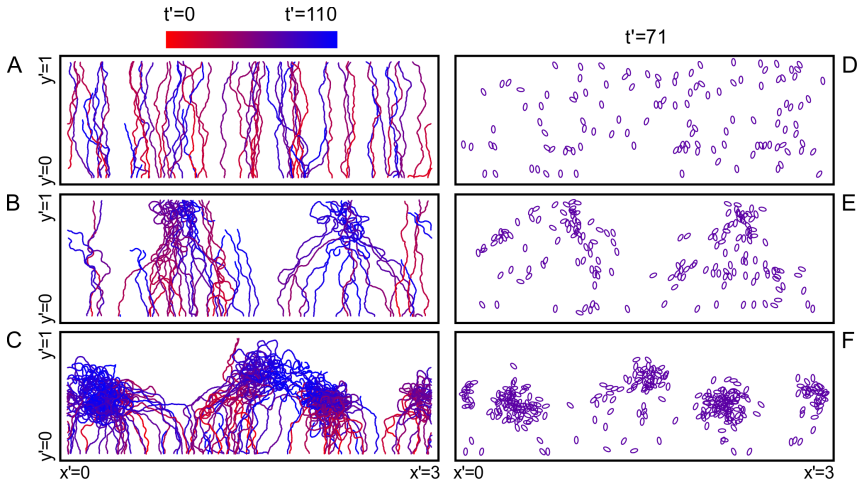

Figure 4.3: (A) For a relatively slow cAMP secretion rate ($s' = 0.083$) the cells move independently, showing no sign of collective motion. (B) If the cAMP secretion is moderate ($s' = 0.665$) cells form streams. (C) For high relative cAMP secretion rate ($s' = 1.327$) cells exhibit aggregation and therefore form clumps. Panels (D-F) are snapshots from the same simulations exhibiting the spatial organization of the cells.

Dynamics of collective migration is quantified by the mean progression speed and the cell density. To go beyond the visual comparison of our simulation results with our experimental observations, a quantitative description of the three modes of group cell motion described above (i.e., uncorrelated motion, streams, and clumps) is desirable. We define the normalized mean progression $M(y', t')$, by $M(y', t') = |\langle \mathbf{n}(t') \rangle|$, where the angle brackets denote an average of cells in the region between $y' - \Delta/2$ and $y' + \Delta/2$, where $\Delta = 0.05$ (cf., [122, 123]). We denote by $\widetilde{M}(t')$ the average of $M(y', t')$ over $0 \leq y' \leq 1$, and we denote by $\overline{M}(y')$ the time average of $M(y', t')$ taken over the last quarter of the simulation ($82.5 < t' < 110$). Another useful measure is the normalized averaged cell density $\overline{\rho}(y')$, computed by averaging over the region $y' - \Delta/2$ to $y' + \Delta/2$ with $\Delta = 0.05$ and normalized so that $\int_0^1 \overline{\rho}(y') dy' = 1$.

First, Fig. 4.4A shows the ensemble average of $\widetilde{M}(t)$, denoted by $\widetilde{M'}(t)$, for the aca- cell experiment (in gray) and for a single model simulation (in black). The collective-migration model parameters for the run are $\nu_0' = 2.25$ and $s' = 0.033$, which correspond to the aca- mutant cells. To make a fair comparison, for the experimentally obtained $\widetilde{M'}(t)$ we filtered out cells that move at a slower speed than what we considered in our collective migration model (i.e., $v < v_0$). We calculate $\widetilde{M'}(t)$ for a group of randomly selected cells in the $0 < y' < 1$ region. Since our tracking algorithm cannot track all the cells available in this region, the experimentally obtained $\widetilde{M}(t)$ is represented by this ensemble average. To compare our experimental result to our numerical simulation results, we calculate $\widetilde{M'}(t)$ from our simulation by sampling cells in the simulation so as to match the number of cells for which $\widetilde{M'}(t)$ is experimentally calculated.

We show in Figs. 4.4B and 4.4C how $\overline{M}(y')$, and $\overline{\rho}(y')$ vary with the distance from the cell reservoir, y', for the three values of s' used to obtain the cell tracks shown in Fig.4.3 with ν_0' fixed at the same value used for Fig. 4.3. In these plots, $\overline{M}(y')$, and $\overline{\rho}(y')$ are averaged over several runs (this average is denoted by $[\widetilde{M}(t)]$), where the error in the mean is shown by vertical error bars, which is calculated by the standard deviations of the runs divided by the square root of the number of runs. In the low s' regime (solid curves in Figs.4.4B and 4.4C), corresponding to Figs. 4.3A and 4.3D, Fig. 4.4A shows that, $\overline{M}(y')$ saturates to 0.9 in the upper half of the gradient chamber, $y' \gtrsim 0.5$, whereas Fig. 4.4B shows that $\overline{\rho}(y') \cong 1 \pm 10\%$ is approximately uniform. The density profiles measured from the time lapse images (a rough estimate calculated from the image intensity) are in fair agreement with

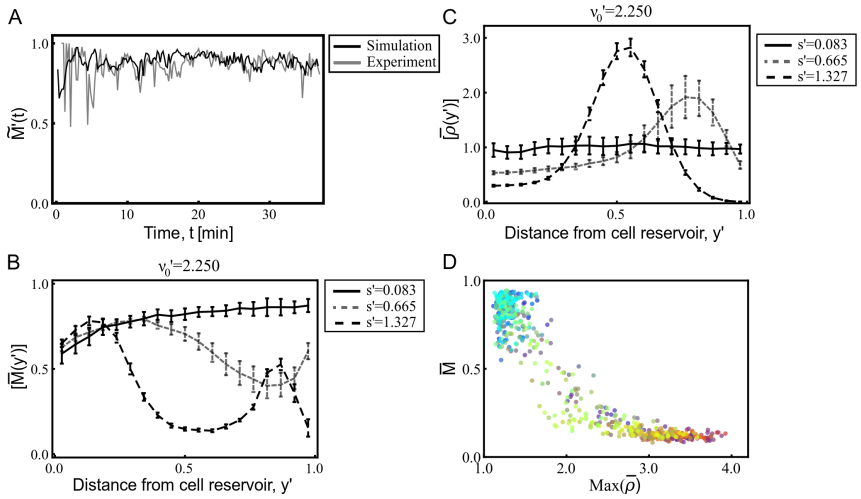

Figure 4.4: (A) $\widetilde{M}(t)$ is used to compare experimental data (aca- with $C_0 = 5\mu$M) with a representative single run that is obtained with collective-migration model parameters that mimic the experimented acamutant cells. (B) and (C) show respectively, $\overline{M}(y')$, and $\overline{\rho}(y')$ as a function of the distance from the cell reservoir for $\nu_0' = 2.25$, and three different cAMP secretion rates. Error bars are obtained from different realizations with the same simulation parameters for each curve and represent the standard error of the mean. (D) The maximum $\overline{\rho}(y')$ in the region $y' > 0.5$ is plotted against its corresponding $\overline{M}(y')$. Each point corresponds to a single numerical run. For (A), when the cells enter the chamber at $y' = 0$, we initialize the cell orientation vectors $\mathbf{n}_i$ for cell i according to a distribution of the angle θ with respect to the $y-$axis, where this distribution is uniform in the range, $-\pi/2 < \theta < \pi/2$. This process is used for approximate matching of the experimental $\widetilde{M}(t)$ at $t \cong 0$.

those obtained from our simulations. For PDE1- cells, our collective migration model suggests that the cAMP secretion levels are small compared to those of the wild-type cells exposed to the same imposed gradient. The density profiles measured from the time lapse images (a rough estimate calculated from the image intensity) are in fair agreement with those obtained from our simulations. For PDE1- mutant cells, our collective migration model suggests that the cAMP secretion levels are small compared to the wild-type cells exposed to the same imposed gradient. In determining the cAMP secretion rate we assumed same noise level compared to the wild-type cells. Therefore, in conjunction with findings from our collective migration model, our experimental observations suggest that the lack of degradation of external cAMP results in either reduced signal relay or increased noise level in gradient sensing (corresponding to receptor desensitization). The comparison and the details of the density estimate are shown in Appendix C.4.

As shown in Figs. 4.3B and 4.3E, for $t' = 71$, streams emerge in the regime of moderate s' (plotted as the gray dashed curves in Figs. 4.4B and 4.4C). These streams start to aggregate in the upper half of the gradient chamber, which results in a decrease in $\overline{M}$ and a corresponding increase in $\overline{\rho}$. Compared to the low s' regime, the streams cause an increase in the cell density (the peak at $y' \cong 0.8$).

In the high s' regime (plotted as the black dashed curves in Figs. 4.4B and 4.4C), $\overline{\rho}(y')$ is even more peaked than in the moderate s' regime. This situation apparently leads to a peak in the cAMP density which leads cells to start aggregating in the lower half of the gradient chamber. Streams form close to the reservoir, where cells enter the gradient chamber. To form streams, newly entering cells acquire

laterally (x-directed) converging velocity components. Because the cell speeds are fixed at v_0, $\overline{M}(y')$ decreases (see the region $0.2 \lesssim y' \lesssim 0.5$ in Fig. 4.4B) and $\overline{\rho}(y')$ increases. This situation apparently leads to a more localized secretion of cAMP, which overcomes the externally imposed cAMP concentration causing the clumping seen in Figs. 4.3C and 4.3F.

In Fig. 4.4D the maximum $\overline{\rho}(y')$ in the region $0.5 \leq y' \leq 1$ is plotted versus the corresponding $\overline{M}(y')$. Each point in this figure is obtained from a single numerical run. The points are color coded with respect to the ν_0' and s' used in the numerical run. Fig. 4.4D shows that points are clustered in two regions. The first region, in which ρ is large and M is small [($\rho \gtrsim 3$), $M \lesssim 0.3$], corresponds to large clumps, while the second region, in which ρ is small and M is large [($\rho \cong 1$), $M \cong 0.9$], corresponds to the uncorrelated motion. The points between these two regions correspond to runs in which cells form streams that either generate clumps (i.e., points closer to the first region) or move through the $0.5 \leq y' \leq 1$ region and leave the gradient chamber (i.e., points closer to the second region).

Stream formation is robust when external cAMP is degraded. We explored the effect of the two timescales, the cAMP degradation rate and the local cAMP production rate, ν^{-1} and s^{-1}, respectively. Fig. 4.5 shows results for $M(y', t')$ averaged over $0 \leq y' \leq 1$ and $82.5 \leq t' \leq 110$ (i.e., the last quarter of the simulation), as well as over a large number of model simulations (~ 1000). These averages are labeled $\{M\}$ in the figure. The top panel of Fig. 4.5A shows $\{M\}$ as a function of s' for $\nu_0' = 2.25$. Fig 4.5A shows that $\{M\}$ decreases as s' increases. In the region

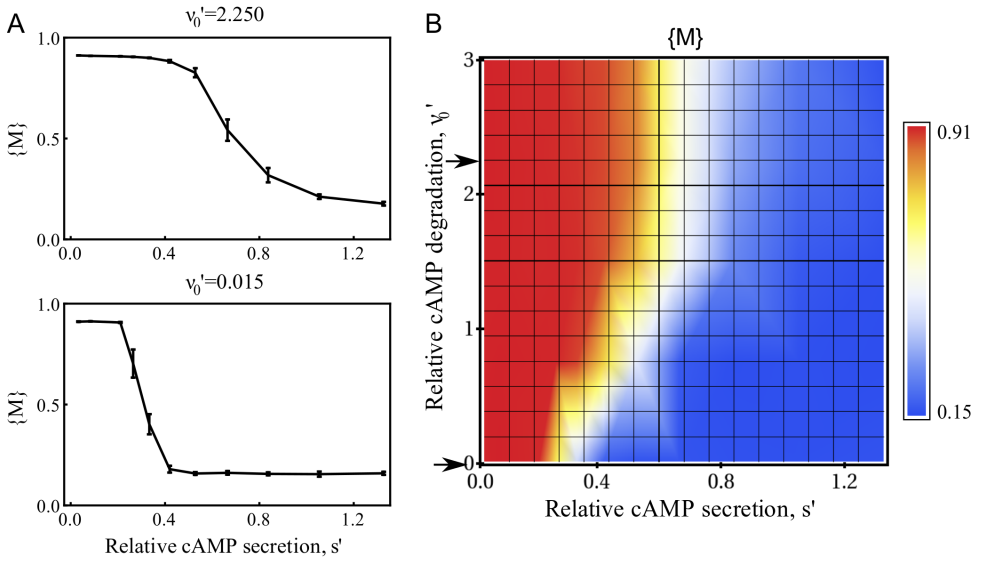

Figure 4.5: (A) $\{M\}$ as a function of s'. Error bars are obtained from multiple numerical realizations (between $10-30$) and represent the standard error of the mean. In the top panel, the degradation rate is comparable to the experimentally obtained degradation rate of the phosphodiesterase. In the bottom panel, we used a small cAMP degradation rate to model mutant PDE1- cells, which are incapable of secreting the enzyme that degrades cAMP. (B) $\{M\}$ as a function of the relative cAMP secretion and relative cAMP degradation rates. The red regions correspond to uncorrelated motion. The dynamically unstable regions of the (ν_0', s') phase space, in which streams are likely to form, are labeled with yellow and white. Blue regions are associated with aggregate formation.

$0.8 \gtrsim s' \gtrsim 0.5$, where $\{M\}$ decreases fastest, streams occur, but clumps are rare (e.g., Figs 4.3B and 4.3E). The bottom panel of Fig. 4.5A is for a small value of ν_0' (0.015), to model mutant cells that cannot degrade cAMP. In this case we see that there is a sharp decrease in $\{M\}$ in the range $0.3 \gtrsim s' \gtrsim 0.2$. Below this range the simulations show roughly uniform cell density, whereas above this range clumps occur. Compared to the slow degradation regime, in the fast degradation regime (top panel of Fig. 4.5A) the streaming behavior is robust. In the slow degradation regime, the streams form for only a short period, which is followed by formation of clumps. Recent experiments demonstrate that stream formation is impaired if cells cannot degrade external cAMP [25]. Fig. 4.5B summarizes results for our simulations (color coded), as a function of s' (plotted on the horizontal axis) and ν_0' (plotted on the vertical axis). The data in the top (bottom) panel of Fig. 4.5A correspond to a horizontal cut through Fig. 4.5B at the arrow, $\nu_0' = 2.25$ (0.015), on the vertical axis of Fig. 4.5B. Fig. 4.5B shows that the width of the range of s' in which streams occur decreases as ν_0' is lowered. Additionally, the onset of stream generation with respect to s' becomes smaller with decreasing ν_0'.

4.4 Discussion

Our collective migration model explains different observed modes of collective motion of motile cells. Our main new finding is that signal relay alone is not enough to arrange migrating cells into collectively moving streams. However, when the signal is both relayed and also degraded, stable streams form. Our collective migration

model is minimal, involving a relatively small number of potentially experimentally deducible parameters.

Based on our numerical results, we suggest experiments in which the transition between streaming and clumping can be experimentally tested by changing the effective values of our collective-migration model parameters. One suggestion is that the value of ν can be effectively reduced by either mixing wild-type and PDE1-mutants or by changing the amount of PDE1 added during the PDE1- mutant cell development.

The relaxation time ω^{-1} obtained from our experimental observations is associated with the membrane retraction time scale. In addition, the time scale corresponding to the noise amplitude $\eta \approx 20$ sec is associated with the formation time of pseudopods [90]. These parameters could be altered by adding drugs or changing the developmental procedures. For example, introducing a drug that inhibits the PI3 kinase reduces the pseudopod generation frequency [90] and hence both ω and η^{-1}. Additionally, recent studies show drastic change in the collective motion behavior of wild-type cells when they are prepared over a longer development time [124]. In this case ω and η^{-1} are reduced in agreement with the observed reduction of stream formation [124]. Thus, we believe that our collective migration model can be utilized to quantify changes in the collective motion in response to modifications of cell characteristics.

In our collective migration model, we have focused only on the extracellular cAMP dynamics given in Eq. (4.3), with the objective of reproducing the patterns in Fig. 4.1 with as few physical processes as possible. We modeled the motion of the

cells according to the the dynamics of sensing the signal with the phenomenological equation (4.2). Models that include additional processes are capable of explaining additional phenomena. E.g., models of cAMP signal transduction including receptor desensitization [44] and adaptation [116] show the generation of experimentally observed cAMP waves including spiral waves [19,103,117]. In addition, the observed rotating vortex structure of the aggregates can be explained by other self-propelled particle models that allow cells to adjust their propulsive force [125]. In the future we plan to modify our collective migration model to investigate the rate of dynamic cell-cell adhesion in stabilizing both stream formation and aggregation.

Our collective migration model can be extended to include competition between the gradient steepness, $|\nabla C|$, and the local cAMP concentration, C, by modifying Eq. (4.4) and introducing a competition between the noise intensity and the concentration of the cAMP. A simple approach is to impose the following limits: For small local cAMP concentration, the noise (second term in Eq. (4.4)) will have a higher effect in the directionality compared to the guidance from the cAMP gradient (i.e. independent random motion). In contrast, for high local cAMP concentration, the contribution from the noise to local cAMP concentration ratio should be small compared to the gradient steepness to local cAMP concentration ratio. When the collective migration model is extended to include this competition, we can define an organization time scale as a measure of cellular organization. Thus, we can measure the efficiency of stream formation not only with respect to signal relay but also with respect to the efficiency of directional sensing.

We believe that the simplified approach used here for *D. discoideum* can be

extended to more complex cells exhibiting signal relay, such as neutrophils [98,126]. For neutrophils, signal relay is less well understood [98]. However, our numerical simulations can be utilized to distinguish uncorrelated motion from weak signal relay. Using our simulations in conjunction with linear gradient experiments in which cells do not converge naturally to an external signal, we can calculate the effect of signal relay on the mean progression speed, as well as on the development of an inhomogeneous density due to cell-cell attraction, even in the case of signal relay that is not sufficient to lead to discernible clumps or streams. Moreover, our collective migration model can potentially be extended to include the dependence of signal relay on cell density, in order to compare the dynamics to those observed in Ref. [127], which proposes a quorum sensing mechanism that can quantify the persistent random walk of *D. discoideum* at different phases of development as well as at different densities. Another potential use of our collective migration model is to characterize migration in which subpopulations of cells have different signal sensing, and signal relay capabilities. A prominent example of such collective migration is the motion of neural crest cells, a collective process during embryonic development. Recent experiments suggest that mathematical models of the neural crest migration require subpopulations having different chemotactic responses [128].

4.5 Methods

4.5.1 Experiments in linear cAMP gradient

To examine the chemotactic dose response, cell migration was recorded at 12 second intervals for 1 hour in the EZ-TAXIScan chamber (Effector Cell Institute, Tokyo, Japan). In the absence of wild-type cells the device establishes a well-defined, stable cAMP gradient during the course of the experiment [94]. Wild-type *Dictyostelium discoideum* cells (ax3) and ACA null mutant cells (aca-) were prepared as described in Ref. [8]. PDE1- cells were prepared as described in Ref. [25].

4.5.2 Computational implementation

There are two modules in our numerical simulation code, the first module consists of the equations of motion given in Eqs. (4.1)-(4.3) which defines the position and the direction of motion of cells based on the local gradient in the neighborhood of each cell. The second module calculates the diffusive time evolution of cAMP due to the external signal and dynamic local intercellular signals and provides the updated gradient vector field for use in the first module. Simultaneous evaluation of these two modules generates cell tracks. The diffusion equation for the cAMP (Eq. (4.3)) is solved explicitly on a square grid with spacing $\Delta x = \Delta y = 3.3$ μm using a forward time and central space Euler method. In the numerical simulations the time step is $\Delta t = 0.235(\Delta x)^2/D \approx 0.007$ seconds, which is well in the stable range of the numerical algorithm. For implementing the numerical evaluation of

C' the diffusion equation is discretized with $\Delta x' = \Delta x/L_y$ and $\Delta t' = \omega \Delta t$. The Laplace operator can be replaced by the discretized Laplace operator and the Dirac δ function is discretized in one dimension as $\delta(x' = n\Delta x') \to \delta(i,n)/\Delta x'$, where $\delta(i,n)$ is the Kronecker δ function, which is zero except for $i = n$. Thus, the value of the cAMP field at $x' = n\Delta x'$ and $y' = m\Delta x'$, where n and m are integers, is updated according to

$$
\begin{aligned}
C'(x,y,t+\Delta t) &= C'(x,y,t) + \mu' \left(C_D - C_\nu + C_s\right) && (4.13)\\
C_D &= D'\Big(C'(x+\Delta x', y', t') + C(x'-\Delta x', y', t') \\
&+ C'(x', y'+\Delta x', t') + C(x', y'-\Delta x', t') \\
&- 4C'(x', y', t')\Big) && (4.14)\\
C_\nu &= \nu' y'(1-y')(\Delta x')^2 C'(x', y', t') && (4.15)\\
C_s &= s' \sum_i \delta(n, \|x_i'/\Delta x'\|)\delta(m, \|y_i'/\Delta x'\|)\,, && (4.16)
\end{aligned}
$$

with $\mu' := \Delta t'/(\Delta x')^2$. In Eq. (4.13), $\|x_i'/\Delta x'\|$ rounds its argument to the nearest integer. The same $\Delta t'$ is used in evaluating the equations of motion (Eqs. (4.1) and (4.2)). Table 4.1 shows the definitions and values of the parameters used in the numerical simulations.

"This section is reproduced from Ref. [16] under CC BY-NC license"

Chapter 5: Distinguishing patterns of collectively migrating cells

5.1 Overview

So far we have investigated the mechanically- and chemically-guided cell migration independently. Howeve, a cell's natural environment comprises both types of directional cues, and cells often integrate directional signals from various sources. In this chapter, we will investigate the impact of changes in the mechanical cell-cell and cell-surface interactions on collective migration. To identify the differences in the dynamics of the collective motion we introduce topological measures that elucidate cell-cell coordination. We elaborate the model introduced in the previous chapter to include mechanical guidance cues and use this model to demonstrate that the "chemotactic index"–a measure of individual chemotaxis efficiency–is not sufficient to distinguish coordinated motion from the individual cell migration. On the other hand, monitoring the total projected area and the size of the largest connected component in the binarized images of the cells resolves the characteristic patterns formed during the group migration. We then apply these measures to two sets of experimental data representing both genetic and mechanical perturbations. We demonstrate that the topological measures not only distinguish complex patterning structures but also provide insight into how the perturbations affect the migration

efficiency of the cell population.

A current push in experimental and theoretical cell biology is investigating which factors affect the structure and facility of these streams [16, 129]. These transient, local regions of coherence are visible to the eye, but quantification of streaming behavior is an open area of research. The most common measure used is the "chemotactic index" [113,130,131], which is the average cell orientation relative to the direction of a globally applied signal, such as a needle disbursing chemoattractant. Although chemotactic index is a good measure for assessing the efficiency of individual chemotaxis, it ignores local coordination and correlation of alignment between cells. Additionally, this measure requires accurate information about the cell's position over time, which presents experimental challenges.

Stream formation is crucial for *D. discoideum* aggregation, and therefore has strong physical and biological implications for the survival of the organism. Changes in cell-cell communication or defects in the mechano-transductive ability of the cells have been shown to inhibit stream formation [24, 25]. E.g., mutant cells with diminished cell-substrate interactions do not form streams and cluster in smaller aggregates, which results in aberrant sporulation (Fig. 2.1(e)).

Here, we demonstrate the use of topological measures on the binarized images of *D. discoideum* to distinguish variation in group migration. First, we introduce a phenomenological cell migration model to obtain the migratory modes observed in no-flow gradient chambers. Using the synthetic data from the model we show that even with absolute location information, the chemotactic index fails to distinguish between the two modes of cell migration observed in this assay: individual motion

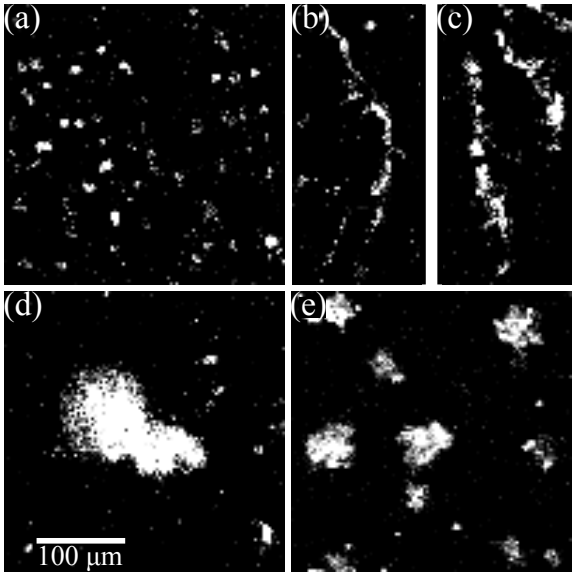

Figure 5.1: (a) Initial state of cells (uniformly distributed). (b-c) Cells moving in streams. (c) Final configuration of wild-type cells is a large aggregate. (d) Mutant cells that cannot stream form smaller aggregates in their final configuration.

and streaming. On the other hand, the onset of collective motion can be precisely determined by using topological metrics, specifically the total projected area and the size of the largest connected component. Then, with live-cell experiments, we explore the robustness of collective behavior by comparing the topological measures among cells with internal defects and cells that are migrating in different environments. We show that our prescribed topological measures not only distinguish group motion in every condition discussed, but also elucidate the modified characteristics of the group-coordination efficiency of cell populations.

The experiments that are presented in this chapter are performed by Chenlu Wang (except the experiments that were published in Ref. [129]). Joshua Parker and myself have equal contributions for both performing numerical simulations and

analyzing both experimental and numerical data.

5.2 Quantifying streaming

To introduce both the problem and our solution for quantifying streaming motion, we here discuss a phenomenological model for collective migration of *D. discoideum* cells. In this model, the dynamics of a single cell are described with three modules, *gradient sensing* (Eqs. (5.1) and (5.2)), *membrane protrusions* (Eqs. (5.3) and (5.4)), and *center-of-mass motion* (Eqs. (5.5) and (5.6)), supplemented by an equation (Eq. (5.7)) for the diffusion, production, and degradation of the chemoattractant. Each cell i is represented as a motile disk with a defined front and back, corresponding to the direction of its motion. The cell responds to the external cAMP concentration field, $C(\mathbf{r},t)$ by aligning its target direction, $\mathbf{g}_i(t)$, to a perceived gradient direction via the following two equations (where $|\mathbf{g}_i(t)|=1$):

$$\dot{\mathbf{g}}_i(t) = \omega_\phi \mathbf{g}_i(t) \times (\mathbf{H}_i(t) \times \mathbf{g}_i(t)) \tag{5.1}$$

and

$$\mathbf{H}_i(t) = \frac{L\nabla C(\mathbf{r}_i(t),t)}{\langle C(\mathbf{r}_i(t),t)\rangle_{\text{local}} + K_D} + \sqrt{\eta_\phi}\boldsymbol{\xi}_{\boldsymbol{\phi}}(t)\,. \tag{5.2}$$

According to Eq. (5.1), $\mathbf{g}_i(t)$ orients itself with the vector $\mathbf{H}_i(t)$ on a relaxation time scale ω_ϕ^{-1}. The deterministic contribution to $\mathbf{H}_i(t)$ (first term on the right hand side of (5.2)) is proportional to the cAMP gradient if C is low and saturates to $l(\nabla C/C)$ when C is large ($C \gg K_D$), consistent with experimental observations [113] (L is the characteristic size of the migration chamber). According to Eq. (5.2), $\mathbf{H}_i(t)$ has a stochastic component modeled by two-dimensional white noise of amplitude

η_ϕ ($\langle \xi_\phi^j \rangle = 0$, $\langle \xi_\phi^j(t) \xi_\phi^{j'}(t') \rangle = \delta_{jj'}\delta(t-t')$, where $j = x, y$ indicates the directional component). This approximation models the stochastic nature of the binding and unbinding of cAMP molecules to receptors [95, 113, 115, 132].

The "membrane protrusion" module models the cell's protrusive response $\mathbf{n}_i(t)$ to its target direction of motion, and with the net direction of new protrusions corresponding to the two equations

$$\dot{\mathbf{n}}_i = \omega_\theta \mathbf{n}_i \times (\mathbf{G}_i \times \mathbf{n}_i) \tag{5.3}$$

and

$$\mathbf{G}_i = \mathbf{g}_i + \sqrt{\eta_\theta}\boldsymbol{\xi}_{\boldsymbol{\theta}}(t)\,. \tag{5.4}$$

That is, the unit vector $\mathbf{n}_i(t)$ responds to a noise-corrupted goal direction $\mathbf{G}_i(t)$ (with noise amplitude η_θ) on a time scale ω_θ^{-1}.

Finally, the center-of-mass motion of cell i, located at point $\mathbf{r}_i$ and moving with velocity $\mathbf{v}_i$, is modeled by the equations,

$$\dot{\mathbf{v}}_i(t) = -\beta \mathbf{v}_i(t) + \kappa v_0 \mathbf{n}_i(t) + \sum_{j \neq i} \mathbf{f}_{ij} \tag{5.5}$$

and

$$\mathbf{f}_{ij} = k\left(1 - \frac{d_{ij}}{2r_0}\right)\frac{\mathbf{r}_i - \mathbf{r}_j}{d_{ij}^3}\Theta(2r_0 - d_{ij})\,. \tag{5.6}$$

Here, $\mathbf{f}_{ij}$ is a "force" with strength k (Θ is the unit step function) that prevents the cells (assumed to be of size r_0) from occupying the same space. In the absence of mechanical interactions (i.e., $k = 0$), Eq. (5.5) can be integrated to yield $\mathbf{v}_i(t) = \kappa v_0 \int_{-\infty}^{t} e^{-\beta(t-t')}\mathbf{n}_i(t')dt'$. This approximation identifies the center-of-mass motion as a "sum over protrusions" [11] with a characteristic time scale β^{-1}, where

κ is a time-independent parameter selected so that the speed $|\mathbf{v}_i|$ suitably averaged over cells is v_0 (see supplementary information). Because the aim of this chapter is to demonstrate stream quantification, we chose model parameters with values that exaggerate the streaming behavior of this extension of the collective migration model.

We simulate Eqs. (5.1)-(5.6) in a square chamber with side $L = 0.33$ mm, cell density ρ, and periodic boundary conditions for the cell motion (thus, if a cell leaves through one of the four boundaries, it is reintroduced at the opposite boundary). The cells are initially distributed to be not in contact but otherwise random, and the simulation is allowed to run sufficiently long to reach steady state. The dynamics of the chemoattractant inside the chamber are governed by the diffusion equation,

$$\partial_t C \;=\; D\nabla^2 C - \nu(y)C + s\sum_j \delta(\mathbf{r} - \mathbf{r}_j)\,. \tag{5.7}$$

The first term on the right hand side of Eq. (5.7) represents diffusive spreading of the chemoattractant with diffusivity D. The second term represents global degradation of the cAMP field by phosphodiesterases secreted by the cells. The third term represents a constant secretion of cAMP from each cell with rate s [24]. We choose the form of $\nu(y)$ and the boundary conditions on $C(x, y, t)$ to mimic behavior experiments performed in no-flow gradient chambers [16]. The boundary conditions are $C(x, 0, t) = 0$, $C(x, L, t) = C_0$, $C(x + L, y, t) = C(x, y, t)$, whereas $\nu(y) = 4\nu_0 y/L(1 - y/L)$ where ν_0 is a coefficient reflecting the rate of degradation.

Figs. 5.2(a-c) show model simulations of the three steady state phases of this model (individual motion, streaming, and aggregation) for a representative set of

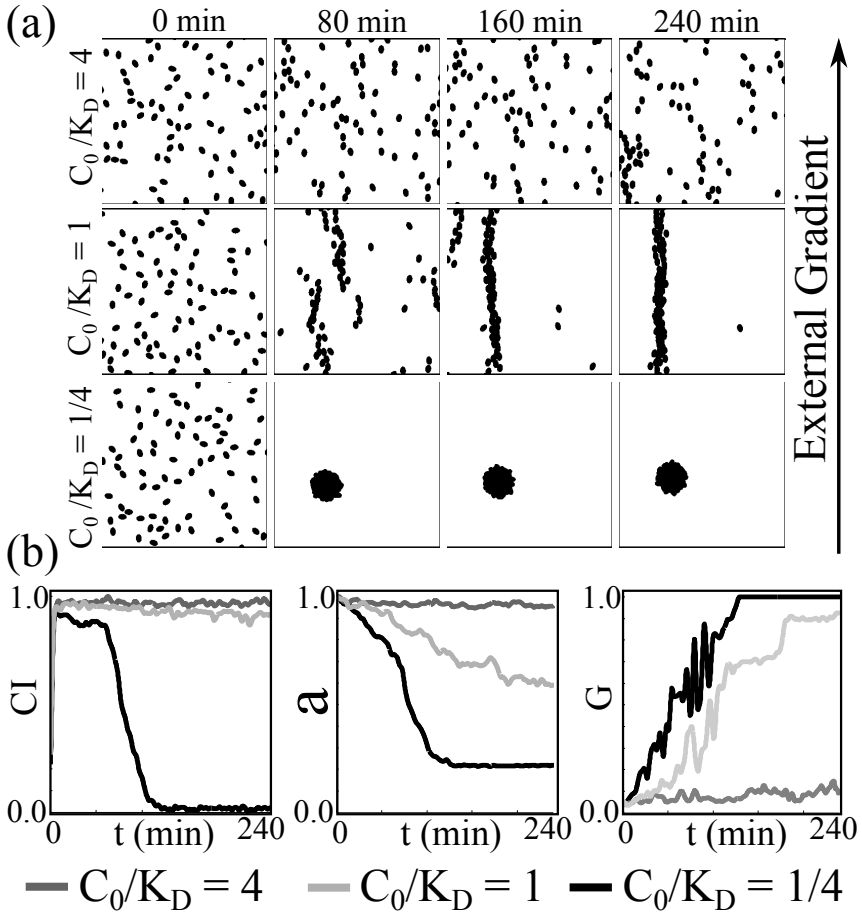

Figure 5.2: (a-c) Snapshots of the simulations demonstrating the three steady state dynamic modes: individual motion, streaming, and aggregates ($\rho = 750$ mm^{-2}) (d-e) The chemotactic index fails to distinguish the individual motion from streaming while the two topological measures a and G correctly distinguish all migratory modes

parameters and three values of reservoir concentration of the chemoattractant, C_0. For high C_0, the production of cAMP by cells has minimal contribution to the total cAMP gradient, therefore cells move in the y direction (Fig. 5.2a). For moderate C_0, the cell's secretion of cAMP results in a large stream (Fig. 5.2b). For low C_0, streams become unstable and fold into aggregates (Fig. 5.2c).

The chemotactic index for the these three scenarios is shown in Fig. 5.2d. Although the cells are coordinating their migration upwards by forming streams, their overall orientation is almost indistinguishable from that of individual motion. Therefore, the chemotactic index cannot capture the coordination among cells because it is a measure for the efficiency of individual chemotactic behavior. To elucidate the cell-cell coordination it is necessary to measure high-order spatial correlations among migrating cells.

The three migratory modes of this model can be quantified with two topological measures. The first measure is the first Minkwoski number of the image, $a(t)$, which is defined as the total binarized area of the cell images, normalized by the area from the first frame [1]. The second measure is the fraction of the total area taken up by the largest connected component in the image, which is defined as $G(t)$. This measure is borrowed from studies of percolation in networks [134, 135], where moderate values of $G(t)$ suggest the presence of a "giant component", i.e. a dominant structure representing the majority of interactions. Both measures were implemented with custom scripts in MATLAB.

[1] This measure (along with the other two Minkowski numbers) have found recent application in distinguishing sets of protein point patterns, see Ref. [133]

Figs. 5.2(e-f) show these two measures over time for the three modes of the cell migration model. For non-interacting cells the total projected area remains roughly constant and there is no giant component ($a \approx 1$, $G(t) \approx 0$). For streaming motion, the size of the largest component progressively increases with time and eventually saturates to 1. The onset of collective motion can be identified by the size of the giant component. The total projected area is starkly diminished when cells form an aggregate, which is the only and largest component in the entire system ($A << 1$, $G(t) = 1$). Therefore, the combination of the topological measures can identify the different migratory modes that are observed in the model results.

5.3 The individual's role during coordinated motion

Mutant cells that lack key regulators of cell migration (e.g., chemoattractant degradation [25], signal relay [8], and cell-substrate adhesion [129]) exhibit aberrant streaming and collective migration. Fig. 5.3a shows time-lapse images of Ax3/WT, Ax2/talA-, and Ax3/aca- cells migrating towards a needle, notated with the white asterisks. Wild-type cells form streams that enhance the reach of the global signal emanating from the needle and aggregate at the tip of the needle. The talA- mutants lack the protein Talin, which modulates the interaction between the actin skeleton and the plasma membrane [136]. These mutant cells cannot move in streams and therefore only generate small clumps. These clumps are distributed around the needle and their size increase over time. However, clumps cannot merge into a large aggregate similar to the one that the wild-type cells form. The mutant aca- cells

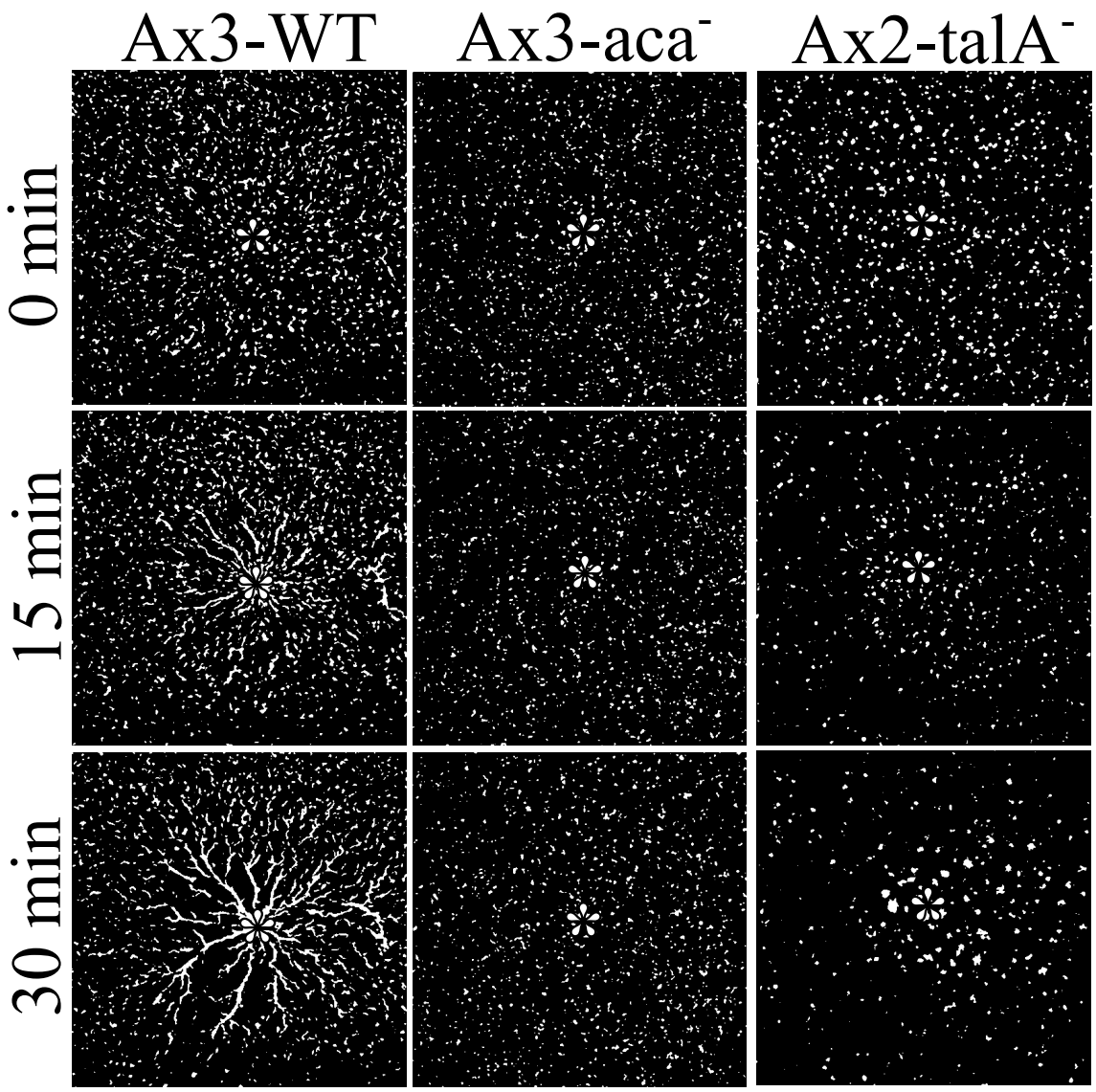

Figure 5.3: Snapshots of cell migration assays with a chemoattractant needle present (the white asterisk denotes needle location). The two mutations, one to adhesive ability and one to signal relay, both diminish the migratory efficiency of the cells

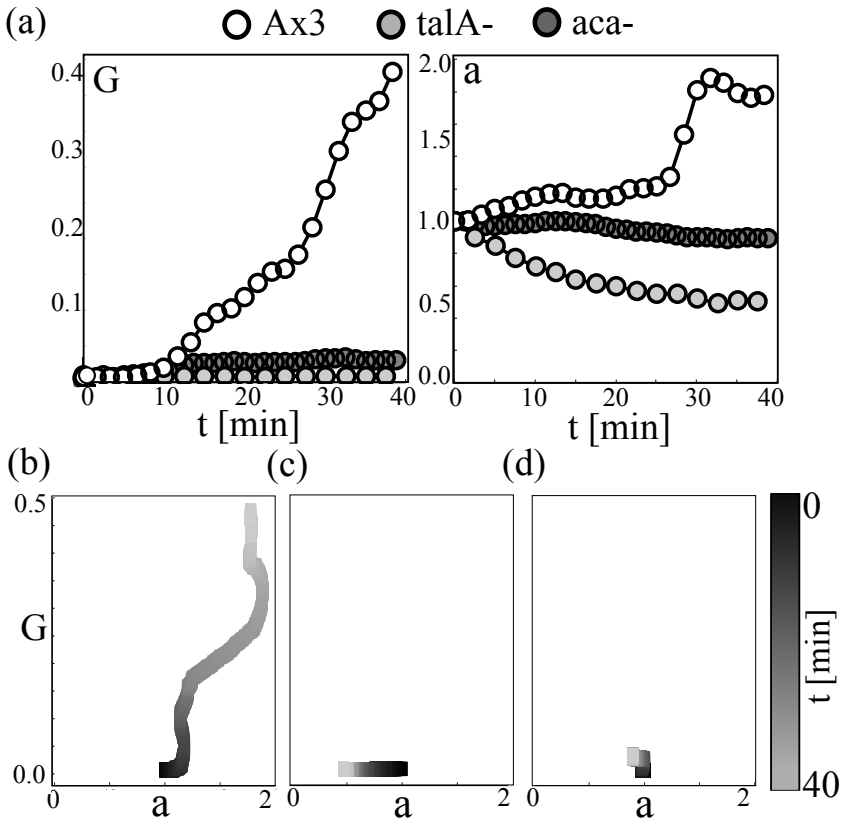

Figure 5.4: (a) Our topological measures for the needle experiments. The combination of the two numbers successfully delineate each experiment (b) Parameter trajectories for the three needle experiments, elucidating key biological processes such as signal propagation and recruitment

do not have the enzyme Adenaline Cyclase A, which is the essential component of chemical signal relay [24]. In contrast with the talA- mutants, the aca- mutants have no significant migratory deficiencies based on the comparison of their individual chemotaxis efficiency with wild-type cells [8]. However, Aca- cells do not form either local clumps or streams, but merely migrate in the direction of the externally imposed gradient. The lack of signal relay reduces the recruitment of many cells to the needle, because the reach of the chemoattractant signal is spatially limited.

All of the characteristics of the cell-cell coordination of genetically defected cells were quantified with the two topological measures $a(t)$ and $G(t)$. The projected area is normalized by the first frame of the movie when the cells are dispersed. Therefore, the apparent sharp increase in a suggests both strong response by the cells in spreading onto the surface (thus being more reflective) and in the recruitment of other cells that were initially outside the image boundary, and the overall increase in G corresponds to an emergence of a dominant connected component in the image. In contrast, both aca- and talA- mutant cells exhibit negligible recruitment. Both of the genetic mutations result in a loss of a dominant structure. This inability for long-range communication suggests that the overall migratory efficiency towards the needle is diminished. However, cell-cell coordination of the two mutant cell types was distinguished by a. For talA- mutants, the steady decrease in this measure shows the formation of small clumps that never aggregate into a dominant component. These characteristics are better separated visually on a parametric plot of the two measures (time in shades of gray), seen in Figs. 5.4(c-e). All three experiments begin at the same point ($a(0) = 1$, $G(0) \approx 0$), but their progression from this point is visually distinguishable.

5.4 Effect of environmental perturbations on cell-cell coordination

Recently, the migratory dynamics of *D. discoideum* cells were investigated, when cells were plated on surfaces with different chemical properties [129]. Fig. 5.5 shows time lapse images from self-aggregation experiments on normal glass and

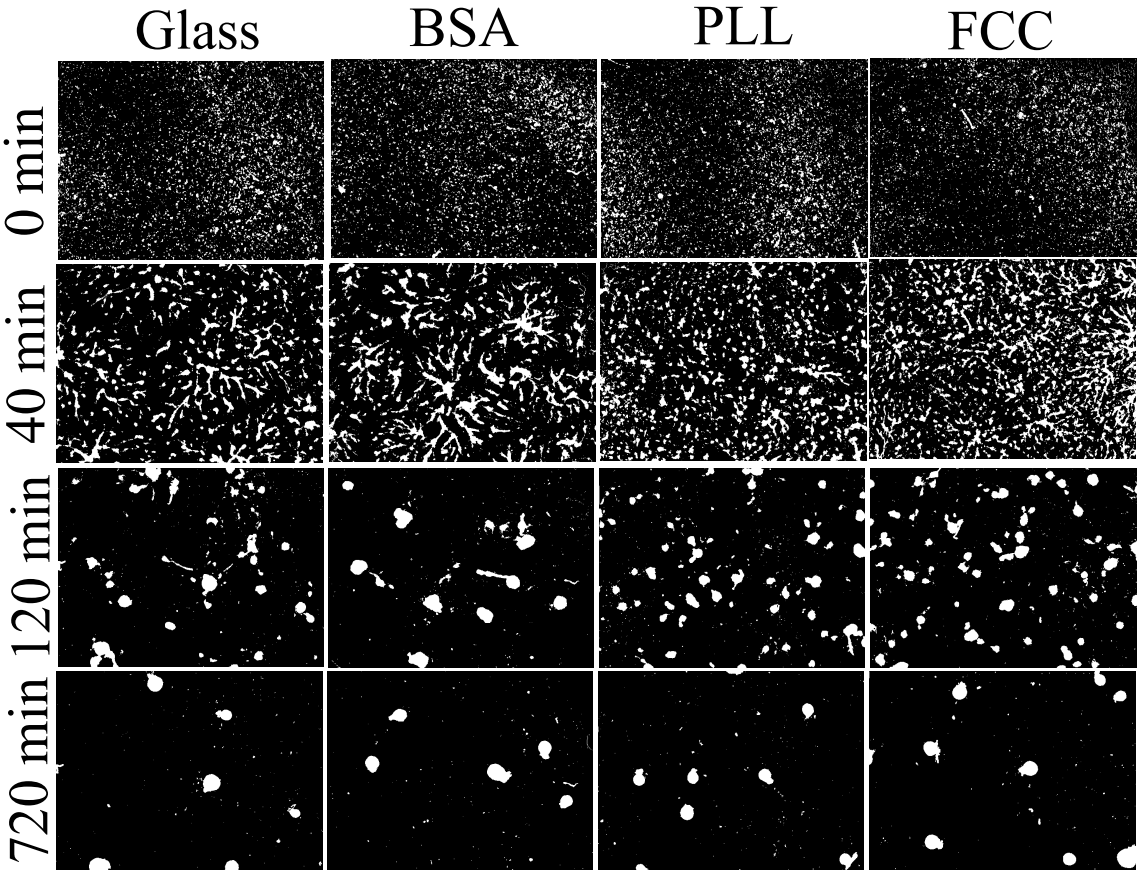

Figure 5.5: Snapshots of self-aggregation cell migration assays involving cells plated on surfaces with different adhesive capacities. Both glass and BSA form large streams quickly and fewer aggregates while PLL and FCC seem to have diminished streaming capacity and form smaller aggregates, suggesting surface adhesion plays a notable role in the migratory efficiency of the cells. The figure is generated from data published in Ref. [129].

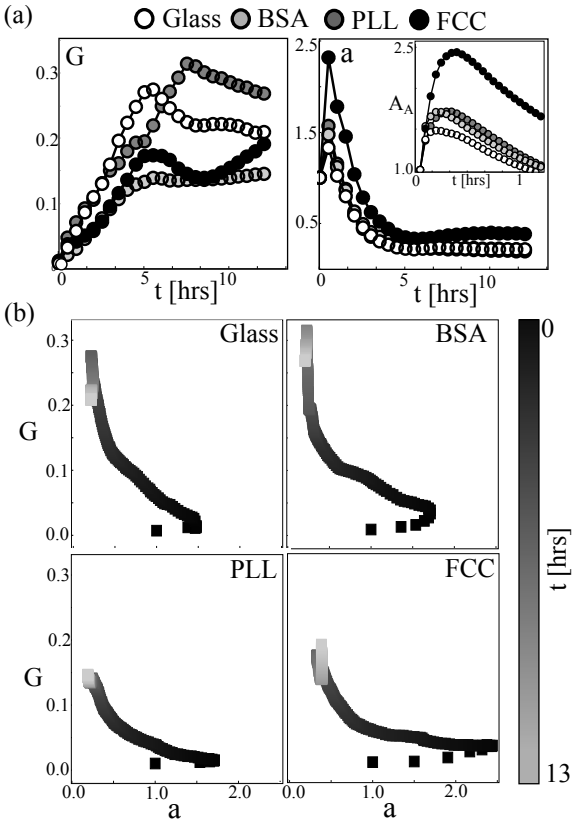

Figure 5.6: (a) Our topological measures for the surface experiments. The combination of the two numbers distinguish each experiment (b) Parameter trajectories for the four surface experiments. It is apparent that the strong adhesive capacity retards streaming and therefore healthy aggregation

glass coated with three different chemicals: bovine syrum albumin (BSA), poly-L-lysine (PLL), and perfluorinated carbon chains (FCC). Ref. [129] concluded that although there were significant differences in adhesive capacity of the surfaces, there were no significant migratory differences on the individual cell level. Nevertheless, surfaces with stronger adhesive properties (PLL and FCC) seemed to slow aggregation. Experimentally, measuring the chemotactic index is challenging, due to the lack of a defining the direction of the chemoattractant gradient and segmenting cells in contact.

Fig. 5.6(a-b) shows the two topological measures for these experimental conditions, both over time and as a parametric plot. These combined measures distinguish the different experiments and quantify the cell-cell coordination under different external conditions. The projected area, $a(t)$ is always greater for cells that are moving on FCC than on the other surface coatings. This observation agrees with the shaken-assay results reported in Ref. [129] (cells spread and adhered to FCC the most strongly). The inset of Fig. 5.6 shows that the cell-cell coordination rate is faster for cells moving on surfaces with lower adhesion. The progression of $G(t)$ shows that both PLL and FCC have shallower initial slopes and its peak value is much lower than cells migrating on non-coated surface or BSA coating, suggesting the lack of large streams forming bridges to local aggregate centers. Although individual cell characteristics are similar, the large-scale organization of cells depends on a variety of internal and external factors.

5.5 Discussion

Quantifying complex pattern formations seen in biological systems is crucial for understanding biological phenomena. These patterns are often not spurious in nature, but have biological implications. *D. discoideum*, for example, forms large streams, which serve as roads that efficiently recruit more cells from long distances. This recruitment increases the local population of cells and is subsequently followed by proper sporulation and organismic survival. In this work, we have introduced a robust pair of topological measures for quantifying what effect experimental variations have on streaming patterns.

The combination of chemical (i.e., Eq. (5.1)) and mechanical (i.e., Eq. (5.3)) directional sensing modules in conjunction with the suggested phase space of topological measures provide a framework for the modeling and analysis of neutrophil chemotaxis, which requires both chemical and mechanical inputs [83]. Neutrophils respond to multiple chemoattractants [137]. Although neutrophils relay some of the perceived chemoattractants, unlike *D. discoideum* their collective motion does not result in visually detectable modes of migration [98]. To reach an infectious zone, neutrophils are exposed to multiple chemoattractant gradients, yet they succeed integrating these interfering/conflicting signals efficiently. Recent modeling has attempted to investigate signal transduction through a competition between multiple chemoattractants in the absence of relay and mechanotransduction [138]. Our model can be generalized to include multiple chemical inputs (e.g., a linear composition of many equations in the form of Eq. (5.1)). Also, adhesive/repulsive cell-substrate

interactions can be included in Eq. (5.6). Using an effective interaction distance for nearby neutrophils, we can extend the cell-cell cooperation analysis to investigate the lengthscales associated with the neutrophil collective migration.

The phase space defined by the topological measures enables comparison of collective migration for a wide range of organisms. Because the chemotactic index determines the efficiency of individuals, it is not a suitable measure for comparing cells that have different natural environments. However, the giant component size and the relative area occupied by the cells are properly normalized measures that do not depend on information on individual cell migration. We believe that comparison trajectories and steady states on the (a,G) phase space will enable classifying the collective motion phenotype in systems ranging from swarming cells to flocking birds.

Chapter 6: Outlook

6.1 Conclusion

In this dissertation–with a combination of experiments, quantitative analysis, and modeling–I have discussed mechanisms for the guidance of cell migration from subcellular to multicellular scales. Specifically, my contributions are: (*i*) Conducting some of the experiments presented in Chapter 2, (*ii*) developing the preferential-actin-polymerization model presented in Chapter 2 by modifying the actin-polymerization model introduced in Ref. [66], (*iii*) performing numerical simulations of the preferential-actin-polymerization model presented in Chapter 2, (*iv*) developing analysis tools and analyzing both the experimental and numerical data presented in Chapter 2, (*v*) developing analysis tools and analyzing experimental data presented in Chapter 3, (*vi*) developing the cellular-oscillation model presented in Chapter 3, (*vii*) analyzing both experimental and numerical data presented in Chapter 4, (*viii*) developing the collective-migration model presented in Chapter 4, (*ix*) implementing model equations and performing numerical simulations of the collective-migration model presented in Chapter 4, (*x*) developing the extension of the collective-migration model presented in Chapter 5, (*xi*) developing tools for the analysis of the experimental and numerical data presented in Chapter 5, and (*xii*)

conducting the experiments that are presented in Chapter 6.

In Chapter 2 and Chapter 3, I have shown how mechanical guidance cues may result in directed migration of individual cells. By analyzing actin wave propagation on nanotopography I have suggested subcellular mechanisms for mechanically-guided cell migration. In summary, these mechanisms are:

— Actin polymerization localizes around the tops of the nanoridges, suggesting that the polymerization of actin is promoted preferentially through the positive curvature imposed by the nanoridges.

— The spacing of the nanoridges affects the polymerization rate of actin, which is reflected in the measured speed of propagation of actin waves. In particular, waves induced by the closely-spaced nanoridges propagate more slowly than waves induced by widely-spaced nanoridges. The slower wave propagation speed is potentially due to the competition for finite resources such as ATP or free actin monomers.

— If waves align perpendicularly with respect to the nanoridge orientation and traverse multiple ridges, they dissipate or get split by nanoridges and propagate parallel to the orientation of nanoridges. As a result, the average wave orientation becomes aligned with the nanoridge orientation.

— The preferential polymerization of actin on nanoridges can be explained by a difference in nucleation rates of actin on and off the nanoridges. Simulations with increased nucleation of actin on nanoridges compared to flat surfaces yield

anisotropic wave propagation parallel to the nanoridges that is comparable to experimentally observed waves in size and localization.

At a larger scale, nanotopography guides cell migration. In Chapter 3, we showed how guidance of cells can be quantified by a contact guidance efficiency parameter and introduced a phenomenological model that connects larger-scale directed migration to cellular oscillations modulated by the nanotopography. At larger scale the interaction between the nanotopography and the cell can be modeled as a stochastic resonance. This model indicates that the timescale of internal dynamics–which is yet to be associated with actin dynamics–determines the characteristic lengthscale of the topography sensed by the cell. Hence, sensing is dynamic. We showed that if a protrusion encounters new ridges approximately every 10 seconds, its extension along the nanoridges is maximized. The guidance of protrusions via the mechanical forces exerted on polymerizing actin is more direct than the preferential motion of cells during chemotaxis. The connection between the guided oscillations and observed persistent waves is an open question that needs to be explored in future work.

The protrusion is roughly a factor of two faster than the chemically-induced oscillations of actin recruitment to the plasma membrane. Figure 6.1 shows a suggested model for chemically-mediated actin polymerization. The main pathway that is suggested in this example is that of PI3K, which generates an asymmetric distribution of the chemicals PIP2 and PIP3. The slower timescale of the chemically-induced directed migration is justified by the additional biochemical reactions embedded in

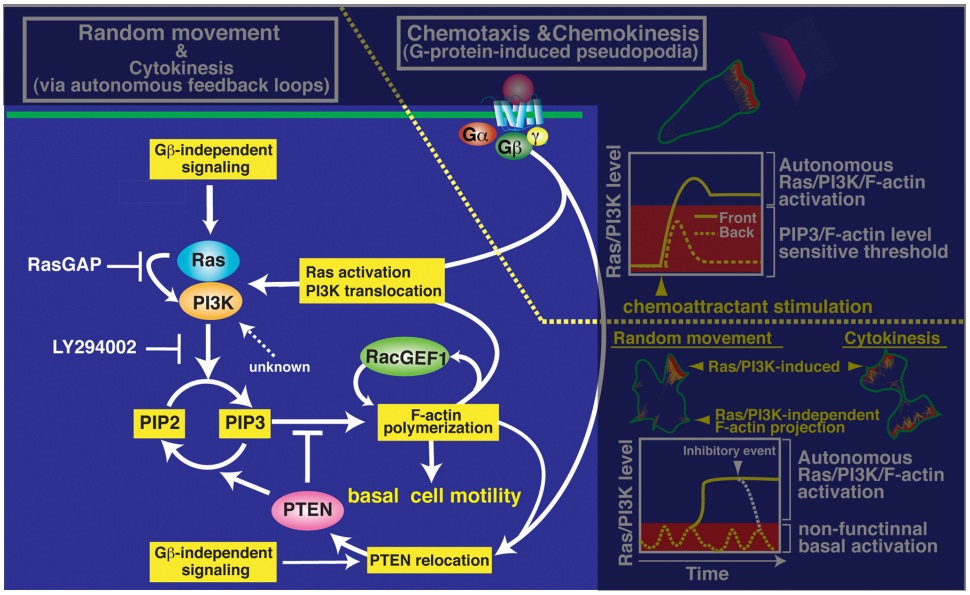

Figure 6.1: The suggested model for the chemically-mediated actin polymerization and chemotaxis. Domains of G-proteins result in an asymmetry in PIP2/3 concentrations, which regulate actin polymerization. Figure reproduced from Ref. [69]. (Sasaki et al., 2007. Originally published in Journal of Cell Biology. doi:10.1083/jcb.200611138)

multiple signal transduction pathways [139].

In Chapter 3, we also introduced another example of mechanically-induced directed migration: the persistent migration of cells confined in microchannels. Analysis revealed that the persistence time of the cell's motion is increased due to ordering of left/right protrusions. Comparing auto-covariance of these protrusions to the cross-covariance between protrusions, we observed that the ordered protrusions were interdependent. In particular, protrusions are not autocatalyzed, but rather are promoted by the extinction of the opposite protrusion. Furthermore, we analyzed the underlying actin polymerization dynamics inside these protrusions and found that the unidirectional migration of the cells is associated with spatially-stationary

patches of actin polymerization that have an average lifetime of 10 seconds. Comparing this result to the resonant timescale obtained in the previous section, we concluded that physical forces not only can mediate actin polymerization but their impact is also much more direct compared to that of signal-transduction-mediated directed migration.

In Chapter 4, we looked at the effect of the directed single cell motion on the migration of groups of cells. Based on our previous findings we developed a coarse-grained model for the persistent migration of individual cells to investigate the directed migration of cells that emerges from intercellular communication. We measured the cell-cell communication by investigating cell motion in a linear external chemoattractant gradient. We modeled this type of directed migration to extract the amplitude of the noise in cell's perception of the chemoattractant gradients. We found that the timescale associated with this noise corresponds to the resonant timescale of chemically-induced directed migration. We then incorporated cell-cell communication processes in our model and found that the collective migration of cells depends on the competition between the rates of signal production and signal degradation. By quantifying the efficacy of signal relay we characterized the competition between multiple "streams" that lead to formation of large aggregates.

From the results of the collective-migration model, we found that when the dispersion length of the chemoattractant is large, cell groups aggregate quickly and become entrapped in small local aggregates. For strong external gradients, cells are drawn to the global attractor, which could either be a needle that steadily injects chemoattractant to the cell medium or a large aggregate of cells. The efficacy

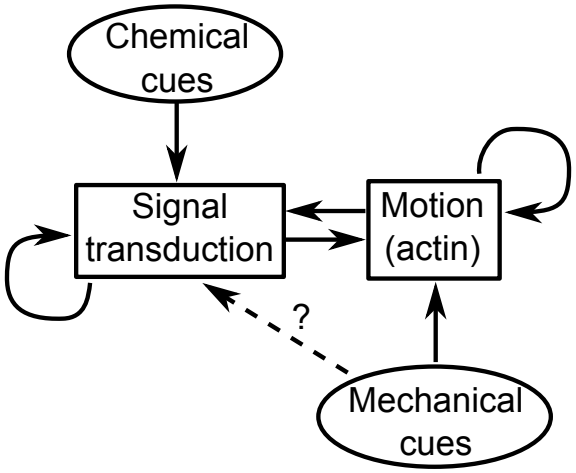

Figure 6.2: Graphical summary of the chemically- and mechanically-induced directed migration. We have shown that mechanical cues can provide a feedforward to actin polymerization dynamics. The connection between the chemical signal transduction and mechanical guidance cues at individual and multicellular levels remains as an open question.

of cell-cell communication is maximized when cells are able to form and maintain streams. This mode of migration emerged when the cell-cell communication strength is comparable to the strength of the externally imposed chemoattractant gradient.

In Chapter 5, we extended the model introduced in Chapter 4 to include mechanical modulation of actin polymerization. We analyzed simulations of collective motion with novel topological measures to assess the cooperation between cells during their large-scale organization. Using these measures we compared the ensemble communication efficiency of mechanically-defective cells to chemically-defective cells and concluded that mechanical defects have less impact on the ensemble's long-distance communication ability. We also showed that the steady state of collective cellular migration is robust under the change of the mechanical properties of the environment. Despite comparable steady-state behavior, the transient aggregation

is heavily dependent on the interaction strength between the cell membrane and the substrate. Cells that are slowed down by high adhesion to the substrate demonstrated better communication compared to cells that are more motile because they are on surfaces with less adhesion. This quantification was enabled by reducing the collective dynamics information of the ensemble to a two-dimensional phase space defined by the topological measures (Figs. 5.4 and 5.6).

6.2 Future directions

Our results raise two significant questions that need to be addressed. We have concluded that physical forces modulate actin polymerization. In Fig. 6.2 a proposed interaction diagram shows the connection between chemical sensing and actin polymerization. As shown in Fig. 6.1, some of these connections are very well identified. An interesting question is how much of the guidance of actin polymerization via the nanotopography propagates to the signal transduction through feedbacks from actin polymerization? Do physical forces also modulate reactions that yield waves of PIP2 phosphorylation?

In Fig. 6.3 preliminary results of PIP3 waves propagating on 1.5-μm-spaced nanoridges are shown. Observations of the interaction between PIP3 waves and nanotopography suggest hints for addressing the previously posed questions. PIP3 waves are also guided by the nanotopography, however their behavior is different from the preferential polymerization waves of actin. The initial elongation of PIP3 waves parallel to the orientation of nanoridges is followed by a perpendicular split.

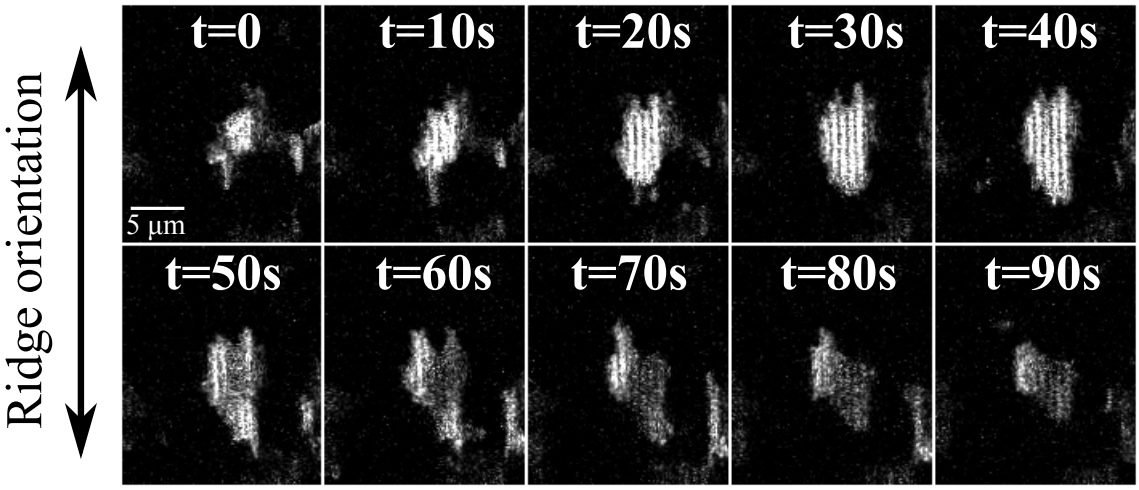

Figure 6.3: A representative example of PIP3 waves propagating on 1.5-μm-spaced nanoridges. Compared to the fast dynamics of actin polymerization waves on nanoridges, PIP3 waves are quasi-stationary. The waves exhibit both parallel and perpendicular propagation with respect to the orientation of the nanoridges.

Remarkably, the timescale that defines the duration of a potentially nanoridge-induced PIP3 wave is long compared to that of actin polymerization dynamics. My ongoing research aims at quantifying and understanding the effect of nanoridges on upstream chemical sensing pathways.

The other question is, under what circumstances can mechanically-induced directed migration dominate chemically-induced directed migration and vice versa? The competition between the different types of directed migration can be examined by directionally-independent chemoattractant and contact guidance inputs. For example, by measuring the contact guidance index in the presence of a linear cAMP gradient the mechanical guidance can be compared with chemical guidance in a controlled way. Having answers to these questions will provide experimental connec-

tions to understanding how cells navigate in their natural environment individually or collectively by integrating signals from multiple sources.

Appendix A: Supplementary information for "Actin wave guidance via periodic nanotopography"

A.1 Tracking of actin polymerization waves

A.1.1 Obtaining flux vectors

To track actin waves, we developed a tracking algorithm based on the apparent flow of actin. Our algorithm was implemented as custom-written Matlab software. This algorithm, which is similar to an optical flow algorithm, results in flux vectors, $\mathbf{K}_i$, that correspond to the apparent flow of actin between two time frames i and $i+1$. We began by measuring at each pixel the flux of fluorescence intensity from frame to frame. For each time frame, we consider two successive images from the fluorescence channel, A_i and A_{i+1}. First, we smooth A_i using a Gaussian kernel with a standard deviation of σ_s pixels. Next, we calculate the gradient of the smoothed image and normalize the gradient vectors by their magnitude. If the dynamics of the measured entity (i.e., actin polymerization) were only diffusive, we could obtain flux vectors using Fick's law, $\mathbf{K}_i = -D\nabla A_i$, where D is the diffusivity of the entity. However, actin polymerization is not purely diffusive. We thus obtain flux vectors by masking the gradient of the first image with the difference image $(A_{i+1} - A_i)$. This difference

image is further smoothed with a Gaussian kernel of standard deviation σ_t and thresholded at ϵ of the maximum allowed image intensity. The smoothing associated with σ_t reduces image noise, whereas the smoothing associated with σ_s spreads information across space. A discrete numerical implementation of the following series of operations yield the vector field, $\mathbf{K}_i$, that represents the flux vectors at frame, i:

$$\begin{aligned}
\Delta A_i &= A_{i+1} - A_i && \text{(A.1)}\\
\Delta A_i &\leftarrow \Delta A_i \otimes G(\sigma_t) && \text{(A.2)}\\
\Delta A_i &\leftarrow (\Delta A_i > \epsilon I) && \text{(A.3)}\\
A_i &\leftarrow A_i \otimes G(\sigma_s) && \text{(A.4)}\\
\mathbf{K}_i &= -\frac{\nabla A_i}{|\nabla A_i|} \times \Delta A_i \,, && \text{(A.5)}
\end{aligned}$$

where $G(\sigma) := e^{\frac{x^2+y^2}{2\sigma^2}}/(2\pi\sigma^2)$ is a two-dimensional Gaussian function with standard deviation σ and I is the maximum allowed intensity in the entire image stack. $A \otimes G(\sigma)$ represents a convolution of the image A with the Gaussian kernel:

$$\frac{1}{2\pi\sigma^2}\int_{-\infty}^{\infty} dx'dy' A(x,y) e^{\frac{(x-x')^2}{\sigma^2}+\frac{(y-y')^2}{\sigma^2}} \,. \qquad \text{(A.6)}$$

$A \times B$ (or $\frac{A}{B}$) indicate element-by-element multiplication (or division), which is obtained by multiplying (or dividing) each pixel value in the first image, $A(x,y)$, with each pixel value in the second image $B(x,y)$. ∇ represents the gradient operator. $|\nabla A| := |\nabla A(x,y)|$ represents the magnitude of the gradient vector at each pixel, (x,y).

A.1.2 Clustering flux vectors

The flux vectors are clustered according to their orientation with respect to their nearest neighbors in both space and time. Each pixel, (x, y), in an image A_i has six nearest neighbors. Four of these neighbors are spatial neighbors in the same image and have coordinates $(x \pm 1, y)$ and $(x, y \pm 1)$. The other two neighbors are temporal neighbors and have coordinates (x, y) in the images A_{i-1} and A_{i+1}. We link a pixel to its neighbor if the dot product of the normalized flux vectors defined at these pixels is greater than 0.1. Next, we define a graph in which the nodes are pixels and the edges are links and represent that graph as a sparse adjacency matrix. Using Tarjan's algorithm [74], we find the connected components of this graph and define each connected component as a cluster of flux vectors.

A.1.3 Refining clusters

With our imaging conditions actin waves are sampled more frequently in space than they are in time. The clustering procedure described in the previous paragraph is thus performed twice. To link flux vectors in time, we first cluster flux vectors obtained from excessively smoothed images. In this first clustering, we used $\sigma_s = 24$ pixels, $\sigma_t = 4$ pixels, and $\epsilon = 6\%$ of the maximum allowed image intensity. We further morphologically erode the temporal links between each pair of subsequent frames using a disk of radius 4 pixels as a structuring element. To link flux vectors in space, we again cluster the vectors using $\sigma_s = 3$ pixels, $\sigma_t = 2$ pixels, and $\epsilon = 12\%$ of the maximum allowed image intensity. Next, the eroded temporal links from the

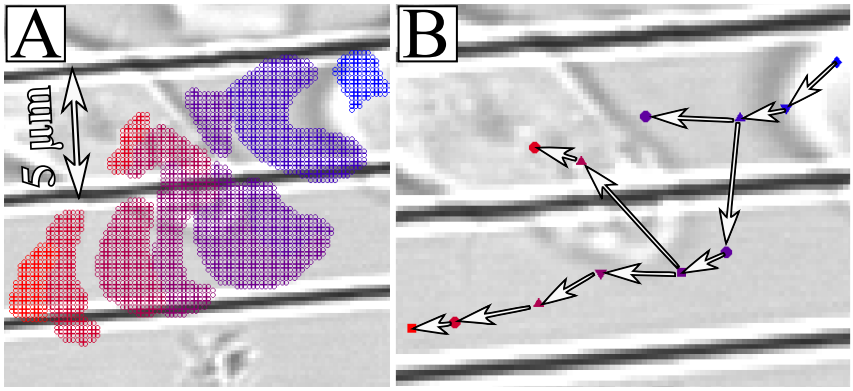

Figure A.1: An incident actin wave is split by a nanoridge (result from experiments). The reflected portion of the wave diminishes. The refracted portion partially engulfs the nanoridge and is subsequently split by the nanoridge once again. One wave continues to propagate parallel to the nanoridge whereas the other wave is diminished. (A) and (B) show the waves and the centroid motion of the waves, respectively.

first clustering are combined with the spatial links from the second clustering to form a single graph. We define each connected component of this graph as a refined cluster of flux vectors.

A.2 Actin wave splitting

In our algorithm, if a parent actin wave splits into multiple spatially disconnected children waves, then both the parent and the children are clustered together as one wave. Splitting events often occur when waves collide with nanoridges. We calculate the speed of the wave from the positions of the waves centroid positions, and so we must account for the wave splitting. For events that split from one wave in two fragments, we calculate the speed of these fragments as the displacement of the fragment centroid from the centroid of the previous cluster. These speeds

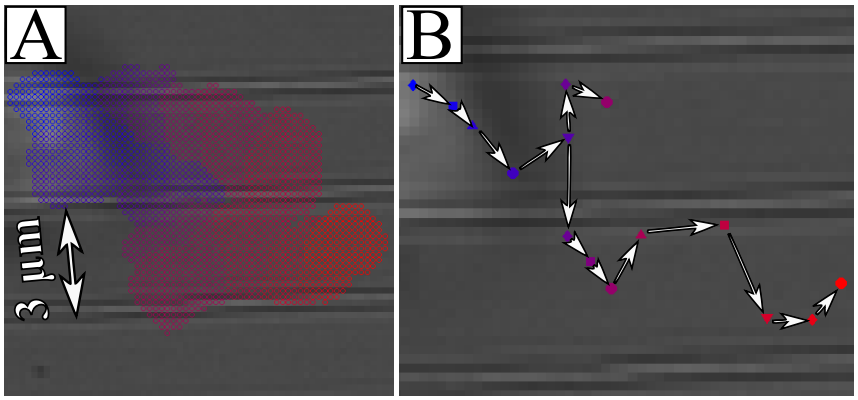

Figure A.2: Initially, an experimentally observed wave is confined between two nanoridges that are separated by 3 μm and propagates parallel to the nanoridges. After contacting with a nanoridge, the wave splits into two waves. The surviving wave is again confined in the groove. (A) and (B) show the waves and the centroid motion of the waves, respectively.

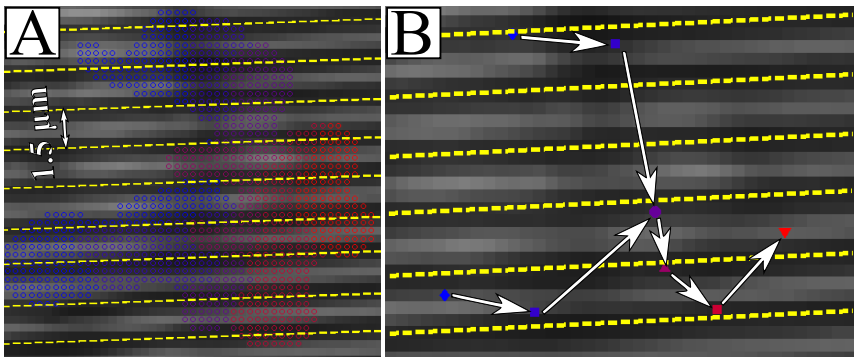

Figure A.3: Two experimentally observed actin waves merge and continue propagating as a single wave. The waves and the centroid motion are show in (A) and (B) respectively. Yellow dashed lines correspond to the location of the nanoridges that are separated by 1.5 μm.

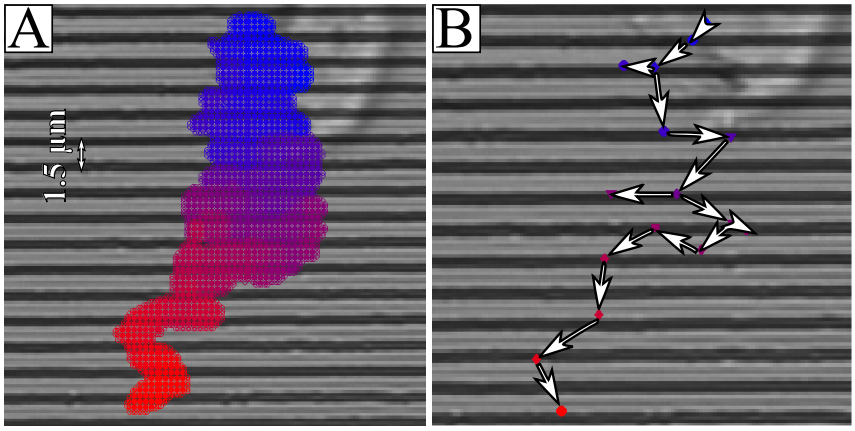

Figure A.4: (A) An experimentally observed actin wave dissipates as it is propagating perpendicular to the 1.5 μm spaced nanoridges. (B) The centroid motion of the actin waves shown in (A). There are two splitting events.

are included in the speed distributions. We discarded the higher order splitting events, due to the uncertainty in the wave centroid (all fragments have their own centroid and the mean position of these centroids does not represent a wave). In Figs. A.1-A.4 we show some representative examples of the splitting events.

A.3 Positions of the nanoridges

To find the positions of the nanoridges, we use slightly different algorithms to obtain the centers of the nanoridges for large spacings (i.e., 3 and 5 μm) and for small spacings (i.e., 0.8 and 1.5 μm). For large spacings, we first convolve the bright field images with a Laplacian of a Gaussian filter, in which the Gaussian has a standard deviation of 0.2 pixels. For large ridge spacings (i.e., 3 and 5 μm), we then use a Hough transform to obtain the coordinates of the lines (i.e., nanoridges)

in the images. For small ridge spacings (i.e., 0.8 and 1.5 μm), we use a Radon transform instead of a Hough transform. For each image, the applied transform yields the angle between the lines and the x axis, ϕ (obtained with a resolution of 0.01 degrees). We determine the orientation of the nanoridges as the median of the ϕ distribution. To measure the exact ridge spacing, we rotate the image by $-\phi$ to align the nanoridges perpendicular to the x-axis. We then average the image along the y axis and obtain a one-dimensional profile for the nanoridges. Next, to achieve subpixel resolution, we interpolate this profile using a cubic spline with a step size of 0.005 pixels. We then calculate the autocovariance function of this profile (the lag of the autocovariance corresponds to a spatial separation). The distance between the first two peaks of the autocovariance is the nanoridge spacing, ρ. We model nanoridges as a sequence of rectangles that are separated by a distance ρ and have an orientation ϕ with respect to the x-axis. We then calculate the cross-correlation between the model nanoridges and the nanoridge profile to measure the spatial offset of the nanoridges, $\delta\rho$. The three variables, ϕ, ρ, and $\delta\rho$ determine the position of each nanoridge. In Fig. A.5, we show the estimated spatial offset as a function of the frame number for each ridge spacing (these plots correspond to the drift of the microscope stage).

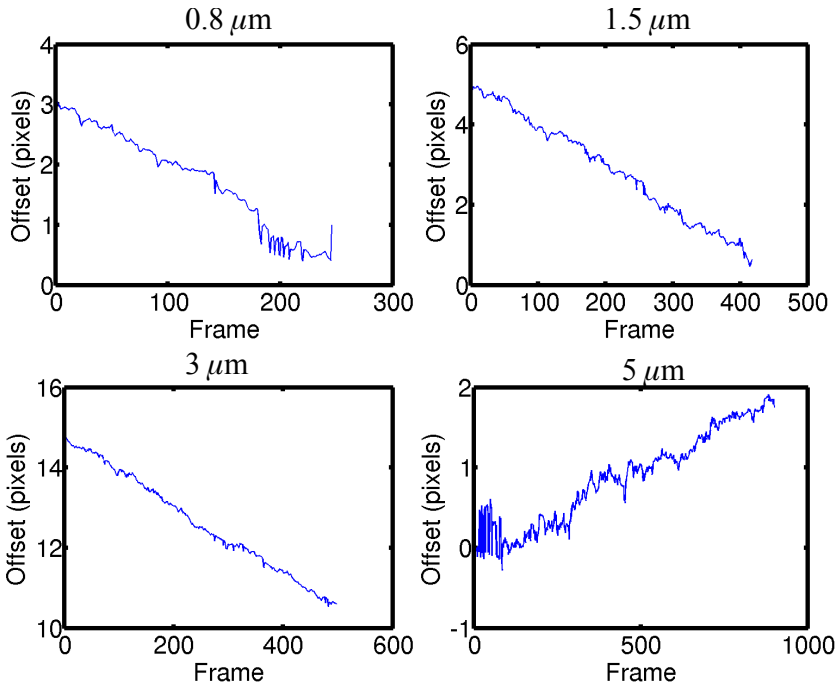

Figure A.5: The measured spatial offset of the ridges as a function of the frame number. A representative data set is shown for each nanoridge spacing.

A.4 Simulation Methods

A.4.1 Activity patterning model

In our simulation, we model the effect of the nanoridges by patterning the nucleation activity on the membrane. This patterning is motivated by the recently seen effects of curvature on Arp2/3 induced branching [85]. We define the activity density of binding events on the ridges and off the ridges as k_r and k_g, respectively. This quantity has units of $\text{min}^{-1}\mu\text{M}^{-1}$. The total membrane nucleation activity density in the simulation chamber, K_{total} is calculated as

$$K_{\text{total}} = w\lambda k_r + (1 - w\lambda)k_g \,. \tag{A.7}$$

Here w is the width of a single ridge and λ is the number density of nanoridges (i.e., number of nanoridges per μm). We modeled the increased activity of nucleation promotion factors on the nanoridges by choosing $k_g < k_r$. For the two rate densities held constant, increasing λ increases the total activity of actin within the cell. This model results in behavior consistent with that seen in the experiments. As an alternative model, we limit the total nucleation promotion activity within the cell (i.e., simulation domain). This constraint can be achieved if the activity rates on and off of the nanoridges are chosen as $k_r = (1/2)K_{\text{total}}/(w\lambda)$ and $k_g = (1/2)K_{\text{total}}/(1 - w\lambda)$, respectively. In Fig. A.8 we show the activity densities as a function of the nanoridge spacing for both k_r and k_g, normalized by the total activity density given in Eq. (A.7). Our simulation results show sharp disagreement between this version of

the model and experimental results for large nanoridge spacings. This disagreement suggests that actin activity is not constrained (Fig. A.9). Results from the two models become comparable and similar to a uniform distribution of polymerized actin for spacings less than 1 μm. All of the parameters in this model are the same as in Ref. [66] except the parameters shown in Tables S1 and S2. We choose these parameters to optimize the visual fit between the numerical simulations and experiments. We increased the area of the simulation domain to look at actin dynamics on a scale comparable to the size of the plasma membrane that is in contact with the substrate. With strong attractive force between the membrane and actin filaments, we observed an increased number of "parasitic" dendritic clusters. When the force is weak, such events are rarer, which reduces the noisiness of the the spatial distribution of actin polymerization. The remaining parameters are changed to mimic the effect of genetic and drug treatment perturbations, as explained in the following section.

Table A.1: Parameters used in simulations that differ from those used in Ref. [66]. Note that there are two actin nucleation rates depending on the location (k_r on nanoridges and k_g on grooves).

Parameter (units)	Ref. [66]	Non-limited	Limited	latrunculin A treatment
L_x (μm)	3	8	8	8
L_y (μm)	3	5	5	5
f_{att} (k_BT/nm)	-0.275	-0.22	-0.22	-0.22
k_{nuc} ($\mu\text{M}^{-1}\text{s}^{-1}$)	0.001	0.001 grooves 0.002 ridges	variable (see Table. A.2)	0.0005 grooves 0.001 ridges
$[G_{\text{actin}}]$ (μM)	0.45	0.45	0.45	0.25 – 0.45

Table A.2: Values of the nucleation rate, k_{nuc}, on nanoridges (k_r and on grooves k_g used in simulations of the limited model.

Spacing (μm)	# nanoridges	k_{nuc} on ridges (1/s) $\times 10^{-3}$	k_{nuc} on grooves (1/s) $\times 10^{-3}$
0.6	13	1.02	0.97
0.8	10	1.33	0.8
1	8	1.66	0.71
1.5	6	2.22	0.65
2	4	3.33	0.59
2.5	4	3.33	0.58
3	3	4.44	0.56
4	2	6.66	0.54
5	2	6.66	0.54

A.4.2 Perturbations to model parameters

We used our actin polymerization model to investigate the change in the behavior of the wave coupling in response to changes to actin polymerization machinery. Experimentally, this perturbation can be achieved by treating cells with latrunculin A. We tested a decrease of 22% in the free actin monomers to see the effect of an intermediate dose of the drug. When free actin monomer concentration is reduced by 33% polymerization of actin is entirely disabled.

We quantified the effect of the perturbations by measuring the parallel component of the wave velocity from the kymographs. Latrunculin A perturbation slows down the waves. Under this perturbation the average wave speed decreases from 5.8 μm/min to 4.2 μm/min. This difference is statistically significant ($p < 10^{-4}$ using Mann-Whitney-U test).

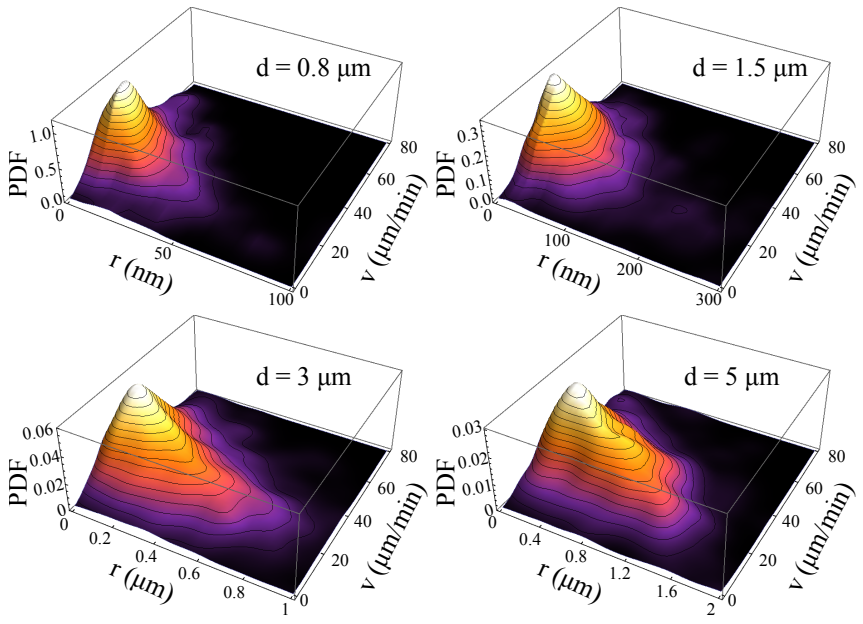

Figure A.6: Joint probability density of experimentally observed actin wave speed and centroid location with respect to the nearest nanoridge.

A.4.3 Implementation of the activity of nucleation promotion factors in a finite domain.

For a finite domain of size $L_x \times L_y$, λ takes discrete values of $\lambda = n/L_x$, where n, the number of ridges, is a function of the ridge spacing, g. Since only a limited number of ridges can fit in a finite simulation domain with fixed ridge spacing, increasing g introduces more off-ridge activity, deviating from the value expected by (A.7). This effect was accounted for in our analysis by choosing ridge spacings large enough that n changes with each g chosen.

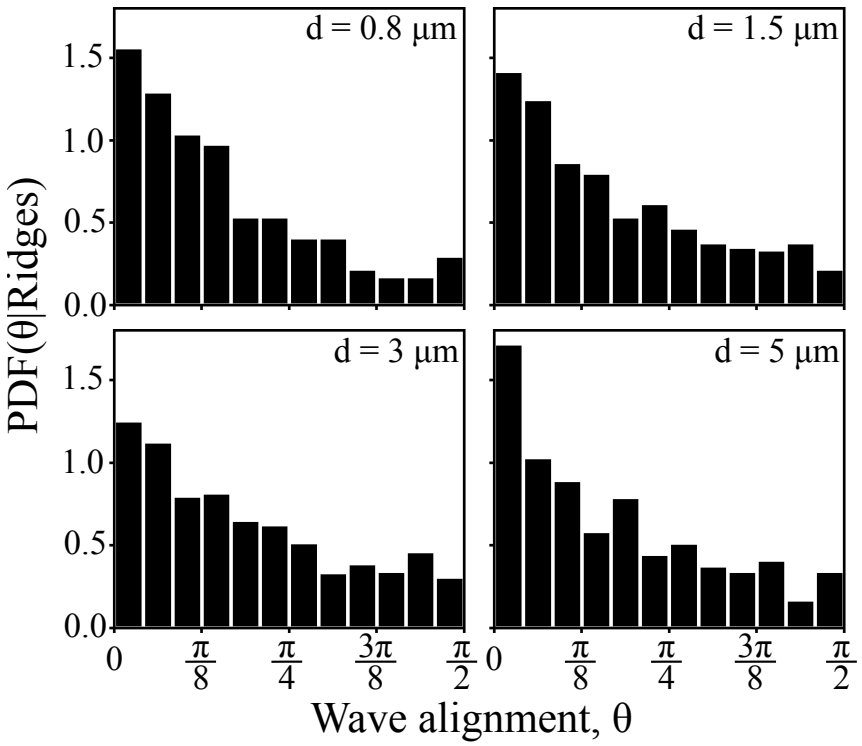

Figure A.7: Probability density of wave alignment for waves that are located in the vicinity of the nanoridges (results from experiments). Location is determined by the position of the wave centroid.

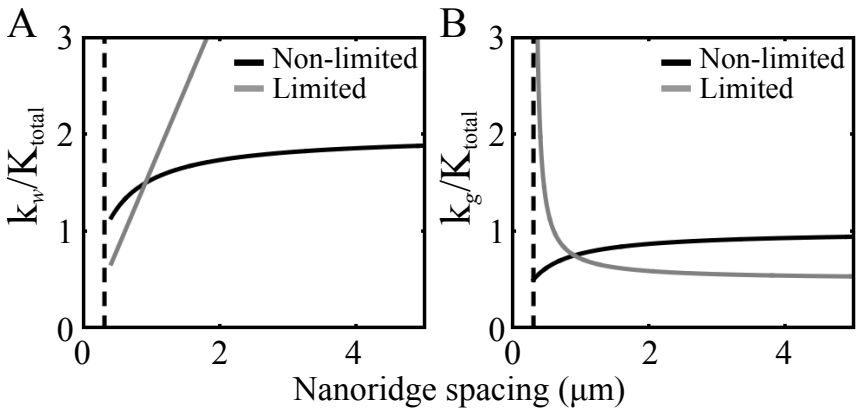

Figure A.8: Activity density of nucleation promotion factors as a function of the nanoridge spacing on the nanoridges (A) and off the nanoridges (B) used in models. The activity density is normalized by the total activity density. Black lines correspond to the model without any biochemical constraints. Gray lines correspond to another model, in which the activity densities on and off the nanoridges are changed such that the total activity within the simulation domain is kept constant. The dashed line indicates the width of the nanoridge, which sets a lower limit for the nanoridge spacing.

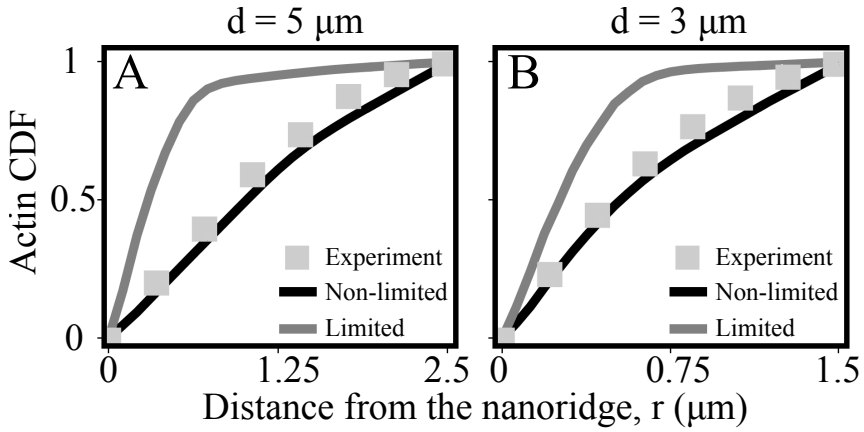

Figure A.9: Cumulative probability, CDF, of actin polymerization with respect to position for (A) 5-μm-spaced and (B) 3-μm-spaced nanoridges. Light gray squares represent experimental results. Black line represents model simulation results, where the total actin activity is increased due to contact with nanoridges and is not biochemically constrained. The dark gray line represents results from an alternative model, in which the actin activity is increased on sites in contact with the nanoridges and the total actin activity is limited.

A.5 Role of depolymerization

To observe how sequestration of free actin monomers affects the preferential polymerization, we monitored the actin waves after addition of 1.25 μM of latrunculin A. Ref. [30] showed that for accommodation of actin polymerization waves the polymerized (F-actin) and actin monomers should be continuously cycled. Furthermore, Ref. [30] showed that despite the global deficiency of actin monomers, actin can still assemble locally at the sites of the plasma membrane that are in contact with the substrate. By impairing the cycling between F- and G-actin we observe how much nanoridges can locally enrich the actin activity. We observe that under this perturbation actin still polymerizes preferentially along the nanoridges. How-

ever, the lack of monomers results in a decrease in the overall actin activity, which is reflected in the wave speed (average speed of 5.2 μm/min).

Appendix B: A guide to wave tracking software

B.1 Actin wave tracking software

In this section details of the actin wave tracking code are provided. The software clusters actin flux vectors based on alignment of neighboring vectors obtained from the fluorescent images.

B.1.1 Input

The input variables include parameters that are related to the location of the stored images and parameters that correspond to the physical quantities of actin polymerization. The function that tracks the actin waves has the format:

```
function fluxClusterDoubleClusterErode(path_name,
file_short, num_digits, number_frames, noiseSmoothRadius,
informationSmoothRadius, erodeRadius, lower_threshold,
save_on, save_path)
```

The first four input parameters enables determination of the image stack that will be processed by the actin-wave tracking code. The remaining four parameters are related to the physical quantities of actin polymerization and will be explained

below. The last two parameters determine whether the analysis outputs will be saved in the system.

B.1.2 Actin flux calculation

To track actin waves, we need first to calculate the flux vectors from the fluorescent images. The outline of this process was explained in Appendix A.1. The operations explained in that section are performed as follows:

```
filename = [path_name file_short];
to_filename = ['%0' num2str (num_digits) 'u.tif'];

% run once with inflated filters
noiseSmoothRadiusP = 2.0*noiseSmoothRadius;
informationSmoothRadiusP = 8.0*informationSmoothRadius;
lower_thresholdP = 15;

% initialize first iteration
timeFlag = true;
indexLR=[];
indexUD=[];
indexFB=[];

% noise smoothing filter
```

```
gauss_filter _noise =
fspecial('gaussian', round(10*noiseSmoothRadiusP), noiseSmoothRadiusP);

% information smoothing filter
gauss_filter _info =
fspecial('gaussian', round(10*informationSmoothRadiusP),
informationSmoothRadiusP);

% iterate through the frames
for f=1:number_frames-1

% read the images from each frame and the next
filename1 = sprintf(to_filename, f);
image1 = double(imread([filename filename1]));
filename2 = sprintf(to_filename, f+1);
image2 = double(imread([filename filename2]));

% create the diference image
imageDif = image2-image1;

% smooth the diference image
imageDif = imfilter(imageDif, gauss_filter _noise, 'replicate');
```

```
% smooth the first image

smoothed_image1 = imfilter(image1, gauss_filter _info, 'replicate');


% set a lower threshold on the differance image (threshold)

imageDif = imageDif.*(imageDif>lower_thresholdP);


% take the gradient of the smoothed image

[grad_x, grad_y] = gradient(smoothed_image1,1);


% normalize the gradient (threshold)

normalization = sqrt(grad_x.^2 + grad_y.^2);

grad_x _normal = grad_x./normalization;

grad_y _normal = grad_y./normalization;


% multiply the image difference by the gradient

measure_x = imageDif.*(-1*grad_x _normal);

measure_y = imageDif.*(-1*grad_y _normal);


% find the measure magniture and direction at every pixel

measureDir = mod(atan2(-1*measure_y, measure_x), 2*pi);
```

B.1.3 Clustering of actin flux vectors

The quantity *measureDir* is the vector field that corresponds to the flux vectors based on the apparent flow of actin. In this section, the code for clustering of these vectors is provided. The clustering is performed based on how parallel the flux vectors are with respect to their neighbors.

```
% threshold for defining parallel vectors
epsilon = 0.1;


% filter for non-zero elements
measureFilter = measureDir > 0;


% initialize variables
timeFlag = true;
indexLR=[];
indexUD=[];
indexFB=[];
[rowNum, colNum] =
size(double(imread([filename sprintf(to_filename, 1)])));


% make a left right shift and find edges
edgesLR = cos(measureDir - circshift(measureDir,[0 -1]))>epsilon;
```

```
% filter 0-0 interactions to the left
edgesLR = edgesLR.*measureFilter;

% modify the filter to eliminate 0-0 interactions to the right
filterLR = circshift(measureFilter,[0 -1]);

% eliminate the 0-0 interactions
edgesLR = edgesLR.*filterLR;

% eliminate false interactions
edgesLR = [edgesLR(:,1:end-1) zeros(rowNum,1)]';

% find corresponding indices
indexLR = [indexLR indexList(edgesLR(:)>0)];



% make an up down shift and find edges
% run filters similar to LR edges
edgesUD = cos(measureDir - circshift(measureDir,[-1 0]))>epsilon;
edgesUD = edgesUD.*measureFilter;
filterUD = circshift(measureFilter,[-1 0]);
edgesUD = edgesUD.*filterUD;
edgesUD = [edgesUD(1:end-1,:); zeros(1,colNum)]';
```

```
indexUD = [indexUD indexList(edgesUD(:)>0)];


% make a time shift and find temporal edges
if timeFlag
measureDirOld = measureDir;
measureMagOld = measureMag;
measureFilterOld = measureFilter;
timeFlag = false;
else
edgesFB = cos(measureDir - measureDirOld)>epsilon;
edgesFB = edgesFB.*measureFilter;
edgesFB = edgesFB.*measureFilterOld;
edgesFB = edgesFB';
indexFB = [indexFB indexList(edgesFB(:)>0)];
measureDirOld = measureDir;
measureMagOld = measureMag;
measureFilterOld = measureFilter;
end


% end the frame iteration
end
```

These edges are only defined from one node to another (i.e., they are directional). To cluster them the adjacency network needs to be bidirectional. Therefore, we need to add new edges by reversing the direction of the existing edges.

```
% collect all edges
indexSparse1 = [indexLR, indexUD, indexFB];


% flip the direction of former edges
indexSparse2 = [indexLR+1, indexUD+colNum, indexFB-rowNum*colNum];


% generate a sparse adjacency matrix
sparseIndex = sparse([indexSparse1 indexSparse2],
[indexSparse2 indexSparse1], 1);
```

Next, we find the clusters in the adjacency matrix.

```
% find clusters in the adjacency matrix
[~, C] = graphconncomp(sparseIndex);


% padding
C = [C zeros(1,rowNum*colNum*(number_frames-1)-length(C))];


% convert clusters to a data cube
C = permute(reshape(C,[colNum rowNum number_frames-1]), [2 1 3]);
```

Finally, we only select the temporal connections from the initial clustering process

```
% filter for keeping non-zero elements

goodFilter = C>0;


% find the temporal links

filterTmp = (C(:,:,1:end-1)-C(:,:,2:end))==0;

filterTmp = filterTmp.*goodFilter(:,:,1:end-1);
```

B.1.4 Refining the clusters

First, we erode the temporal links obtained in the first clustering process

```
% initialize temporal links

indexFB = [];


% erosion filter

erosion_filter = strel('disk',erodeRadius);


% erode the inflated clusters in each time frame

for f=1:number_frames-2


indexList = (f-1)*rowNum*colNum+1:1:f*rowNum*colNum;

edgesFB = imerode(filterTmp(:,:,f),erosion_filter);
```

```
edgesFB = edgesFB';

indexFB = [indexFB indexList(edgesFB(:)>0)];


end
```

Using the eroded temporal links, we perform a secondary clustering with smaller smoothing kernels.

```
% initialize spatial links

indexLR=[];

indexUD=[];


% noise smoothing filter

gauss_filter _noise =

fspecial('gaussian', round(10*noiseSmoothRadius),

noiseSmoothRadius);


% information smoothing filter

gauss_filter_info =

fspecial('gaussian', round(10*informationSmoothRadius),

informationSmoothRadius);


% iterate through the frames

for f=1:number_frames-1
```

```
% read the images from each frame and the next

filename1 = sprintf(to_filename, f);

image1 = double(imread([filename filename1]));

filename2 = sprintf(to_filename, f+1);

image2 = double(imread([filename filename2]));


% create the diference image

imageDif = image2-image1;


% smooth the diference image

imageDif = imfilter(imageDif, gauss_filter _noise, 'replicate');


% smooth the first image

smoothed_image1 = imfilter(image1, gauss_filter _info, 'replicate');


% set a lower threshold on the differance image (threshold)

imageDif = imageDif.*(imageDif>lower_threshold);


% take the gradient of the smoothed image

[grad_x, grad_y] = gradient(smoothed_image1,1);


% normalize the gradient (threshold)
```

```
normalization = sqrt(grad_x.^2 + grad_y.^2);

grad_x _normal = grad_x./normalization;

grad_y _normal = grad_y./normalization;


% multiply the image difference by the gradient

measure_x = imageDif.*(-1*grad_x _normal);

measure_y = imageDif.*(-1*grad_y _normal);


% find the measure magniture and direction at every pixel

measureDir = mod(atan2(-1*measure_y, measure_x), 2*pi);


% make a left right shift and find edges

edgesLR = cos(measureDir - circshift(measureDir,[0 -1]))>epsilon;

edgesLR = edgesLR.*measureFilter;

filterLR = circshift(measureFilter,[0 -1]);

edgesLR = edgesLR.*filterLR;

edgesLR = [edgesLR(:,1:end-1) zeros(rowNum,1)]';

indexLR = [indexLR indexList(edgesLR(:)>0)];


% make an up down shift and find edges

edgesUD = cos(measureDir - circshift(measureDir,[-1 0]))>epsilon;

edgesUD = edgesUD.*measureFilter;

filterUD = circshift(measureFilter,[-1 0]);
```

```
edgesUD = edgesUD.*filterUD;

edgesUD = [edgesUD(1:end-1,:); zeros(1,colNum)]';

indexUD = [indexUD indexList(edgesUD(:)>0)];


end


% generate a sparse adjacency matrix

indexSparse1 = [indexLR, indexUD, indexFB];

indexSparse2 = [indexLR+1, indexUD+colNum, indexFB+rowNum*colNum];

sparseIndex =

sparse([indexSparse1 indexSparse2],

[indexSparse2 indexSparse1], 1);


% cluster spatial neighbors

[~, C] = graphconncomp(sparseIndex);

C = [C zeros(1,rowNum*colNum*(number_frames-1)-length(C))];

C = permute(reshape(C,[colNum rowNum number_frames-1]), [2 1 3]);


% make a left-right comparison

filtTemp = (C(1:end-1,:,:)-C(2:end,:,:))==0;

goodFilterLR = [filtTemp; false(1,colNum,number_frames-1)];

goodFilterRL = [false(1,colNum,number_frames-1); filtTemp];
```

```
% make an up-down comparison

filtTemp = (C(:,1:end-1,:)-C(:,2:end,:))==0;

goodFilterUD = [filtTemp, false(rowNum,1,number_frames-1)];

goodFilterDU = [false(rowNum,1,number_frames-1), filtTemp];


% make a temporal comparison

filterTmp = (C(:,:,1:end-1)-C(:,:,2:end))==0;

goodFilterFB =filterTmp;

goodFilterFB(:,:,number_frames-1) = false(rowNum,colNum,1);

goodFilterBF(:,:,1) = false(rowNum,colNum,1);

goodFilterBF(:,:,2:number_frames-1) = filterTmp;


% combine all the filters

goodFilter =

goodFilterLR | goodFilterRL |

goodFilterUD | goodFilterDU |

goodFilterFB | goodFilterBF;

C = C.*goodFilter;


% relabel cluster id's

listCluster = unique(C);

for i=1:length(listCluster)

C(C==listCluster(i)) = -i;
```

```
end

C = abs(C);


% save clusters

if save_on

    save([save_path 'clusterCube'], 'C', '-v7 .3');

end
```

The variable C contains the spatio-temporal position of each cluster element.

B.2 Ridge detection software

In this section details of the ridge detection code are provided. The software extracts the position of nanoridges from the bright-field images in which both cells and nanoridges are visible.

B.2.1 Input

The software only uses the directory and the format of the bright-field images as input. A few parameters are carefully chosen for the appearance of nanoridges in bright-field microscopy. The procedures estimate the spacing between adjacent nanoridges, the orientation of nanoridges, the width of the nanoridges and the offset of the first nanoridge with respect to the origin of the image. The name of the function that performs all these procedures is:

```
function [spacing, width, angle, offset] =
```

```
modelNanoridges(path_name, num_images, small_switch)
```

Here, the first input is the name of the folder in the system, where the images are located. The second input is the total number of images in the stack. The software assumes that the images are located in a subfolder named "bright" and are named as "tXXXX.tif", where XXXX is a four-digit number denoting the time point of the image in the stack (e.g., t0001.tif, t0177.tif etc.)

```
% create filename variables
num_digits = 4;
filename = [path_name 'bright/t'];
to_filename = ['%0' num2str (num_digits) 'u.tif'];

% initiate output variables
angle = zeros(1,num_images);
spacing = angle;
width = angle;
offset = angle;
spacingTest = angle;

% define parameters
spline_stepSize = 0.005;
edge_cutoff = 100;
```

Based on these assumptions all of the images in the stack are loaded and later processed with a for loop

```
for i = 1:num_images


% display progress
if mod(i,10) == 1
disp([’  ’ num2str (i) ’ of ’ num2str (num_images) ’ frames’])
end


% open the image
filenameEnd = sprintf(to_filename, i);
image = imread([filename filenameEnd]);


% measure orientation and rough spacing
[angle(i), spacingTest(i)] = measureAngle(image);


% measure spacing at subpixel resolution
imageRot = rotateImageNaN(imadjust(image), -angle(i));
spacing(i) = measureRidgeSpacing(imageRot,
spacingTest(i), spline_stepSize, edge_cutoff);


% measure width at subpixel resolution
```

```
width(i) = measureRidgeWidth(imageRot,
spacing(i), spline_stepSize, edge_cutoff);

% measure offset
offset(i) = estimateOffset(imageRot,
spacing(i), width(i), spline_stepSize, edge_cutoff);

end
```

The subfunctions that estimate the spacing, orientation, width and offset were explained in the following sections.

B.2.2 Estimating the orientation of nanoridges

In the first procedure, we detect the orientation of the nanoridges and make a rough estimate of the nanoridge spacing using the function *measureAngle*. In this procedure we first perform "Prewitt" edge detection to extract the lines from the image.

```
function [orientation, roughSpacing] = measureAngle(image)

% edge detection
BW = edge(image,'prewitt');
```

We then perform a Hough transformation (alternatively one can also run a Radon transformation) on BW to estimate the orientation of nanoridges:

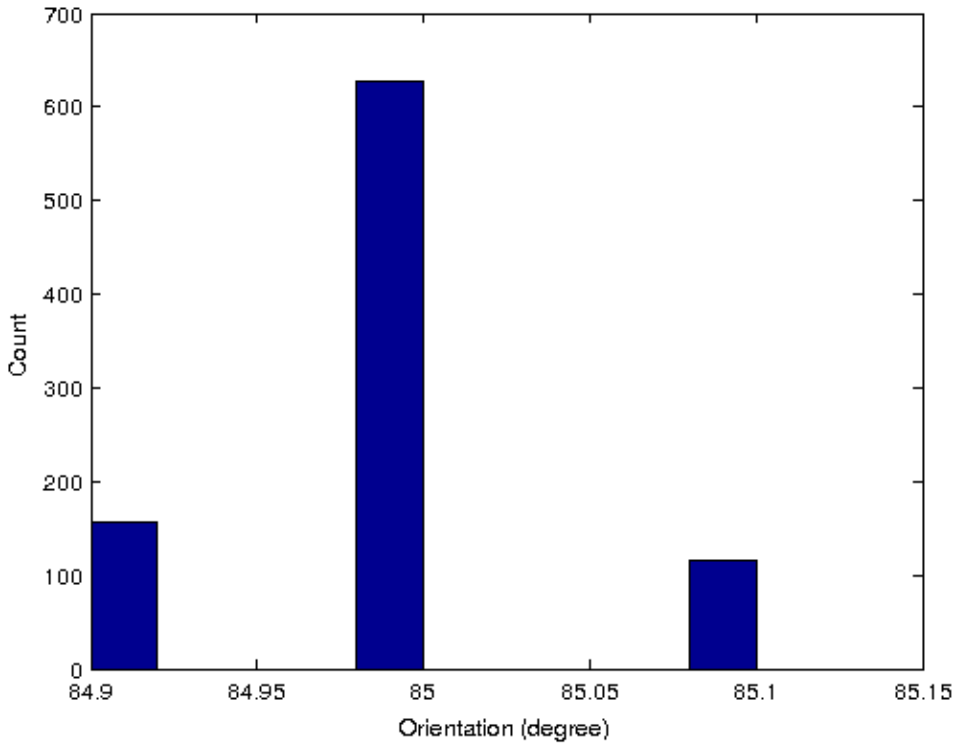

Figure B.1: The orientation of nanoridges measured over 900 frames, using the *measureAngle* function. The measurement is consistent over the course of the experiment.

```
% hough transform and find peaks

thetaRange = -90:0.1:89;

[H,T,R] = hough(BW,'RhoResolution',0.5,'Theta',thetaRange);

P  = houghpeaks(H,30);


% most-likely orientation

orientation = mode(T(P(:,2)));
```

This algorithm can determine the orientation of the nanoridges with a resolution of 0.1 degrees. The distribution from an experiment is shown in Fig. B.1.

Finally, using the positions of the lines extracted by the Hough transform we estimate the nanoridge spacing with

```
% calculate rough spacing for cross-check
spacingDist = R(P(:,1));
spacingDist = sort(spacingDist, 'ascend');
spacingTmp = diff(spacingDist);
roughSpacing = mode(spacingTmp);
end
```

In this approach, we calculate the difference between the adjacent lines that are obtained from the peaks extracted from the Hough transformation. Then we estimate the spacing as the most frequent distance between the adjacent nanoridges. This distance does not have subpixel resolution. However, it provides a simple cross-check value for the estimated spacing.

B.2.3 Estimating the nanoridge spacing

The function that estimates the spacing between adjacent nanoridges is called:

```
function spacing = measureRidgeSpacing(image,
spacingTest, spline_stepSize, edge_cutoff)
```

This function requires a rotated bright-field image such that the nanoridges are parallel to the vertical axis. In the main function, this rotation is provided by the *rotateImageNaN* function, which is a custom-written function that rotates an

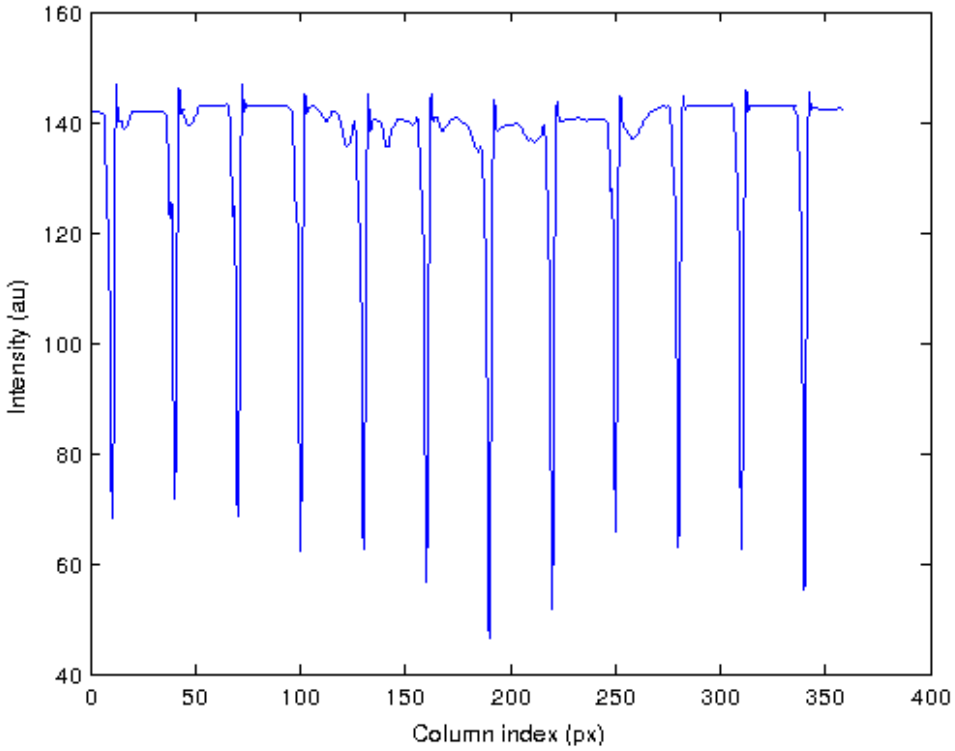

Figure B.2: After projecting the image in th vertical direction and performing spline, nanoridges can be approximated with aa square-wave signal.

image and fills the padded regions with NaN's. This function is not written as a subprocedure. Instead it is saved in the same directory as the main function. The code for *rotateImageNaN* is provided later in this subsection.

Next, we will estimate the nanoridge spacing with the following operations. First, we will average over the rows to obtain a square-wave signal that corresponds to the nanoridges. Then, we will interpolate this function with spline to attain subpixel resolution.

```
% find the y-projection of the image
```

```
%(that means average over y i.e. rows)
meanCol = nanmean(image,1);


% fit a spline to the projection
xxCol = 0:spline_stepSize:
length(meanCol(edge_cutoff:end-edge_cutoff));
meanColEdge = meanCol(edge_cutoff:end-edge_cutoff);
yyCol = spline(1:length(meanColEdge), meanColEdge, xxCol);
```

An example for the square-wave-like signal representing the nanoridges is shown in Fig. B.2. Then we use the autocovarience function to extract the spacing:

```
% find the auto-correlations of the x- and y-projections
[meanColCor, lags] = xcov(yyCol);


% find the periodicity
[~, colLocs] = findpeaks(meanColCor, 'SORTSTR', 'descend');
spacing = abs(colLocs(1) - colLocs(2))*spline_stepSize;
```

A representative covariance function of this signal is shown in Fig. B.3. The peaks in the covariance function correspond to a good match between the original signal and the shifted signal, which is shifted with a delay associated with the peak. Therefore, by calculating the distance between the two largest peaks we can estimate the nanoridge spacing.

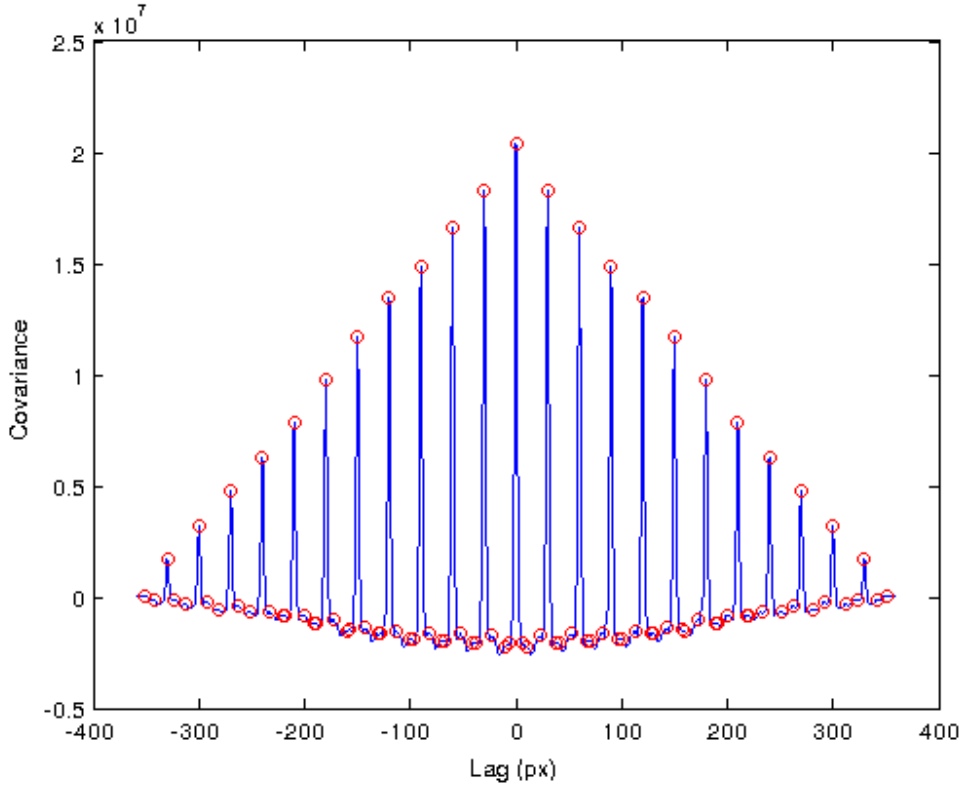

Figure B.3: Autocovariance function of the nanoridges. The spacing of the nanoridges is obtained from the distance between adjacent peaks.

In the final step, we compare the spacing to a rough estimate of the spacing obtained from the Hough transformation. This estimate is calculated in *measureAngle* function. If the discrepancy between the two values is fairly large (greater than 20%), we recalculate the spacing using the statistics of the distribution of all distances between all adjacent peaks.

```
% cross-check with rough spacing.
% Do statistical analysis if the discrepancy is not tolerable
epsilon = 1;
peakRange =  0.8*spacingTest;
peakDistance = round(peakRange/spline_stepSize);

% check if peakDistance is positive
if peakDistance <= 0
% try spacing instead of spacingTest
peakDistance = round(0.8*spacing/spline_stepSize);
end

% if spacing doesn't work, default to 1
if peakDistance <= 0
peakDistance = 1;
end
if abs(spacing-spacingTest) > epsilon
```

```
[~, colLocs] = findpeaks(meanColCor,
 'MINPEAKDISTANCE', peakDistance, 'SORTSTR', 'descend');
properDist = sort(lags(colLocs));
spcTmp = zeros(1,length(properDist)-1);
for i=1:length(properDist)-1
spcTmp(i) = abs(properDist(i)properDist(i+1))*spline_stepSize;
end
spacing = mean(spcTmp);
end
end
```

This method is a fairly robust way of estimating the nanoridge spacing. The distribution of the measured values for the spacing over an experiment is shown in Fig. B.4.

Finally, we show the code for *rotateImageNaN* function, which rotates an image with a given angle in the clockwise direction and fills the padded regions with NaN's:

```
function imageRotated = rotateImageNaN(image, angle)
% rotate image
imageRotated = imrotate(image+100, -angle, 'bilinear', 'loose');

% replace padded zeros with NaN's
imageRotated(imageRotated == 0) = NaN;
```

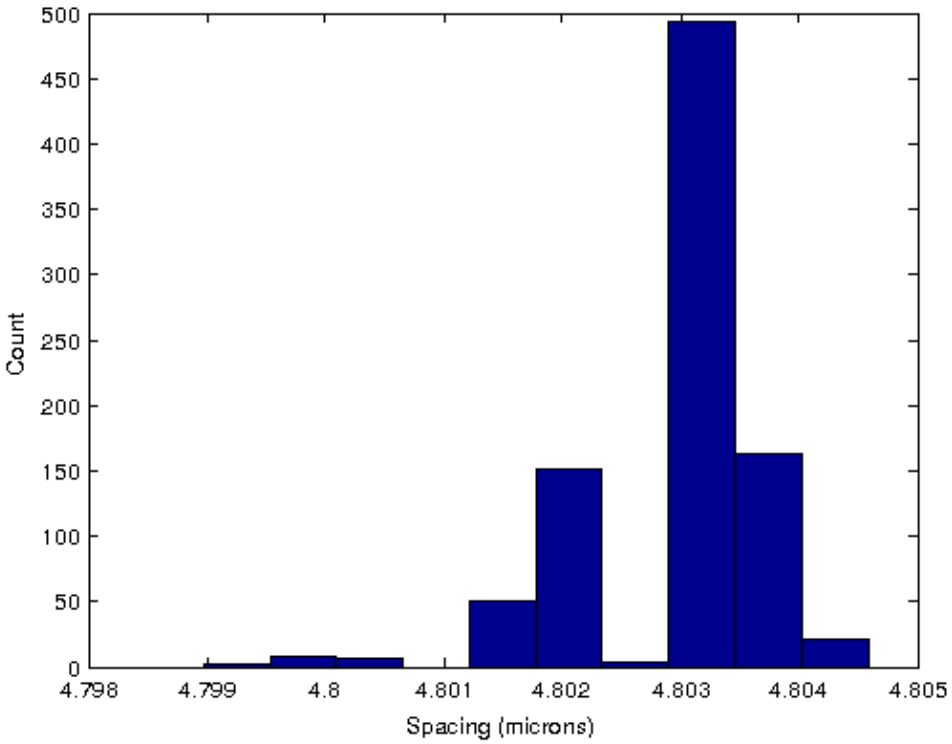

Figure B.4: The distribution of measured values for the nanoridge spacing. The algorithm is capable of measuring the spacing with a small uncertainty.

```
% pad edges with NaN's too
imageRotated = imageRotated - 100;
edge_mask = isnan(imageRotated);
se = strel('square', 3);
edge_mask = imdilate(edge_mask,se);
imageRotated(edge_mask == 1) = NaN;
end
```

B.2.4 Measuring the nanoridge width

The width of the fabricated nanoridges is around 200-300 nm, which is close to the diffraction limit. For simplicity we can assume the width as two pixels (in the experiments images are oversampled by a factor of two). However, for generality, the algorithm for measuring the nanoridge width is provided in this section. The procedure is similar to measuring the nanoridge spacing. The function that measures the nanoridge width is:

```
function width = measureRidgeWidth(image,
spacing, spline_stepSize, edge_cutoff)

% find the y-projection of the image
% (that means average over y i.e. rows)
% to find the width peaks in the derivative are used
```

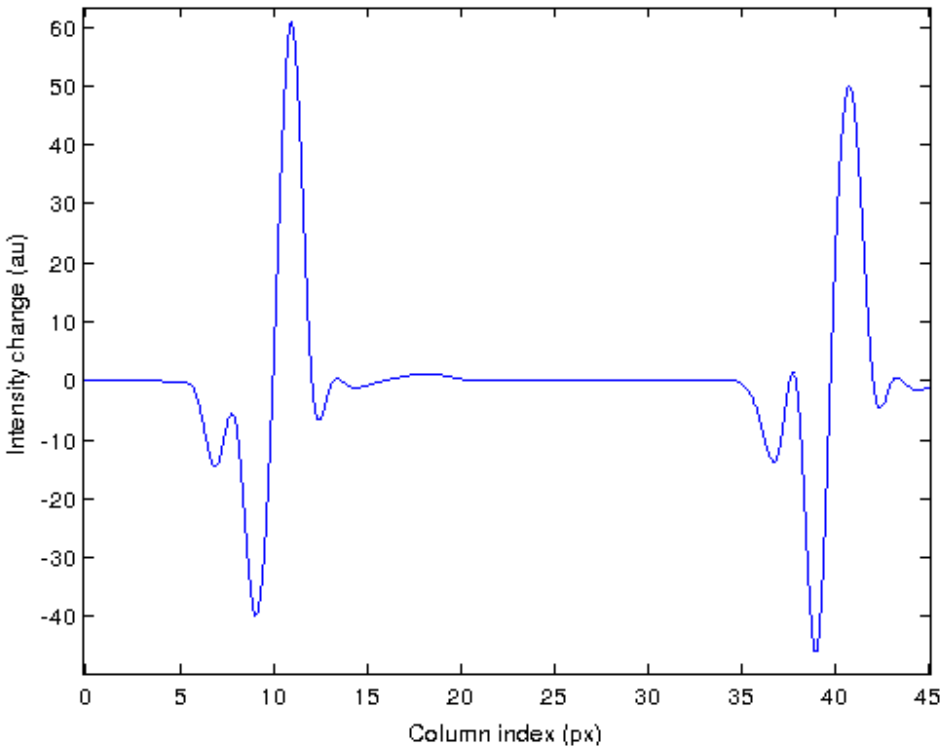

Figure B.5: To measure the nanoridge width the derivative of the square-wave signal is used. The width is estimated from the distance between crests and troughs of this signal.

```
meanCol = nanmean(image,1);

meanCol = diff(meanCol(edge_cutoff:end-edge_cutoff));
```

Instead of the square-wave, we will analyze its derivative, which has a characteristic form shown in Fig. B.5. Nanoridges appear dark in the bright-field images. The intensity difference between two neighboring pixels is large when these two pixels are in the transition region from a groove to a nanoridge and vice and versa. Therefore, the width can be estimated from the distance between crests and troughs of the derivative of the signal. We look at the autocovariance function of the derivative of the square-wave signal.

```
% fit a spline to the projection
xxCol = 0:spline_stepSize:length(meanCol);
yyCol = spline(1:length(meanCol), meanCol, xxCol);

% find the auto-correlations of the x- and y-projections
[meanColCor, lags] = xcov(yyCol);

% find the periodicity
[~, colLocs] = findpeaks(-meanColCor, 'SORTSTR', 'descend');
width = abs(lags(colLocs(1)))*spline_stepSize;
```

The autocovarience between a crest and a trough is negative and maximum in absolute value. Therefore, the lag that corresponds to the minimum autocovariance yields the estimate for the nanoridge width. A representative autocovariance function of the derivative of the square-wave signal is shown in Fig. B.6.

Similar to the estimation of the spacing, we perform a statistical test for the measured width to ensure that the measured value is within a reasonable interval.

```
% do a statistical check
% if statistically obtained value deviates 20% from the one obtained
% from maximum anticorrelation, trust the statistically obtained value
epsilon = 0.2;
maxAntiCorrelation = -min(meanColCor);
[~, colLocs] = findpeaks(-meanColCor,
```

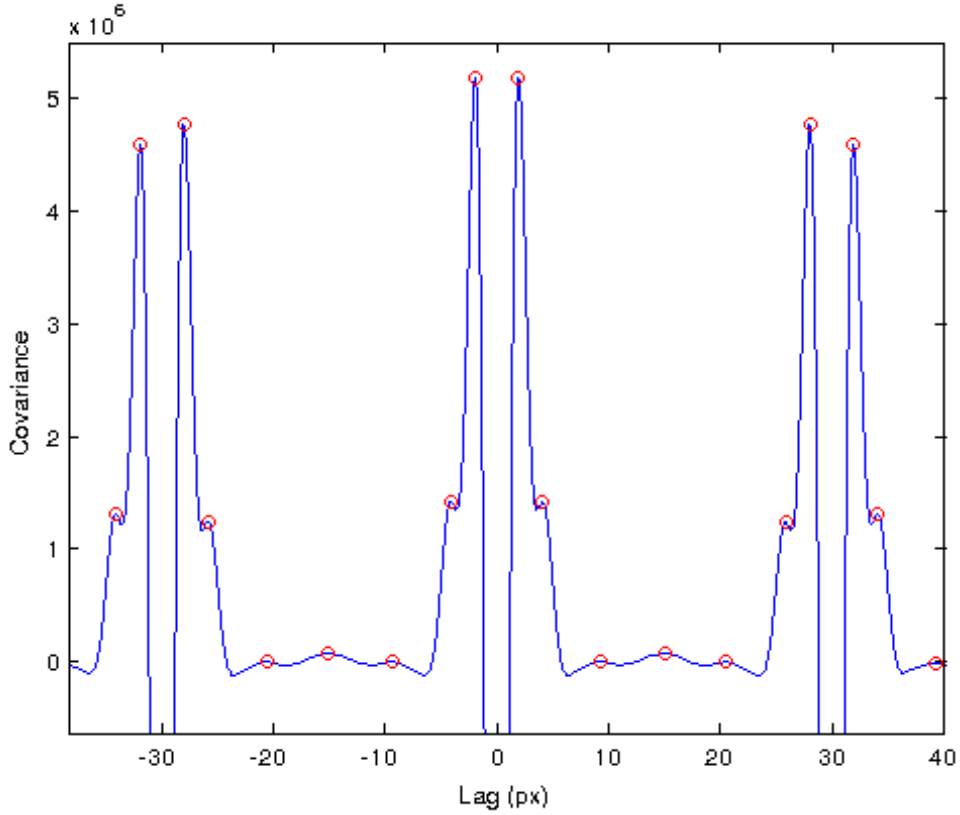

Figure B.6: The widths of the nanoridges are estimated from the lag associated with the minimum autocovariance, which corresponds to a lag between crests and troughs of the derivative of the square-wave signal.

```
'MINPEAKHEIGHT', 0.5*maxAntiCorrelation);
properDist = lags(colLocs)*spline_stepSize;
widthDist = mod(properDist, spacing);
widthTmp = mean([mean(widthDist(widthDist<0.5*spacing)),
spacing - mean(widthDist(widthDist>0.5*spacing))]);

if abs(widthTmp - width) > epsilon*width
    width = widthTmp;
end
end
```

The distribution of measured width is shown in Fig. B.7.

B.2.5 Estimating the offset

To recreate the nanoridges precisely, we need the offset of the first nanoridge from the origin. This quantity can be estimated in a manner similar to the one used to obtain the nanoridge spacing. First, we generate a square wave with zero offset using the nanoridge spacing and nanoridge width that were extracted from the bright-field images.

```
function offset = estimateOffset(image,
spacing, width, spline_stepSize, edge_cutoff)

% find the y-projection of the image
```

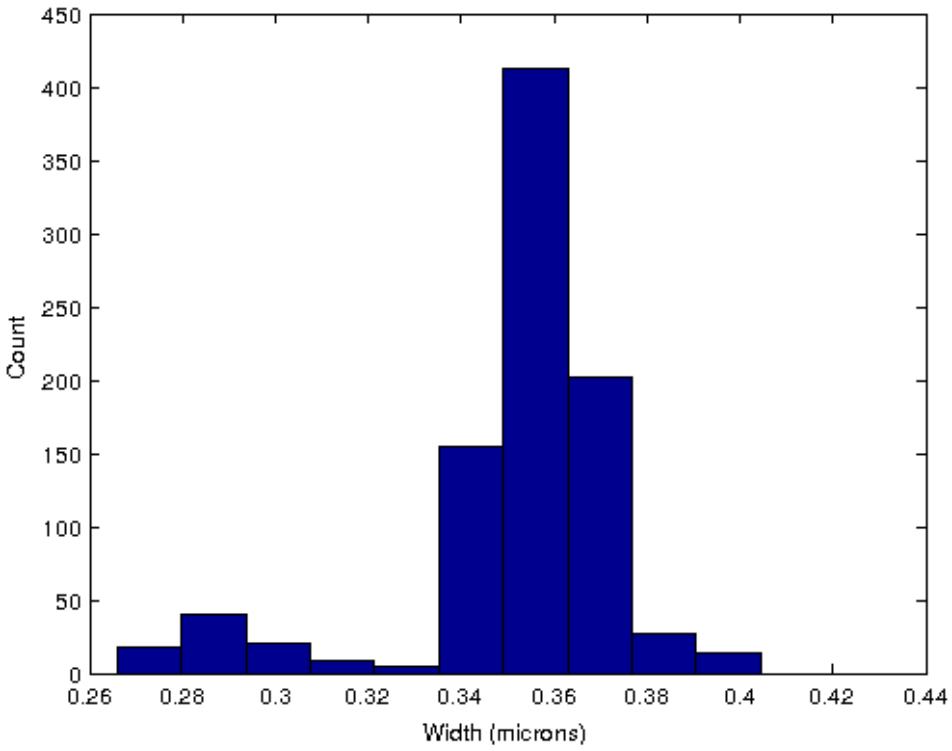

Figure B.7: The distribution of the measured nanoridge widths.

```
%(that means average over y i.e. rows)
meanCol = nanmean(image,1);


% fit a spline to the projection
xxCol = 0:spline_stepSize:length(
meanCol(edge_cutoff:end-edge_cutoff));
meanColEdge = meanCol(edge_cutoff:end-edge_cutoff);
yyCol = spline(1:length(meanColEdge), meanColEdge, xxCol);
yyCol = (yyCol - min(yyCol))/(max(yyCol) - min(yyCol));
signalLength = length(yyCol);


% Second, construct a square wave
% from measured spacing and width
modelSignal = zeros(1,signalLength);
widthPx = round(width/spline_stepSize);
spacingPx = round(spacing/spline_stepSize);
groovePx = spacingPx - widthPx;
repLength = floor(1.0*signalLength/spacingPx);
grooveStart = (widthPx:spacingPx:widthPx+repLength*spacingPx)+1;
grooveEnd = grooveStart + groovePx - 1;
for i=1:length(grooveStart)-1
    groovePattern = grooveStart(i):1:grooveEnd(i);
    modelSignal(groovePattern) = 1;
```

```
end
residue = signalLength - grooveEnd(end-1);
if residue>=spacingPx
    groovePattern = grooveStart(end):1:grooveEnd(end);
    modelSignal(groovePattern) = 1;
elseif residue>widthPx
    groovePattern = grooveStart(end):1:signalLength;
    modelSignal(groovePattern) = 1;
end
```

The original square wave and the reconstructed square wave are shown in Fig. B.8. The mismatch between the two signals corresponds to the offset. Next, we will calculate the covariance function of this signal with respect to the measured signal to obtain the offset.

```
% Correlate the two signals and find the phase gap
[signalCov, lags] = xcov(modelSignal,yyCol);
[~, phase] = max(signalCov);
phase = mod(lags(phase), spacingPx);

% calculate offset
offset = -phase*spline_stepSize;
end
```

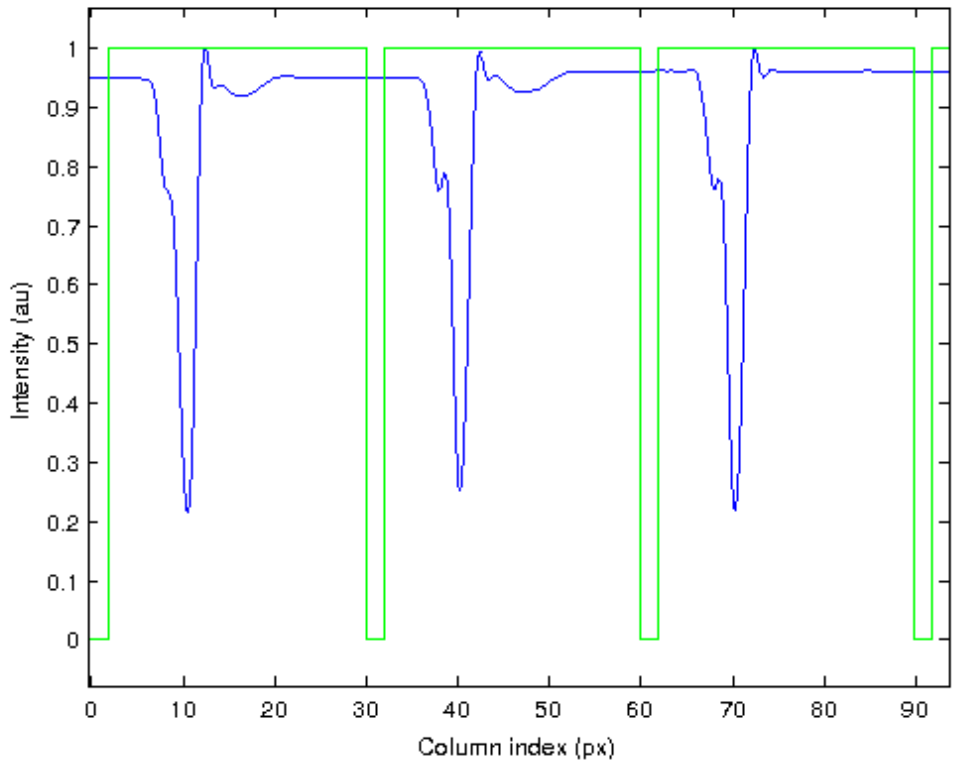

Figure B.8: A square-wave signal was constructed from the measured spacing and width in order to model the nanoridges (green). The model signal was compared with the original signal (blue). The mismatch between the two signals corresponds to the offset.

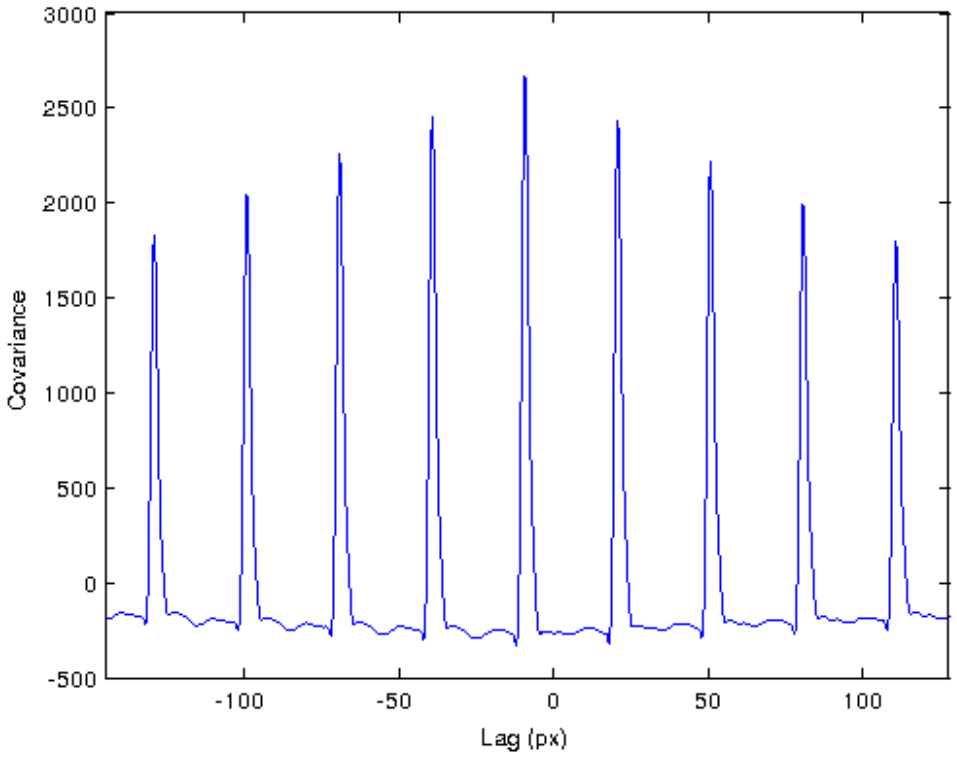

Figure B.9: The covariance function of nanoridges with modeled nanoridges. The lag of the maximum covariance corresponds to the offset between the two signals.

The covariance function is maximized when one of the signals has the greatest overlap with the other signal for a given lag. A representative covariance function is shown in Fig. B.9.

From this lag, we determine the offset. The corrected square wave that models the nanoridges is plotted in Fig. B.10.

The measured offset as a function of time is shown in Fig. B.11. We can see the drift of the microscope stage from the time series of this quantity. These four variables—spacing, width, offset, and orientation—completely model the nanoridges. Using these variables we can analyze the localization of actin waves with respect to

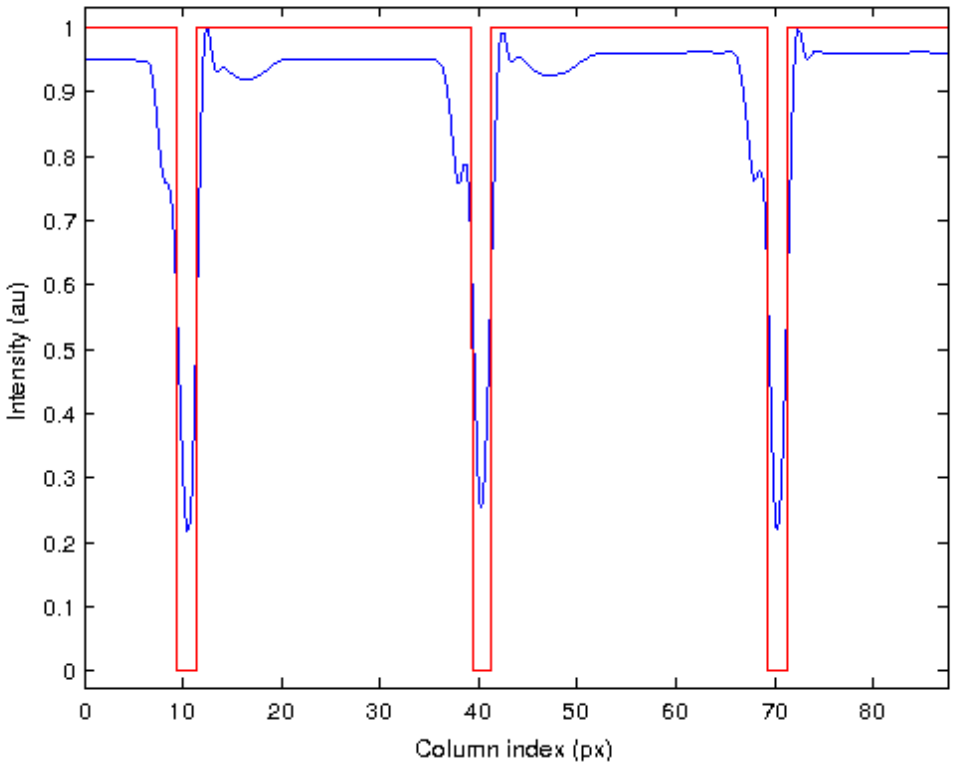

Figure B.10: The corrected square-wave that models the nanoridges (red) compared with the original square-wave signal obtained from the nanoridges (blue).

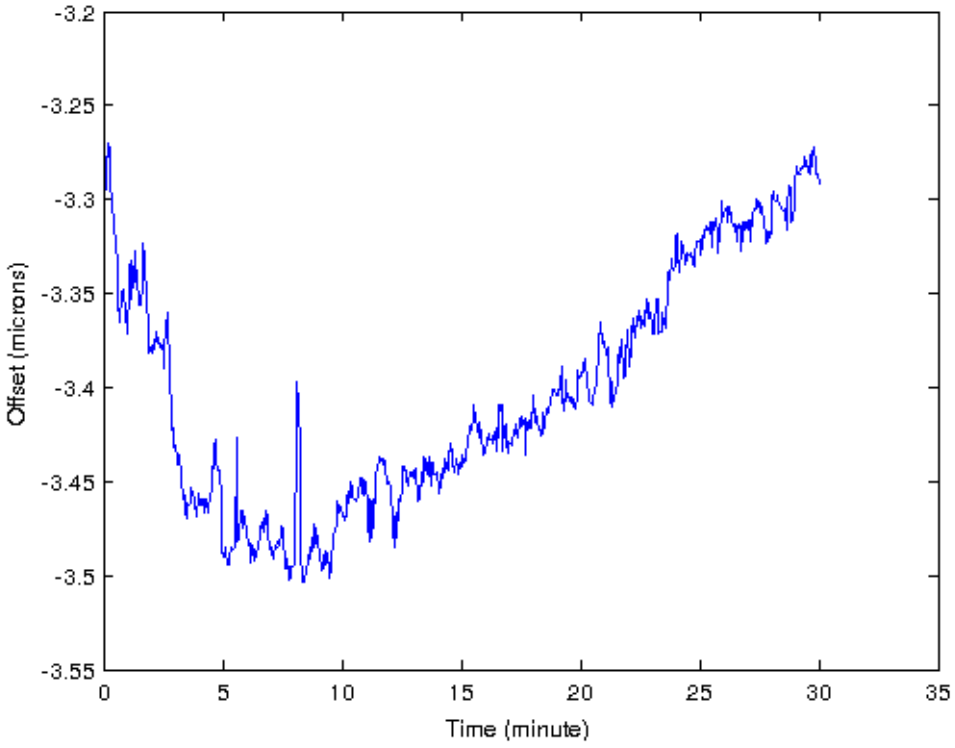

Figure B.11: The offset is plotted as a function of time. The jitter and the drift of the microscope stage can be seen. The measured offset does not exhibit any significant discontinuities. This observation suggests that the offset estimation is accurate.

the closest nanoridge.

Appendix C: Supplementary information for "Signal relay in noisy directed migration of cell groups"

In this section, details regarding the assumptions used in our signal relay model are provided. In addition, we compare numerical results with experimental observations presented in Chapter 4.

C.1 Nonuniform hydrolysis profile approximation

To observe aggregation, cells are starved in a shaking flask with low concentration cAMP pulses for 5 hours. During this period the cells differentiate and secrete chemicals as a byproduct of the development process. Phosphodiesterase (PDE) which hydrolyzes the signaling molecule cAMP, is secreted at a relatively constant rate during the preparation [140]. The activity of the PDE inhibitor is reduced for our method of pulsing [141]. Thus, we approximate the PDE density as $n_{\mathrm{PDE}} = n_{\mathrm{cell}} s_{\mathrm{PDE}} T$, where n_{cell} is the cell density, s_{PDE} is the rate of PDE production per cell per unit time (assumed to be constant), and $T = 5$ hours is the total preparation time. Once the cells are placed in the $y < 0$ reservoir they settle quickly to its bottom surface. After settling is complete the cell surface density is $\bar{n}_{\mathrm{cell}} = n_{\mathrm{cell}} L_z$, where $L_z = 1$ cm is the height of the reservoir [94]. In the

$0 \leq y \leq L_y$ region, the dynamics of the enzyme PDE reaches a steady state in about $(L_y/2)^2/D_{\mathrm{PDE}} \sim 4$ min. The $x-t$ average of the diffusion equation describing the dynamics of the PDE concentration $\bar{C}_{\mathrm{PDE}}$ is

$$D_{\mathrm{PDE}} \frac{d^2}{dy^2} \bar{C}_{\mathrm{PDE}} + s_{\mathrm{PDE}} \bar{n}_{\mathrm{cell}} = 0\,. \tag{C.1}$$

The vertical thickness of the chamber is small, $l_z = 5$ μm. Therefore, within the chamber, the PDE concentration is considered uniform in this direction. As previously discussed, we assume the boundary conditions

$$\bar{C}_{\mathrm{PDE}}(0) \;=\; 0 \tag{C.2}$$

and

$$\bar{C}_{\mathrm{PDE}}(L_y) \;=\; 0\,. \tag{C.3}$$

The solution of Eq. (C.1) subject to the boundary conditions in Eqs. (C.2) and (C.3) is

$$\bar{C}_{\mathrm{PDE}}(y) \;=\; \frac{s_{\mathrm{PDE}} \bar{n}_{\mathrm{cell}}}{2 D_{\mathrm{PDE}}} L_y^2 \frac{y}{L_y} \left(1 - \frac{y}{L_y}\right). \tag{C.4}$$

Next, to justify (C.2) we argue that $\bar{C}_{\mathrm{PDE}}(L_y/2) \gg \bar{C}_{\mathrm{PDE}}(0)$ holds in our experimental setup. The PDE concentration at $y = 0$ is estimated by matching it to an estimate of the PDE concentration in the reservoir at $y < 0$, which is $n_{\mathrm{cell}} s_{\mathrm{PDE}} T$. Thus, Eq. (C.2) is valid if

$$(n_{\rm cell} s_{\rm PDE} T) l_z \ll \frac{s_{\rm PDE} \bar{n}_{\rm cell}}{8 D_{\rm PDE}} L_y^2 \,, \tag{C.5}$$

where the factor l_z on the left hand side of this inequality results from the fact that $\bar{C}_{\rm PDE}$ is a surface density rather than a volume density. With $\bar{n}_{\rm cell} = n_{\rm cell} L_z$, the cell density and the unknown PDE production rate $s_{\rm PDE}$ cancel, and the inequality becomes

$$T \ll \frac{L_z}{l_z} \frac{L_y^2}{8 D_{\rm PDE}} \,. \tag{C.6}$$

Using the dimensions of the experimental setup and an estimate of the diffusivity of the PDE in Eq. (C.6), we obtain

$$T = 5{\rm hours} \ll \frac{1{\rm mm}}{5\mu{\rm m}} \frac{9 \times 10^4 \mu{\rm m}^2}{8 \times 100 \mu{\rm m}^2/{\rm sec}} \approx 56{\rm hours} \,. \tag{C.7}$$

Therefore, the boundary condition assumed in Eq. (C.2) is reasonable. The other boundary condition, Eq. (C.3), is even better justified because: (i) the number of cells in the $y > L_y$ reservoir is much smaller than the number of cells in the $y < 0$ reservoir, and (ii) the experimental time (≈ 1 hour) is shorter than T.

C.2 Fokker-Planck equation for aca- mutant cells

In this section we describe the steady-state behavior of the model in the continuum approximation. For the non-interacting aca- cells, the cAMP density gradient always points toward the $y > L_y$ reservoir (i.e., $\nabla C / |\nabla C| = \hat{\mathbf{y}}$). Additionally, we set $\mathbf{f} \to 0$ for the continuum limit, and thus the attractor vector in Eq. (2) reduces

to $\mathbf{g} = \xi_x \hat{\mathbf{x}} + (1 + \xi_y)\hat{\mathbf{y}}$. Since $|\mathbf{n}| = 1$, Eq. (2) reduces to

$$\frac{d\theta}{dt} = -\omega\theta + \omega\xi_x \,, \tag{C.8}$$

where θ is the angle between $\mathbf{n}$ and the y axis. The steady-state, spatially uniform version of the Fokker-Planck equation corresponding to (1) and (C.8) is

$$\frac{\partial}{\partial\theta}\left(\omega\theta\rho + \frac{\eta\omega^2}{2}\frac{\partial\rho}{\partial\theta}\right) = 0 \,, \tag{C.9}$$

where $\rho = \rho(x, y, \theta; t)$ is the probability density of the cells in (x, y, θ) space. Multiplying Eq. (C.9) by θ^2 and integrating over θ from $\theta = -\pi$ to $\theta = \pi$ with ρ assumed small away from $\theta \approx 0$ we obtain

$$\frac{\langle\theta^2\rho\rangle}{\langle\rho\rangle} = \eta\omega/2 \,. \tag{C.10}$$

C.3 Results for uniform degradation scheme

In our model we considered a non-uniform cAMP degradation scheme, which is justified by the boundary conditions of the setup and the initial conditions determined by the cell preparation. In this section we show results for which we apply uniform cAMP degradation in the $0 < y' < 1$ region. The degradation for the external cAMP is treated as being spatially uniform in most of the other chemotaxis and collective cell migration models [19, 44, 47, 116]. We summarize our results for the constant degradation scheme in Fig. S1, where we show $\overline{M}(y')$ and $\overline{\rho}(y')$ for $\nu_0 = 3$. Compared to the results obtained using the non-uniform cAMP degradation scheme

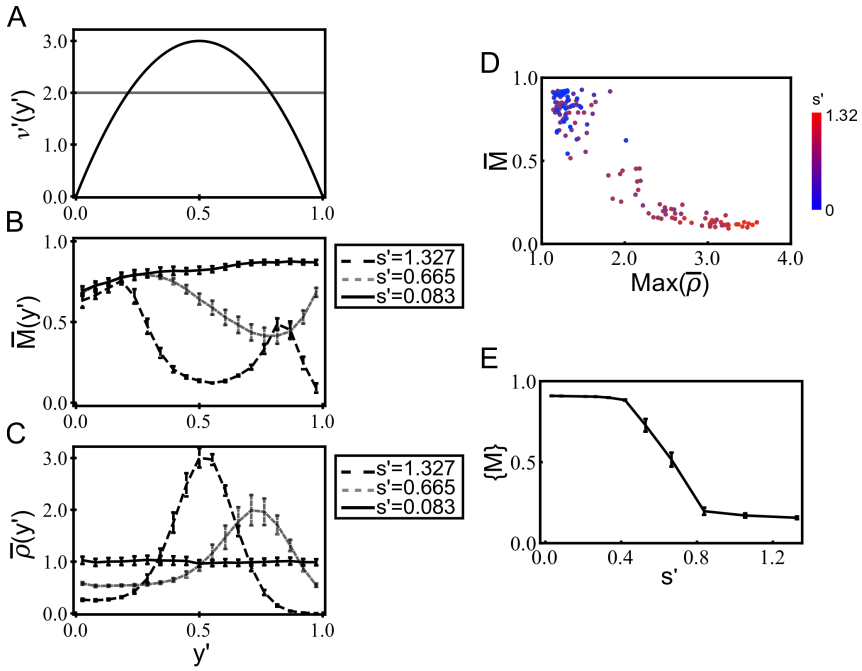

Figure C.1: (A) The degradation rate as a function of the distance from the cell reservoir, where $\nu_0 = 3$. (B) $\overline{M}(y')$ is shown for three representative relative cAMP secretion rates, whose dynamics is shown in Fig. 4.3. (C) $\overline{\rho}(y')$ for the same relative cAMP secretion rates used in the upper panel. (D) Maximum $\overline{\rho}(y')$ in the $0.5 \leq y' \leq 1$ region, is plotted against its corresponding M for all numerical simulations with constant degradation scheme. Each point represents a single numerical realization and is color coded with respect to s'. (E) $\{M\}$ is plotted against s', where the each data point is obtained from averaging many numerical realizations $(10-30)$. The vertical bars represent the error in the mean, which is calculated by the standard error from many realizations.

(Figs. 4.4B-D, and 4.5A), the results of the uniform cAMP degradation do not differ qualitatively.

C.4 Comparison of density profile measured from experiments

Tracking individual cells within a stream is technically difficult. However, because the depth of the experimental region is approximately the same as the thickness of the cell, we can infer the local cell number from the images. More precisely, we thresholded and binarized the time-lapsed images to determine the z-projected area of the stream. We estimate this area is proportional to the number of cells within the stream. Figure C.2 shows the local density obtained from experiments and simulations as a function of distance from the cell reservoir. Overall, both experiments with wild-type cells and simulations show an increase in density along the gradient direction and a peak density close to the high cAMP reservoir (Figs. C.2A and C.2B), with a stronger peak when the external cAMP concentration is low. The experiments and simulations disagree in the low external cAMP case near the cell reservoir. In the simulations, signal relay begins when the cells enter the thin gradient chamber. In the experiments, signal relay is not restricted, and in low cAMP regions such as the cell influx well, the cells may begin to form streams. Mutant cells that do not secrete cAMP have a uniform density in the gradient chamber (Fig. C.2C). To match the experimental density curve for the PDE1- cells, we lowered the cell secretion rate (Fig. C.2D). This result suggests a testable prediction from our studies.

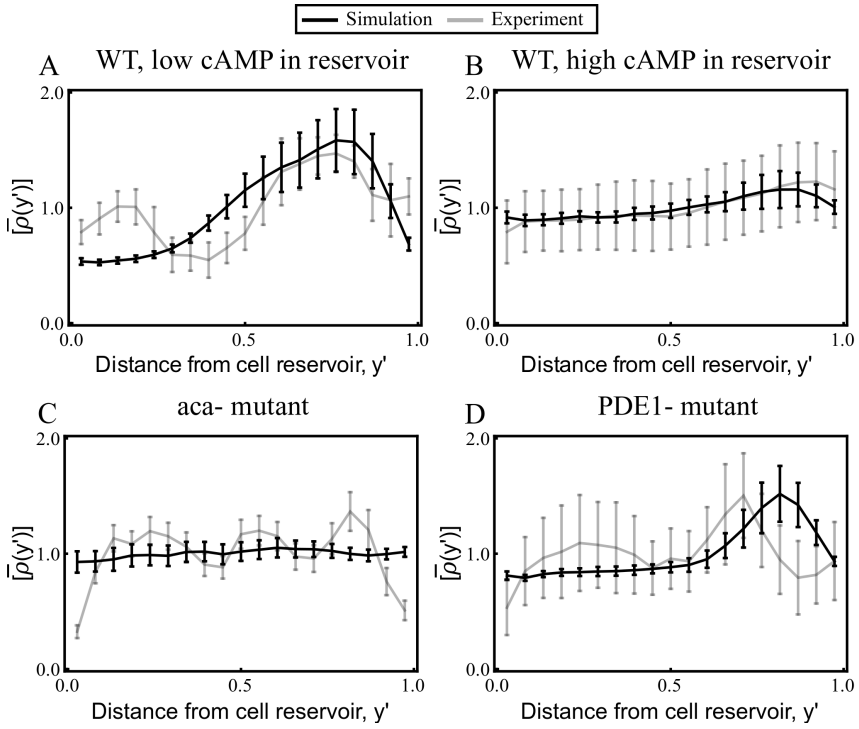

Figure C.2: The density, $\overline{\rho}(y')$, is plotted against the distance from the cell reservoir for wild-type cells moving in low cAMP concentration in the reservoir (left), wild-type cells moving in high cAMP concentration in the reservoir (center) and aca- mutant cells moving in high cAMP concentration in the reservoir (right). The density profile is obtained both from experiments and simulations of the model for (A) $\nu_0' = 3$, $s' = 0.665$, (B) $\nu_0' = 3$, $s' = 0.528$, (C) $\nu_0' = 3$, $s' = 0.033$, (D) $\nu_0' = 0.015$, $s' = 0.265$. Each simulation data point is obtained from averaging many numerical realizations. The vertical bars in both experimental and simulation data represent the standard error of the mean.

Bibliography

[1] Xuesong Yang, Dirk Dormann, Andrea E Münsterberg, and Cornelis J Weijer. Cell movement patterns during gastrulation in the chick are controlled by positive and negative chemotaxis mediated by FGF4 and FGF8. *Dev. Cell*, 3(3):425–37, September 2002.

[2] Lawrence F Brown, Naomi Lanir, Jan McDonagh, Kathy Tognazzi, Ann M Dvorak, and Harold F Dvorak. Fibroblast migration in fibrin gel matrices. *The American journal of pathology*, 142(1):273, 1993.

[3] Jareer Kassis, Douglas A Lauffenburger, Timothy Turner, and Alan Wells. Tumor invasion as dysregulated cell motility. *Seminars in Cancer Biology*, 11(2):105 – 119, 2001.

[4] Evanthia T Roussos, John S Condeelis, and Antonia Patsialou. Chemotaxis in cancer. *Nature Reviews Cancer*, 11(8):573–587, 2011.

[5] Cornelis J Weijer. Signalling during dictyostelium development. In Maria Romeralo, Sandra Baldauf, and Ricardo Escalante, editors, *Dictyostelids*, pages 49–70. Springer Berlin Heidelberg, 2013.

[6] Carole A Parent and Peter N Devreotes. A cell's sense of direction. *Science*, 284(5415):765–70, April 1999.

[7] Chris Janetopoulos, Lan Ma, Peter N. Devreotes, and Pablo A. Iglesias. Chemoattractant-induced phosphatidylinositol 3,4,5-trisphosphate accumulation is spatially amplified and adapts, independent of the actin cytoskeleton. *Proceedings of the National Academy of Sciences of the United States of America*, 101(24):8951–8956, 2004.

[8] Colin P McCann, Paul W Kriebel, Carole A Parent, and Wolfgang Losert. Cell speed, persistence and information transmission during signal relay and collective migration. *J Cell Sci*, 123(Pt 10):1724–31, May 2010.

[9] Liang Li, Simon F Norrelykke, and Edward C Cox. Persistent cell motion in the absence of external signals: a search strategy for eukaryotic cells. *PLoS One*, 3(5):e2093, 2008.

[10] Nicholas P Barry and Mark S Bretscher. Dictyostelium amoebae and neutrophils can swim. *Proc. Natl. Acad. Sci. U.S.A.*, 107(25):11376–80, June 2010.

[11] Meghan K Driscoll, Colin McCann, Rael Kopace, Tess Homan, John T Fourkas, Carole Parent, and Wolfgang Losert. Cell shape dynamics: from waves to migration. *PLoS Comput Biol*, 8(3):e1002392, March 2012.

[12] Morrel H Cohen and Anthony Robertson. Wave propagation in the early stages of aggregation of cellular slime molds. *Journal of theoretical biology*, 31(1):101–118, 1971.

[13] Michael J Potel and Steven A Mackay. Preaggregative cell motion in dictyostelium. *Journal of cell science*, 36(1):281–309, 1979.

[14] Stephanie Alexander, Gudrun E Koehl, Markus Hirschberg, Edward K Geissler, and Peter Friedl. Dynamic imaging of cancer growth and invasion: a modified skin-fold chamber model. *Histochem. Cell Biol.*, 130(6):1147–54, December 2008.

[15] Cornelis J Weijer. Collective cell migration in development. *J. Cell. Sci.*, 122(Pt 18):3215–23, September 2009.

[16] Can Guven, Erin Rericha, Edward Ott, and Wolfgang Losert. Modeling and measuring signal relay in noisy directed migration of cell groups. *PLoS Comput. Biol.*, 9(5):e1003041, May 2013.

[17] Arthur T Winfree. *The geometry of biological time*, volume 12. Springer, 2001.

[18] Thomas Gregor, Koichi Fujimoto, Noritaka Masaki, and Satoshi Sawai. The onset of collective behavior in social amoebae. *Science*, 328(5981):1021–5, May 2010.

[19] Herbert Levine, Igor Aranson, Lev Tsimring, and Thai Viet Truong. Positive genetic feedback governs camp spiral wave formation in dictyostelium. *Proceedings of the National Academy of Sciences*, 93(13):6382–6386, 1996.

[20] Satoshi Sawai, Peter A Thomason, and Edward C Cox. An autoregulatory circuit for long-range self-organization in Dictyostelium cell populations. *Nature*, 433(7023):323–6, January 2005.

[21] Ying-Ying Chang. Cyclic 3', 5'-adenosine monophosphate phosphodiesterase produced by the slime mold *Dictyostelium discoideum*. *Science*, 161(3836):57–59, 1968.

[22] Günther Gerisch, D Hulser, Dieter Malchow, and Ursula Wick. Cell communication by periodic cyclic-amp pulses. *Philosophical Transactions of the Royal Society of London. B, Biological Sciences*, 272(915):181–192, 1975.

[23] Peter N Devreotes, Pamela L Derstine, and Theodore L Steck. Cyclic 3', 5'amp relay in *Dictyostelium discoideum*. i. a technique to monitor responses to controlled stimuli. *The Journal of cell biology*, 80(2):291–299, 1979.

[24] Paul W Kriebel, Valerie A Barr, and Carole A Parent. Adenylyl cyclase localization regulates streaming during chemotaxis. *Cell*, 112(4):549–560, 2003.

[25] Gene L Garcia, Erin C Rericha, Christopher D Heger, Paul K Goldsmith, and Carole A Parent. The group migration of dictyostelium cells is regulated by extracellular chemoattractant degradation. *Molecular biology of the cell*, 20(14):3295–3304, 2009.

[26] Till Bretschneider, Kurt Anderson, Mary Ecke, Annette Müller-Taubenberger, Britta Schroth-Diez, Hellen C Ishikawa-Ankerhold, and Günther Gerisch. The three-dimensional dynamics of actin waves, a model of cytoskeletal self-organization. *Biophys. J.*, 96(7):2888–900, April 2009.

[27] Thomas D Pollard and John A Cooper. Actin, a central player in cell shape and movement. *Science*, 326(5957):1208–1212, 2009.

[28] Daniel A Fletcher and R Dyche Mullins. Cell mechanics and the cytoskeleton. *Nature*, 463(7280):485–492, 2010.

[29] King Lam Hui, Sae In Kwak, and Arpita Upadhyaya. Adhesion-dependent modulation of actin dynamics in jurkat t cells. *Cytoskeleton*, 71(2):119–135, 2014.

[30] Günther Gerisch, Till Bretschneider, Annette Müller-Taubenberger, Evelyn Simmeth, Mary Ecke, Stefan Diez, and Kurt Anderson. Mobile actin clusters and traveling waves in cells recovering from actin depolymerization. *Biophys. J.*, 87(5):3493–503, November 2004.

[31] Orion D Weiner, William A Marganski, Lani F Wu, Steven J Altschuler, and Marc W Kirschner. An actin-based wave generator organizes cell motility. *PLoS Biol.*, 5(9):e221, September 2007.

[32] Orion D Weiner, Maike C Rentel, Alex Ott, Glenn E Brown, Mark Jedrychowski, Michael B Yaffe, Steven P Gygi, Lewis C Cantley, Henry R Bourne, and Marc W Kirschner. Hem-1 complexes are essential for rac activation, actin polymerization, and myosin regulation during neutrophil chemotaxis. *PLoS biology*, 4(2):e38, 2006.

[33] Carole A Parent and Orion D Weiner. The symphony of cell movement: how cells orchestrate diverse signals and forces to control migration. *Current opinion in cell biology*, 25(5):523–525, 2013.

[34] Robert Insall. The interaction between pseudopods and extracellular signalling during chemotaxis and directed migration. *Current opinion in cell biology*, 25(5):526–531, 2013.

[35] Mitchell H Gail and Charles W Boone. The locomotion of mouse fibroblasts in tissue culture. *Biophysical journal*, 10(10):980–993, 1970.

[36] Kristen F Swaney, Chuan-Hsiang Huang, and Peter N Devreotes. Eukaryotic chemotaxis: a network of signaling pathways controls motility, directional sensing, and polarity. *Annu Rev Biophys*, 39:265–89, June 2010.

[37] Tian Jin. Gradient sensing during chemotaxis. *Current opinion in cell biology*, 25(5):532–537, 2013.

[38] Christopher J Bettinger, Robert Langer, and Jeffrey T Borenstein. Engineering substrate topography at the micro- and nanoscale to control cell function. *Angew. Chem. Int. Ed. Engl.*, 48(30):5406–15, 2009.

[39] Andre Levchenko and Pablo A Iglesias. Models of eukaryotic gradient sensing: application to chemotaxis of amoebae and neutrophils. *Biophys. J.*, 82(1 Pt 1):50–63, January 2002.

[40] Reinhold Fürth. Die Brownsche Bewegung bei Berücksichtigung einer Persistenz der Bewegungsrichtung. Mit Anwendungen auf die Bewegung lebender Infusorien. *Zeitschrift für Physik*, 2:244–256, 1920.

[41] Robert P Futrelle, J Traut, and W George McKee. Cell behavior in *Dictyostelium discoideum*: preaggregation response to localized cyclic AMP pulses. *J. Cell Biol.*, 92(3):807–21, March 1982.

[42] Alan R Gingle. Critical density for relaying in *Dictyostelium discoideum* and its relation to phosphodiesterase secretion into the extracellular medium. *Journal of cell science*, 20(1):1–20, 1976.

[43] Alan R Gingle and A Robertson. The development of the relaying competence in *Dictyostelium discoideum*. *Journal of cell science*, 20(1):21–27, 1976.

[44] Jean-Louis Martiel and Albert Goldbeter. A model based on receptor desensitization for cyclic amp signaling in dictyostelium cells. *Biophysical journal*, 52(5):807–828, 1987.

[45] Herbert Levine and William Reynolds. Streaming instability of aggregating slime mold amoebae. *Phys Rev Lett*, 66(18):2400–2403, May 1991.

[46] Oliver Steinbock, Florian Siegert, Stefan C Muller, and Cornelis J Weijer. Three-dimensional waves of excitation during Dictyostelium morphogenesis. *Proc Natl Acad Sci U S A*, 90(15):7332–5, August 1993.

[47] David A Kessler and Herbert Levine. Pattern formation in dictyostelium via the dynamics of cooperative biological entities. *Physical Review E*, 48(6):4801, 1993.

[48] Eirikur Palsson and Edward C Cox. Origin and evolution of circular waves and spirals in *Dictyostelium discoideum* territories. *Proceedings of the National Academy of Sciences*, 93(3):1151–1155, 1996.

[49] Marten Postma and Peter JM Van Haastert. A diffusion–translocation model for gradient sensing by chemotactic cells. *Biophysical Journal*, 81(3):1314–1323, 2001.

[50] Herbert Levine, David A Kessler, and Wouter-Jan Rappel. Directional sensing in eukaryotic chemotaxis: a balanced inactivation model. *Proc. Natl. Acad. Sci. U.S.A.*, 103(26):9761–6, June 2006.

[51] Eirikur Palsson and Hans G Othmer. A model for individual and collective cell movement in *Dictyostelium discoideum*. *Proceedings of the National Academy of Sciences*, 97(19):10448–10453, 2000.

[52] Nicola J Armstrong, Kevin J Painter, and Jonathan A Sherratt. A continuum approach to modelling cell-cell adhesion. *J. Theor. Biol.*, 243(1):98–113, November 2006.

[53] Javier Satulovsky, Roger Lui, and Yu-li Wang. Exploring the control circuit of cell migration by mathematical modeling. *Biophys J*, 94(9):3671–83, May 2008.

[54] Inbal Hecht, Monica L Skoge, Pascale G Charest, Eshel Ben-Jacob, Richard A Firtel, William F Loomis, Herbert Levine, and Wouter-Jan Rappel. Activated membrane patches guide chemotactic cell motility. *PLoS Comput Biol*, 7(6):e1002044, June 2011.

[55] Elizabeth D Hay. Extracellular matrix, cell skeletons, and embryonic development. *Am. J. Med. Genet.*, 34(1):14–29, September 1989.

[56] Katarina Wolf, Regina Müller, Stefan Borgmann, Eva-B Bröcker, and Peter Friedl. Amoeboid shape change and contact guidance: T-lymphocyte crawling through fibrillar collagen is independent of matrix remodeling by MMPs and other proteases. *Blood*, 102(9):3262–9, November 2003.

[57] Hisashi Haga, Chikako Irahara, Ryo Kobayashi, Toshiyuki Nakagaki, and Kazushige Kawabata. Collective movement of epithelial cells on a collagen gel substrate. *Biophys. J.*, 88(3):2250–6, March 2005.

[58] Elisabetta Ada Cavalcanti-Adam, Tova Volberg, Alexandre Micoulet, Horst Kessler, Benjamin Geiger, and Joachim Pius Spatz. Cell spreading and focal adhesion dynamics are regulated by spacing of integrin ligands. *Biophys. J.*, 92(8):2964–74, April 2007.

[59] Tobias P Kunzler, Christoph Huwiler, Tanja Drobek, Janos Vörös, and Nicholas D Spencer. Systematic study of osteoblast response to nanotopography by means of nanoparticle-density gradients. *Biomaterials*, 28(33):5000–6, November 2007.

[60] Laurent Bozec, Gert van der Heijden, and Michael Horton. Collagen fibrils: nanoscale ropes. *Biophys. J.*, 92(1):70–5, January 2007.

[61] Meghan K Driscoll, Xiaoyu Sun, Can Guven, John T Fourkas, and Wolfgang Losert. Cellular Contact Guidance through Dynamic Sensing of Nanotopography. *ACS Nano*, March 2014.

[62] Bijan Boldajipour, Harsha Mahabaleshwar, Elena Kardash, Michal Reichman-Fried, Heiko Blaser, Sofia Minina, Duncan Wilson, Qiling Xu, and Erez Raz. Control of chemokine-guided cell migration by ligand sequestration. *Cell*, 132(3):463–473, 2008.

[63] Chun-Min Lo, Hong-Bei Wang, Micah Dembo, and Yu-li Wang. Cell movement is guided by the rigidity of the substrate. *Biophysical journal*, 79(1):144–152, 2000.

[64] Michele Weber, Robert Hauschild, Jan Schwarz, Christine Moussion, Ingrid de Vries, Daniel F Legler, Sanjiv A Luther, Tobias Bollenbach, and Michael Sixt. Interstitial dendritic cell guidance by haptotactic chemokine gradients. *Science*, 339(6117):328–332, 2013.

[65] Pere Roca-Cusachs, Raimon Sunyer, and Xavier Trepat. Mechanical guidance of cell migration: lessons from chemotaxis. *Current opinion in cell biology*, 25(5):543–549, 2013.

[66] Anders E Carlsson. Dendritic actin filament nucleation causes traveling waves and patches. *Phys. Rev. Lett.*, 104(22):228102, June 2010.

[67] Christian Westendorf, Jose Negrete, Albert J Bae, Rabea Sandmann, Eberhard Bodenschatz, and Carsten Beta. Actin cytoskeleton of chemotactic amoebae operates close to the onset of oscillations. *Proc. Natl. Acad. Sci. U.S.A.*, 110(10):3853–8, March 2013.

[68] Nathan W Goehring and Stephan W Grill. Cell polarity: mechanochemical patterning. *Trends in cell biology*, 23(2):72–80, 2013.

[69] Atsuo T Sasaki, Chris Janetopoulos, Susan Lee, Pascale G Charest, Kosuke Takeda, Lauren W Sundheimer, Ruedi Meili, Peter N Devreotes, and Richard A Firtel. G protein-independent Ras/PI3K/F-actin circuit regulates basic cell motility. *J. Cell Biol.*, 178(2):185–91, July 2007.

[70] Chuan-Hsiang Huang, Ming Tang, Changji Shi, Pablo A Iglesias, and Peter N Devreotes. An excitable signal integrator couples to an idling cytoskeletal oscillator to drive cell migration. *Nature cell biology*, 2013.

[71] Günther Gerisch. Self-organizing actin waves that simulate phagocytic cup structures. *PMC Biophys*, 3(1):7, 2010.

[72] Till Bretschneider, Stefan Diez, Kurt Anderson, John Heuser, Margaret Clarke, Annette Müller-Taubenberger, Jana Köhler, and Günther Gerisch. Dynamic actin patterns and Arp2/3 assembly at the substrate-attached surface of motile cells. *Curr. Biol.*, 14(1):1–10, January 2004.

[73] F Hanakam, R Albrecht, C Eckerskorn, M Matzner, and G Gerisch. Myristoylated and non-myristoylated forms of the ph sensor protein hisactophilin ii: intracellular shuttling to plasma membrane and nucleus monitored in real time by a fusion with green fluorescent protein. *The EMBO journal*, 15(12):2935, 1996.

[74] Robert Tarjan. Depth-first search and linear graph algorithms. *SIAM journal on computing*, 1(2):146–160, 1972.

[75] Jun Allard and Alex Mogilner. Traveling waves in actin dynamics and cell motility. *Current opinion in cell biology*, 25(1):107–115, 2013.

[76] Gillian L Ryan, Naoki Watanabe, and Dimitrios Vavylonis. A review of models of fluctuating protrusion and retraction patterns at the leading edge of motile cells. *Cytoskeleton*, 69(4):195–206, 2012.

[77] Changji Shi, Chuan-Hsiang Huang, Peter N Devreotes, and Pablo A Iglesias. Interaction of motility, directional sensing, and polarity modules recreates the behaviors of chemotaxing cells. *PLoS computational biology*, 9(7):e1003122, 2013.

[78] Daisuke Taniguchi, Shuji Ishihara, Takehiko Oonuki, Mai Honda-Kitahara, Kunihiko Kaneko, and Satoshi Sawai. Phase geometries of two-dimensional excitable waves govern self-organized morphodynamics of amoeboid cells. *Proceedings of the National Academy of Sciences*, 110(13):5016–5021, 2013.

[79] Varunyu Khamviwath, Jifeng Hu, and Hans G Othmer. A continuum model of actin waves in *Dictyostelium discoideum*. *PloS one*, 8(5):e64272, 2013.

[80] William R Holmes, Anders E Carlsson, and Leah Edelstein-Keshet. Regimes of wave type patterning driven by refractory actin feedback: transition from static polarization to dynamic wave behaviour. *Physical biology*, 9(4):046005, 2012.

[81] Elena G Yarmola, Thayumanasamy Somasundaram, Todd A Boring, Ilan Spector, and Michael R Bubb. Actin-latrunculin a structure and function differential modulation of actin-binding protein function by latrunculin a. *Journal of Biological Chemistry*, 275(36):28120–28127, 2000.

[82] Tim Lämmermann, Bernhard L Bader, Susan J Monkley, Tim Worbs, Roland Wedlich-Söldner, Karin Hirsch, Markus Keller, Reinhold Förster, David R Critchley, Reinhard Fässler, and Michael Sixt. Rapid leukocyte migration by integrin-independent flowing and squeezing. *Nature*, 453(7191):51–5, May 2008.

[83] Tim Lämmermann, Philippe V Afonso, Bastian R Angermann, Ji Ming Wang, Wolfgang Kastenmüller, Carole A Parent, and Ronald N Germain. Neutrophil swarms require LTB4 and integrins at sites of cell death in vivo. *Nature*, 498(7454):371–5, June 2013.

[84] Jan Faix and Klemens Rottner. The making of filopodia. *Curr. Opin. Cell Biol.*, 18(1):18–25, February 2006.

[85] Viviana I Risca, Evan B Wang, Ovijit Chaudhuri, Jia Jun Chia, Phillip L Geissler, and Daniel A Fletcher. Actin filament curvature biases branching direction. *Proc. Natl. Acad. Sci. U.S.A.*, 109(8):2913–8, February 2012.

[86] Christopher N LaFratta, John T Fourkas, Tommaso Baldacchini, and Richard A Farrer. Multiphoton fabrication. *Angew. Chem. Int. Ed. Engl.*, 46(33):6238–58, 2007.

[87] Shoji Maruo and John T Fourkas. Recent progress in multiphoton microfabrication. *Laser & Photonics Reviews*, 2(1-2):100–111, 2008.

[88] George B Arfken, Hans J Weber, and Frank E Harris. *Mathematical Methods For Physicists International Student Edition*. Academic press, 2005.

[89] Jaume Masoliver and Josep M. Porrà. Harmonic oscillators driven by colored noise: Crossovers, resonances, and spectra. *Phys. Rev. E*, 48:4309–4319, Dec 1993.

[90] Natalie Andrew and Robert H Insall. Chemotaxis in shallow gradients is mediated independently of PtdIns 3-kinase by biased choices between random protrusions. *Nat Cell Biol*, 9(2):193–200, February 2007.

[91] Leonard Bosgraaf and Peter J M Van Haastert. Navigation of chemotactic cells by parallel signaling to pseudopod persistence and orientation. *PLoS One*, 4(8):e6842, 2009.

[92] Ralf Kemkemer, Simon Jungbauer, Dieter Kaufmann, and Hans Gruler. Cell orientation by a microgrooved substrate can be predicted by automatic control theory. *Biophysical journal*, 90(12):4701–4711, 2006.

[93] Nicolaas Godfried Van Kampen. *Stochastic processes in physics and chemistry*, volume 1. Elsevier, 1992.

[94] Shiro Kanegasaki, Yuka Nomura, Nao Nitta, Shuichi Akiyama, Takuya Tamatani, Yasuhiro Goshoh, Takashi Yoshida, Tsuyoshi Sato, and Yuji Kikuchi. A novel optical assay system for the quantitative measurement of chemotaxis. *J Immunol Methods*, 282(1-2):1–11, November 2003.

[95] Danny Fuller, Wen Chen, Micha Adler, Alex Groisman, Herbert Levine, Wouter-Jan Rappel, and William F Loomis. External and internal constraints on eukaryotic chemotaxis. *Proc Natl Acad Sci U S A*, 107(21):9656–9, May 2010.

[96] Gabriel Amselem, Matthias Theves, Albert Bae, Carsten Beta, and Eberhard Bodenschatz. Control parameter description of eukaryotic chemotaxis. *Phys. Rev. Lett.*, 109(10):108103, September 2012.

[97] Anna Bagorda, Satarupa Das, Erin C Rericha, David Chen, Jean Davidson, and Carole A Parent. Real-time measurements of cAMP production in live Dictyostelium cells. *J Cell Sci*, 122(Pt 21):3907–14, November 2009.

[98] Lunhua Liu, Satarupa Das, Wolfgang Losert, and Carole A. Parent. mTORC2 Regulates Neutrophil Chemotaxis in a cAMP- and RhoA-Dependent Fashion. *Dev Cell*, 19(6):845–857, 2010.

[99] Marco A R Vinolo, G John Ferguson, Suhasini Kulkarni, George Damoulakis, Karen Anderson, Mohammad Bohlooly-Y, Len Stephens, Phillip T Hawkins, and Rui Curi. SCFAs induce mouse neutrophil chemotaxis through the GPR43 receptor. *PLoS ONE*, 6(6):e21205, 2011.

[100] Nao Nitta, Tomoko Tsuchiya, Akira Yamauchi, Takuya Tamatani, and Shiro Kanegasaki. Quantitative analysis of eosinophil chemotaxis tracked using a novel optical device TAXIScan. *Journal of Immunological Methods*, 320(2):155–163, 2007.

[101] Masaru Ishii, Junichi Kikuta, Yutaka Shimazu, Martin Meier-Schellersheim, and Ronald N. Germain. Chemorepulsion by blood S1P regulates osteoclast precursor mobilization and bone remodeling in vivo. *The Journal of Experimental Medicine*, 207(13):2793–2798, 2010.

[102] Manfred Schienbein and Hans Gruler. Langevin equation, Fokker-Planck equation and cell migration. *B Math Biol*, 55(3):585–608, 1993.

[103] Catelijne Van Oss, Alexandre V Panfilov, Pauline Hogeweg, Florian Siegert, and Cornelis J Weijer. Spatial pattern formation during aggregation of the slime mould *Dictyostelium discoideum*. *Journal of theoretical biology*, 181(3):203–213, 1996.

[104] Bo Hu, Danny Fuller, William F Loomis, Herbert Levine, and Wouter-Jan Rappel. Phenomenological approach to eukaryotic chemotactic efficiency. *Phys Rev E Stat Nonlin Soft Matter Phys*, 81(3 Pt 1):031906, March 2010.

[105] M Schienbein, K Franke, and H Gruler. Random walk and directed movement: comparison between inert particles and self-organized molecular machines. *Physical Review E*, 49(6):5462, 1994.

[106] Alexander D Shenderov and Michael P Sheetz. Inversely correlated cycles in speed and turning in an ameba: an oscillatory model of cell locomotion. *Biophysical journal*, 72(5):2382–2389, 1997.

[107] Gabriel Amselem, Theves Matthias, Bae Albert, Bodenschatz Eberhard, and Beta Carsten. A Stochastic Description of Dictyostelium Chemotaxis. *PLoS ONE*, 7(5):e37213, 05 2012.

[108] David Selmeczi, Stephan Mosler, Peter H. Hagedorn, Niels B. Larsen, and Henrik Flyvbjerg. Cell Motility as Persistent Random Motion: Theories from Experiments. *Biophysical Journal*, 89(2):912–931, 2005.

[109] Hiroaki Takagi, Masayuki J Sato, Toshio Yanagida, and Masahiro Ueda. Functional analysis of spontaneous cell movement under different physiological conditions. *PLoS ONE*, 3(7):e2648, 2008.

[110] Daniel Campos, Vicenç Méndez, and Isaac Llopis. Persistent random motion: uncovering cell migration dynamics. *J. Theor. Biol.*, 267(4):526–34, December 2010.

[111] Leonard Bosgraaf and Peter J M Van Haastert. The ordered extension of pseudopodia by amoeboid cells in the absence of external cues. *PLoS One*, 4(4):e5253, 2009.

[112] Burton W Andrews and Pablo A Iglesias. An information-theoretic characterization of the optimal gradient sensing response of cells. *PLoS Comput. Biol.*, 3(8):e153, August 2007.

[113] Peter J M van Haastert and Marten Postma. Biased random walk by stochastic fluctuations of chemoattractant-receptor interactions at the lower limit of detection. *Biophys. J.*, 93(5):1787–96, September 2007.

[114] Masahiro Ueda and Tatsuo Shibata. Stochastic signal processing and transduction in chemotactic response of eukaryotic cells. *Biophys. J.*, 93(1):11–20, July 2007.

[115] Azadeh Samadani, Jerome Mettetal, and Alexander van Oudenaarden. Cellular asymmetry and individuality in directional sensing. *Proc Natl Acad Sci U S A*, 103(31):11549–54, August 2006.

[116] Yuanhua Tang and Hans G Othmer. A g protein-based model of adaptation in *Dictyostelium discoideum*. *Mathematical biosciences*, 120(1):25–76, 1994.

[117] John C Dallon and Hans G Othmer. A discrete cell model with adaptive signalling for aggregation of *Dictyostelium discoideum*. *Philosophical Transactions of the Royal Society of London. Series B: Biological Sciences*, 352(1351):391–417, 1997.

[118] Balint Szabo, GJ Szöllösi, B Gönci, Zs Jurányi, David Selmeczi, and Tamás Vicsek. Phase transition in the collective migration of tissue cells: experiment and model. *Physical Review E*, 74(6):061908, 2006.

[119] H. Chate, F Ginelli, G Gregoire, F Peruani, and F Raynaud. Modeling collective motion: variations on the Vicsek model. *Eur Phys J B*, 64(3):451–456, 2008.

[120] Martin Dworkin and Kenneth H. Keller. Solubility and diffusion coefficient of adenosine 3': 5'-monophosphate. *Journal of Biological Chemistry*, 252(3):864, 1977.

[121] Jikui Song, Lian-Wang Guo, Hakim Muradov, Nikolai O Artemyev, Arnold E Ruoho, and John L Markley. Intrinsically disordered gamma-subunit of cGMP phosphodiesterase encodes functionally relevant transient secondary and tertiary structure. *Proc Natl Acad Sci U S A*, 105(5):1505–10, February 2008.

[122] Tamás Vicsek, András Czirók, Eshel Ben-Jacob, Inon Cohen, and Ofer Shochet. Novel Type of Phase Transition in a System of Self-Driven Particles. *Phys. Rev. Lett.*, 75:1226–1229, Aug 1995.

[123] Andras Czirok, H Eugene Stanley, and Tamas Vicsek. Spontaneously ordered motion of self-propelled particles. *J Phys A-Math Gen*, 30:1375, 1997.

[124] Satarupa Das, Erin C Rericha, Anna Bagorda, and Carole A Parent. Direct biochemical measurements of signal relay during Dictyostelium development. *J Biol Chem*, 286(44):38649–58, November 2011.

[125] Wouter-Jan Rappel, Alastair Nicol, Armand Sarkissian, Herbert Levine, and William F. Loomis. Self-organized Vortex State in Two-Dimensional *Dictyostelium* Dynamics. *Phys. Rev. Lett.*, 83:1247–1250, Aug 1999.

[126] Xiaowen Liu, Bo Ma, Asrar B Malik, Haiyang Tang, Tao Yang, Bo Sun, Gang Wang, Richard D Minshall, Yan Li, Yong Zhao, Richard D Ye, and Jingsong Xu. Bidirectional regulation of neutrophil migration by mitogen-activated protein kinases. *Nat Immunol*, 13(5):457–64, May 2012.

[127] Laurent Golé, Charlotte Rivière, Yoshinori Hayakawa, and Jean-Paul Rieu. A quorum-sensing factor in vegetative *Dictyostelium discoideum* cells revealed by quantitative migration analysis. *PLoS ONE*, 6(11):e26901, 2011.

[128] Rebecca McLennan, Louise Dyson, Katherine W Prather, Jason A Morrison, Ruth E Baker, Philip K Maini, and Paul M Kulesa. Multiscale mechanisms

of cell migration during development: theory and experiment. *Development*, 139(16):2935–44, August 2012.

[129] Colin P McCann, Erin C Rericha, Chenlu Wang, Wolfgang Losert, and Carole Parent. Dictyostelium Cells Migrate Similarly on Surfaces of Varying Chemical Composition. *PLoS ONE*, 9(2):e87981, 2014.

[130] Morton McCutcheon. Vol. 26 july, 1946 no. 3 chemotaxis in leukocytes. *Physiological reviews*, 26(3), 1946.

[131] Barbara Varnum and David R Soll. Effects of camp on single cell motility in dictyostelium. *The Journal of cell biology*, 99(3):1151–1155, 1984.

[132] Yuan Xiong, Chuan-Hsiang Huang, Pablo A Iglesias, and Peter N Devreotes. Cells navigate with a local-excitation, global-inhibition-biased excitable network. *Proc. Natl. Acad. Sci. U.S.A.*, 107(40):17079–86, October 2010.

[133] Joshua Parker, Eilon Sherman, Matthias van de Raa, Devaraj van der Meer, Lawrence E. Samelson, and Wolfgang Losert. Automatic sorting of point pattern sets using Minkowski functionals. *Phys. Rev. E*, 88:022720, Aug 2013.

[134] Duncan S Callaway, Mark EJ Newman, Steven H Strogatz, and Duncan J Watts. Network robustness and fragility: Percolation on random graphs. *Physical review letters*, 85(25):5468, 2000.

[135] Mark Herrera, Shane McCarthy, Steven Slotterback, Emmanuel Cephas, Wolfgang Losert, and Michelle Girvan. Path to fracture in granular flows: Dynamics of contact networks. *Physical Review E*, 83(6):061303, 2011.

[136] Keith Burridge and Laurie Connell. A new protein of adhesion plaques and ruffling membranes. *J. Cell Biol.*, 97(2):359–67, August 1983.

[137] Philippe V Afonso, Mirkka Janka-Junttila, Young Jong Lee, Colin P McCann, Charlotte M Oliver, Khaled A Aamer, Wolfgang Losert, Marcus T Cicerone, and Carole A Parent. LTB_4 is a signal-relay molecule during neutrophil chemotaxis. *Developmental cell*, 22(5):1079–1091, 2012.

[138] Matthew B Byrne, Yuki Kimura, Ashish Kapoor, Yuan He, Kewin S Mattam, Katherine M Hasan, Luke N Olson, Fei Wang, Paul JA Kenis, and Christopher V Rao. Oscillatory behavior of neutrophils under opposing chemoattractant gradients supports a winner-take-all mechanism. *PloS one*, 9(1):e85726, 2014.

[139] Peter JM van Haastert, Ineke Keizer-Gunnink, and Arjan Kortholt. Essential role of pi3-kinase and phospholipase a2 in *Dictyostelium discoideum* chemotaxis. *The Journal of cell biology*, 177(5):809–816, 2007.

[140] Gunther Gerisch. Extracellular cyclic-amp phosphodiesterase regulation in agar plate cultures of *Dictyostelium discoideum*. *Cell Differ*, 5(1):21–5, April 1976.

[141] R P Yeh, F K Chan, and M B Coukell. Independent regulation of the extracellular cyclic AMP phosphodiesterase-inhibitor system and membrane differentiation by exogenous cyclic AMP in *Dictyostelium discoideum*. *Dev Biol*, 66(2):361–74, October 1978.